

NASA TECHNICAL NOTE



NASA TN D-4211

2.1

NASA TN D-4211

LOAN COPY
APR 21 1968
KIRTLAND AFB, TEXAS



AERODYNAMIC CHARACTERISTICS OF SEVERAL CRANKED LEADING-EDGE WING-BODY COMBINATIONS AT MACH NUMBERS FROM 0.4 TO 2.94

*by Edward J. Hopkins, Raymond M. Hicks,
and Ralph L. Carmichael*

*Ames Research Center
Moffett Field, Calif.*



0130881

NASA TN D-4211

AERODYNAMIC CHARACTERISTICS OF SEVERAL CRANKED
LEADING-EDGE WING-BODY COMBINATIONS AT
MACH NUMBERS FROM 0.4 TO 2.94

By Edward J. Hopkins, Raymond M. Hicks,
and Ralph L. Carmichael

Ames Research Center
Moffett Field, Calif.

NATIONAL AERONAUTICS AND SPACE ADMINISTRATION

For sale by the Clearinghouse for Federal Scientific and Technical Information
Springfield, Virginia 22151 - CFSTI price \$3.00

AERODYNAMIC CHARACTERISTICS OF SEVERAL CRANKED

LEADING-EDGE WING-BODY COMBINATIONS AT

MACH NUMBERS FROM 0.4 TO 2.94

By Edward J. Hopkins, Raymond M. Hicks,
and Ralph L. Carmichael

Ames Research Center

SUMMARY

Experimental lift, drag, and pitching-moment characteristics are presented for several wing-body combinations. The leading edges of the wings are two straight-line segments of different sweep angles (referred to as "cranked" planforms). As a basis for comparison, one combination had a wing of triangular planform. Each wing was planar and was mounted separately on a cylindrical body of revolution which had a Sears-Haack nose.

Experimental results are presented for a Mach number range from 0.4 to 2.94 at a constant Reynolds number of 0.89 million. Results predicted by methods involving linear wing theories and slender-body interference effects are compared with the results measured at small angles of attack throughout the Mach number range.

Large leading-edge extensions over the inboard portion of the wing span produced nonlinear pitching-moment curves. There were no other large effects of leading-edge extensions; however, a theoretical analysis indicated that warping should improve the lift-drag ratio of one cranked planform about 10 percent whereas the triangular planform should derive practically no benefit from warping.

At low subsonic Mach numbers, practically no Reynolds number effect was indicated for the pitching-moment results obtained for two of the models at Reynolds numbers of 0.89 and 13.7 million.

INTRODUCTION

The effects of curved and cranked leading edges on the aerodynamic characteristics of low-aspect-ratio wings mounted on bodies have been investigated at Mach numbers from about 0.4 to 3.0. The initial part of this investigation (ref. 1) shows that some gains in aerodynamic efficiency over that of a triangular planform are attainable (an increment in maximum (L/D) of 0.2 to 0.5) throughout a Mach number range from 0.7 to 2.94 by use of spanwise variation of leading-edge sweep, that is, an "ogee" planform. The

planforms discussed herein have leading edges consisting of two straight lines which should have practical manufacturing advantages over the "ogee" planforms they approximate.

Part of the present investigation was devoted to the study of the effects of leading-edge geometry and planform variation on the linearity of the pitching-moment curve, particularly at high angles of attack and low Mach numbers. Low-aspect-ratio cranked wings are characterized by a strong vortex flow at high angles of attack which generally emanates and is discharged from the leading edge from which the flow ultimately rolls up into several discrete vortices. This separated vortex flow, the governing geometrical factors that produce it, and its relation to the surface pressures that cause static longitudinal instability on these wings are not clearly understood or predictable at this time. Most of the wings in the present investigation were designed to have a maximum thickness of 3-percent chord, constant along the span. The effect of variable thickness distribution along the span was investigated with two wings. All the cranked wings were designed to have subsonic leading edges over the inboard portions of their spans throughout the test Mach number range; consequently, these wings had rounded leading edges and subsonic-type profiles over this part of their spans. However, one cranked wing was tested with a sharp leading edge along its entire span to determine if the subsonic profile provided any benefits in aerodynamic efficiency.

Since the Reynolds number of the tests, based on the average wing chord, was less than 1 million, there was some concern regarding the application of the results to a full-sized airplane, especially at high angles of attack where some flow separation occurs. Consequently, data for two models have been correlated with data obtained on large-scale, geometrically similar models at a Reynolds number of about 13.7 million.

Experimental results at small angles of attack, where the flow is essentially attached and the curves are linear, are compared with results predicted by composite linear theories described in the appendixes. These theories include mutual interference effects between wing and body.

NOTATION

b	wing span
C_D'	uncorrected drag coefficient, $\frac{\text{drag (measured)}}{qS}$
C_D	drag coefficient corrected to zero leading-edge thickness and to an all-turbulent boundary layer, $\frac{\text{drag (corrected)}}{qS}$
C_{D_0}	minimum drag coefficient, corrected for zero leading-edge thickness and an all-turbulent boundary layer, obtained from an extrapolation of the drag-due-to-lift curve to zero lift coefficient

$\Delta C_{D_{SF}}$	estimated increment of skin-friction drag coefficient for completely turbulent flow on the model
ΔC_{D_B}	estimated increment of drag coefficient associated with the slightly blunted leading edges
C_L	lift coefficient, $\frac{\text{lift}}{qS}$
C_{L_0}	lift coefficient for minimum drag computed from best fitting parabola to experimental drag polar for data taken above $\alpha \cong 3^\circ$
C_m	pitching-moment coefficient, $\frac{\text{pitching moment about moment centers shown in figure 1}^1}{qS\bar{c}}$
$\frac{\partial C_L}{\partial \alpha}$	lift-curve slope measured at $C_L = 0$
$\frac{\partial C_D}{\partial (C_L - C_{L_0})^2}$	drag-due-to-lift factor
$\left(\frac{L}{D}\right)_{\text{max}}$	maximum ratio of lift to corrected drag, $\frac{C_L}{C_D}$
$\frac{\partial C_m}{\partial C_L}$	pitching-moment curve slope measured at $C_L = 0$
c	local wing chord
\bar{c}	mean aerodynamic chord of triangular wing (4.218 in.)
M	Mach number
q	free-stream dynamic pressure
R	Reynolds number based on the average chord of triangular wing
r	body radius

¹The moment center for each model, except model 10, was 4.288 inches ahead of the body trailing edge and corresponded to the 0.25 \bar{c} position for model 1. For model 10, the wing and moment center were shifted forward on the body the same amount, 2.064 inches.

- S wing area of triangular wing including area blanketed by body (21.75 in.² for models, 9970 ft² for flight example)
- α angle of attack

MODEL DESCRIPTION

Complete dimensional data and sketches of each model are given in figure 1. Model 1, considered the base model with a triangular planform, had the same geometry as the triangular-winged model of reference 1, but the profile was a circular arc (0.03 c thick) instead of a hexagonal profile (0.02 c thick). The thicker profile was selected since it was believed to be more representative of current structural design practice. To facilitate a comparison of the experimental results of several models, models 1 through 7 were designed with the same exposed span and exposed area, and hence the same exposed aspect ratio of 2.2. Models 2 through 7 had the same leading-edge sweep of 78° on the inboard part of each wing, but the sweep over outboard regions of each wing varied to maintain the same exposed area, trailing-edge geometry, and tip chord. Models 8 and 9 were designed with identical spans and exposed areas; hence, they had the same exposed aspect ratio of 1.5. On these models the leading-edge sweep of the inboard part of the wing was 82° and the outboard portion was 60°; the trailing edges were unswept. As shown in figure 1, models 8 and 9 differed from each other in the distance from the body to the notch point on the leading edge and in the taper ratio.

Most of the inboard portion of the wing leading edge of model 10 had a sweep of 82°; however, an arbitrary fairing for the wing leading edge was used at the body nose. The equation for this fairing is given in figure 1(g). The leading- and trailing-edge sweep angles on the outer portions of the wings of this model and model 11 were the same as for model 1, 59° and -10°, respectively.

Model 11 was geometrically similar to an existing large-scale model previously tested in the Ames 40- by 80-Foot Wind Tunnel. This model was formed by adding a sharp-edged, flat-sided extension to the wing leading edge of model 1 (see figs. 1(a) and 1(h)). The sweepback angle of this extension was 77.4°. The exposed aspect ratio changed from 2.2 to 1.9 as a result of this leading-edge extension.

Each wing was mounted in the horizontal plane of symmetry on a body of revolution with a Sears-Haack nose (defined in fig. 1(a)) and a cylindrical afterbody. The intersection of the wing trailing edge and the body was 1 inch from the body base for all models except model 10 for which this distance was 3.064 inches.

The models were mounted on a six-component electrical strain-gage balance which was sting supported through the base of the body.

All models except 1 and 11 were centrifugally cast in one piece from a beryllium-copper alloy with an ultimate strength of 70,000 psi and a yield

strength of 40,000 psi. The alloy was 2 to 2.25 percent beryllium, 0.35 to 0.65 percent cobalt, and the rest copper. Models 1 and 11 were of solid steel.

To preserve smooth leading and trailing edges, all models had slightly blunt edges. Experience has shown that if the leading edge is too sharp, imperfections produced in fabrication or during wind-tunnel operation will cause premature transition. The following average thicknesses were measured from cross-sectional slices made through wax impressions of each edge.

Model	Leading-edge thickness, in.	Trailing-edge thickness, in.
1	0.006	0.011
2	.007	.010
3	.003	.003
4	.007	.012
5	.007	.007
6	.011	.015
7	.008	.011
8	.006	.011
9	.005	.006
10	.012	.011
11	.006	.011

TEST PROCEDURE

The tests were conducted at Mach numbers of 0.4, 0.7, 0.9, 1.0, 1.1, and 1.4 in the Ames 2- by 2-Foot Wind Tunnel and at Mach numbers of 1.98 and 2.94 in the Ames 1- by 3-Foot Supersonic Wind Tunnel. The unit Reynolds number was held constant throughout the test at 2.5 million per foot; therefore, the Reynolds number, based on the mean aerodynamic chord of model 1, with the triangular wing, was 0.89 million.

At Mach numbers from 0.7 to 2.94, each model was pitched through an angle-of-attack range from -4° to $+12^{\circ}$ in 1° increments. At a Mach number of 0.4 the sting was offset at two different angles to cover a wider angle-of-attack range. For this Mach number each model was first pitched through an angle-of-attack range from -2° to $+14^{\circ}$ and then through an angle-of-attack range of 5° to 21° in 1° increments.

As in reference 1, all data were obtained with natural transition. The drag presented in the summary figures, however, was corrected to conditions corresponding to an all-turbulent boundary layer by the method of reference 1. The location of boundary-layer transition, which is required to correct the drag data, was determined from sublimation photographs taken at an angle of attack of 4° , which corresponded approximately to that for maximum lift-to-drag ratio for all models at all Mach numbers.

REDUCTION OF DATA

Corrections

The measured axial force was adjusted to the condition of free-stream static pressure acting on the model base. The angle of attack was corrected for sting and balance deflections due to pitching moment and normal force. The normal forces, pitching moments, and axial forces were corrected for first-order interactions between the various components of the balance. No temperature correction was applied as this correction was found to be negligible experimentally (the balance used was temperature compensated).

Although all models were designed to be symmetrical about a horizontal plane, the experimental data were slightly asymmetric. This asymmetry in the data may be due to wind-tunnel flow angularity and curvature, model manufacturing errors, and misalignment of the balance axis with the model axis. To correct for these effects, duplicate runs were made with the model upright and inverted. These data were used for correcting the basic lift and pitching-moment data (figs. 2-12, 18, and 19) to insure that C_L and C_m were zero when the angle of attack was zero. After the lift data were corrected a slight asymmetry remained in the drag polar. This condition, therefore, accounts for an apparent C_{L_0} measured for the models. A correction for the apparent C_{L_0} was applied to the drag-due-to-lift factors and the factors derived therefrom - the minimum drag coefficient, the drag due to lift, and maximum lift-drag ratio.

The drag data presented in the summary figures were corrected to conditions corresponding to an all-turbulent boundary layer by the method presented in appendix A of reference 1; the effects of the slightly blunted leading edges were taken into account by the method presented in appendix B of reference 1. (The leading-edge thicknesses used in the calculations are given under Model Description.) No corrections were applied for the finite thickness of the trailing edges. The skin friction and bluntness drag corrections which were applied are listed in table I.² Only the drag data presented in figures 14 through 16 were adjusted for all these drag corrections.

Maximum Lift-Drag Ratio

The maximum lift-drag ratios presented in figure 16 were computed from the faired curves of $[\partial C_D / \partial (C_L - C_{L_0})^2]_{\alpha > 3^\circ}$ and C_{D_0} as a function of Mach number (figs. 14 and 15). This procedure was used because the drag polars are parabolic for angles of attack above about 3° as indicated by the linearity of the drag-due-to-lift curves shown in part (c) of figures 2 through 11. Below an angle of attack of about 3° , the nonparabolic drag polar indicated there was more laminar flow on the model than at the higher angles of attack

²Corrections for model 11, which was tested over only a limited supersonic Mach number range, are not included in table I since this model was tested primarily to indicate if Reynolds number effects exist at low Mach numbers.

(cf. the experimental points in fig. 9(b) with the dashed part of the curve for a parabolic drag polar). The equation used for computing the maximum lift-drag ratios presented in figure 16 is:

$$\left(\frac{L}{D}\right)_{\max} = \frac{1}{2} \sqrt{\frac{1}{(C_{D_0}) \partial C_D / \partial (C_L - C_{L_0})^2}}$$

The data accuracy based on repeatability and known precision of the measuring equipment is listed below.

C_L	± 0.002	α	$\pm 0.05^\circ$
C_m	± 0.004	M	± 0.01
C_D	± 0.0002	R	$\pm 0.01 \times 10^6$

In addition, other inaccuracies are caused by shrinkage and warpage of cast models and flow nonuniformities in the wind tunnel. Such effects will be reflected primarily as small increments in angle of attack or pitching moment at zero lift.

The coordinates of each model were carefully measured with a dial gage and compared with the specified coordinates. Wave drag at several supersonic Mach numbers was computed for models whose coordinates showed the greatest deviation from the specified coordinates. It was found that these deviations caused increments in the drag coefficient of less than 0.0001.

THEORETICAL METHODS OF ANALYSIS

Details of the methods used in estimating the subsonic and the supersonic aerodynamic characteristics are summarized in appendixes A and B, respectively. For subsonic Mach numbers, two different methods were used to obtain the lift and center of pressure on the primary wing panels (outboard of the leading-edge notch point). In method 1, the DeYoung "rule of thumb" equation (ref. 2) is used and in method 2 the Lomax-Sluder theory (ref. 3) is used to estimate the lift and center of pressure on the primary wing panels. Since the Lomax-Sluder theory is given in reference 3 only for rectangular and triangular wings, this theory was applied only to wings 1, 8, and 10.

In method 3 for supersonic Mach numbers, the lift and center of pressure for the wing were estimated from the influence coefficients of reference 4. For all three methods the mutual interference effects between the wing panels and the body were estimated by the method of reference 5. Also, throughout the Mach number range, because the wing panels were thin and of low aspect ratio, the resultant force was assumed to be normal to the wing plane of symmetry; therefore, no leading-edge thrust was assumed and the drag-due-to-lift factor was the reciprocal of the lift-curve slope. The turbulent

skin-friction drag coefficients³ were computed from Schlichting's incompressible equation (ref. 6) with the compressibility accounted for by the method of Sommer and Short (ref. 7). At supersonic Mach numbers, wave drag was calculated by application of the supersonic area rule to an "equivalent" body of revolution for each wing-body combination.

RESULTS AND DISCUSSION

The lift, drag, pitching moment, and drag due to lift are presented in figures 2 through 12. The maximum lift-drag ratios, minimum drag coefficients, lift-curve slopes, drag-due-to-lift factors, and pitching-moment curve slopes obtained from the data of figures 2 through 11 are summarized in figures 13 through 17. Summary plots of minimum drag coefficient and maximum lift-drag ratio are presented for an all-turbulent boundary layer and zero leading-edge bluntness. Estimated values of the above aerodynamic parameters also are shown on the summary plots. Results obtained at Reynolds numbers of 0.89 and 13.7 million for two of the models, 1 and 11, are presented in figures 18 and 19, respectively.⁴

At $M = 0.4$, the pitching-moment results for the triangular wing (fig. 2(a)) show a reduced longitudinal stability at lift coefficients between about 0.5 and 0.7. The cranked planform with the smallest leading-edge extension, model 2 (fig. 3), appears to lose longitudinal stability more gradually over a wider lift-coefficient range than did model 1. The cranked planforms with larger forward extensions of the wing leading edge, however, have a much greater tendency toward longitudinal instability. (Compare fig. 3(a) with fig. 8(a), and fig. 9(a) with fig. 10(a).) There is also evidence that those models which exhibited instability tendencies at $M = 0.4$ also would have similar tendencies at $M = 2.94$ at the higher angles of attack (see part (a) of figs. 8-11).

Lift

Experimental ($M = 0.4$).- A small leading-edge extension increased the lift-curve slope with increasing angle of attack, the larger leading-edge extensions did not. (Compare results for model 1 with those for models 2 and 7.) Although the leading-edge extensions for both models 2 and 7 produce considerable nonlinearity in the lift curves, model 7 is effectively a lower aspect-ratio wing with greater leading-edge sweep than model 2; therefore, the associated lower lift-curve slope near $C_L = 0$ for model 7 overrides the beneficial effect of nonlinearity at the higher lift coefficients. The approximate angles of attack required to attain a lift coefficient of 0.8 are summarized in the following table.

³All data presented in figures 14 through 16 were corrected to conditions corresponding to an all-turbulent boundary layer as indicated under Reduction of Data.

⁴These results are not modified to the conditions of zero bluntness and an all-turbulent boundary layer.

Model	Figure	$\alpha_{C_L=0.8}$, deg	Exposed wing aspect ratio
1	2(a)	17	2.2
2	3(a)	15	↓
3	4(a)	17	
7	8(a)	18	
8	9(a)	20	1.5
9	10(a)	17	↓
10	11(a)	18	
11	12(a)	15	

Some of the differences in the angles shown in the table are related to the fact that models with lower aspect ratios have lower lift-curve slopes.

Theoretical.- At subsonic Mach numbers, for wings with triangular panels (see fig. 13; models 1, 8, and 10), method 2 (ref. 3) gives better agreement with experiment than method 1 (ref. 2) for the lift-curve slope. For the other models (2-7, 9) on which the outer main wing panels are trapezoidal, method 1 does not predict the large increase in lift-curve slope at transonic Mach numbers. At supersonic Mach numbers up to about 2.0, the predicted $C_{L\alpha}$ generally agrees well with the measured $C_{L\alpha}$ except for models 8 and 10 (the only models with the leading-edge extension originating at the body nose); at higher Mach numbers the experimental $C_{L\alpha}$ were generally larger than predicted.

Drag Due to Lift

Experimental.- The drag-due-to-lift factor $\partial C_D / \partial (C_L - C_{L_0})^2$ is important because of its contribution to the maximum lift-drag ratio. The efficiency of thin low-aspect-ratio wings can be evaluated by comparing the measured $\partial C_D / \partial (C_L - C_{L_0})^2$ to the reciprocal of the measured lift-curve slope representing no leading-edge thrust. Drag efficiency factors⁵ representing this comparison were computed from the results in figures 13 and 14 and are summarized in the following table for four Mach numbers.

⁵A positive number for this factor means that the resultant-force vector is tilted forward of an axis perpendicular to the wing-chord plane so that some leading-edge thrust is realized.

$\left[\left(\frac{1}{C_{L\alpha}} \right) - \frac{\partial C_D}{\partial (C_L - C_{L_0})^2} \right]_{\text{exp}} / \left[\frac{\partial C_D}{\partial (C_L - C_{L_0})^2} \right]_{\text{exp}}$				
Model	M = 0.4	M = 0.8	M = 1.2	M = 2.8
1	0.16	0.17	0.12	-0.01
2	.24	.11	.10	0
3	.18	.11	.12	.02
4	.11	.09	.09	.01
5	.17	.22	.08	.01
6	.23	.13	.14	.01
7	.19	.07	.02	0
8	.28	.20	.08	.02
9	.38	.227	.11	0
10	.29	.17	.03	0

It can be seen that some of the cranked planforms had considerably more leading-edge thrust than the triangular planform (model 1) at $M = 0.4$. Also, at $M = 0.4$ and 0.8 using a round-nosed profile on the leading-edge extension instead of a sharp-nosed profile was somewhat more beneficial (cf. the drag efficiency factors for models 3, 5, and 6 having rounded leading edges with model 4 having a sharp leading edge). At $M = 2.8$ the cranked planforms generally had very nearly the same drag efficiency factors as the triangular planforms.

Theoretical.- For the wings with triangular panels, method 2 (ref. 3) gave subsonic drag-due-to-lift factors somewhat closer to the experimental factors than method 1 (ref. 2) (see figs. 14(a), (h), and (j)). The experimental factors for all the cranked wings, however, are considerably lower than predicted. This larger disparity between the theoretical and experimental values for the cranked wings results primarily because those planforms have higher lift-curve slopes than predicted. At supersonic Mach numbers, where practically no leading-edge thrust was realized for any of the planforms, the estimated drag-due-to-lift factors show fair to good agreement with the experimental factors, except for model 8. At supersonic Mach numbers, the agreement between the theoretical and experimental drag-due-to-lift factors is, generally, a reflection of the agreement of the lift-curve slopes of the respective models.

Minimum Drag

Experimental.- At subsonic speeds, the results presented in figure 15 indicate that the cranked planforms have lower minimum drag than the triangular planform, a result which can be explained partly by the fact that the spanwise distribution of exposed wing area provides lower skin friction for the cranked planforms (as indicated in ref. 8). At transonic speeds, all models with cranked planforms except model 2 show less minimum drag than model 1, mainly because of the more favorable longitudinal distribution of cross-sectional area for the models with cranked planforms. At $M = 2.94$, those cranked planforms with large leading-edge extensions had considerably

lower minimum drag than the triangular planform, although this wing volume was 50 percent or more greater than that for the triangular wing (cf. fig. 15(a) with figs. 15(h), (i), and (j)).

Theoretical.- As shown in figure 15, the minimum drag was predicted, generally, to within about 10 percent of the measured drag except for a few isolated cases at high supersonic Mach numbers. Near the highest Mach number, the minimum drag was higher than predicted, except for model 8. At $M = 1.1$ all cranked planforms, except model 2, had less drag than the triangular planform as predicted. For highly elongated models, such as model 8, the minimum drag at supersonic Mach numbers was considerably less than that for the triangular model because of the favorable longitudinal distribution of cross-sectional area.

Maximum Lift-Drag Ratio

Experimental.- The measured maximum lift-drag ratios (fig. 16) for the various wings are shown in the table below for four Mach numbers. The ratio of the volume of each cranked wing to the volume of the triangular wing is also shown.

Model	$\frac{(\text{Vol})_{\text{crank}}}{(\text{Vol})_{\text{tri}}}$	Maximum lift-drag ratio, $(L/D)_{\text{max}}$			
		$M = 0.4$	$M = 0.9$	$M = 1.2$	$M = 2.8$
1	1.00	7.3	8.5	7.1	5.6
2	1.05	7.9	8.8	7.3	5.4
3	1.16	7.7	8.9	7.6	5.6
4	1.10	7.1	8.4	7.4	5.5
5	1.42	7.8	9.0	7.3	5.6
6	.90	7.7	8.6	7.4	5.5
7	1.32	7.3	8.2	7.0	5.4
8	1.76	6.6	7.6	6.5	6.0
9	1.47	7.6	8.3	7.4	5.9
10	1.47	7.2	7.7	6.6	5.6

It can be seen that some of the cranked planforms (e.g., model 9) give some improvement in the maximum lift-drag ratio over that for the triangular planform at subsonic and supersonic speeds and yet have more usable volume adjacent to the fuselage. Similar improvements for an ogee planform over a triangular planform were reported in reference 1.

Theoretical comparison.- At subsonic speeds, the maximum lift-drag ratios predicted by method 2 (ref. 3) for planforms with triangular panels agreed somewhat better with the experimental values than values from method 1 (see figs. 16(a), (h), and (j)). Generally, the experimental lift-drag ratios shown in these figures were considerably larger than predicted at subsonic Mach numbers by either method because the predicted values of drag due to lift were too large. At supersonic Mach numbers, the theoretical maximum lift-drag

ratios agreed well with the experimental ratios except for model 8. For the latter model, both the measured drag due to lift and minimum drag were smaller than predicted as shown in figures 14(h) and 15(h).

Theoretical potential for L/D by warping.- Although the experimental study was limited to models with planar wings, it is important to note that a warped wing surface would improve the lift-drag ratio in cruising flight. To show the full theoretical potential of cranked planforms, the improvement in the lift-drag ratio to be expected from warping was calculated by the method of reference 4 which gives the optimum cambered wing surface and the associated pressure drag. The results from this study with the flight conditions assumed are given in the following table.

Assumed flight conditions:		
M = 3.0	Altitude = 70,000 ft	
S = 9,970 ft ²	C _L = 0.07	
Model	L/D Flat wing ^a	L/D Warped wing ^b
1 (Triangular wing)	6.8	6.85
9 (Cranked wings)	7.6	8.47

^aValues obtained by extrapolating the experimental L/D values to the flight Reynolds number at the selected C_L and M.

^bValues obtained from the flat-wing values by applying the calculated decrement in drag due to warping at the selected C_L and M.

The triangular wing with its supersonic leading edge gains little in lift-drag ratio from warping, whereas the cranked wing with its leading edge partially subsonic theoretically can be improved about 10 percent.

Aerodynamic Center Travel With Mach Number

Experimental.- The aerodynamic center (a.c.) travel with Mach number (fig. 17) was a maximum between subsonic and transonic Mach numbers and this maximum was nearly the same for the cranked planforms as for the triangular planform. However, for most of the cranked planforms at a Mach number of 2.94 the a.c. was either approximately the same or slightly ahead of its respective subsonic value. The more favorable a.c. travel with Mach number for the cranked planforms should result in smaller trim drag penalties. These a.c. movements with Mach number are summarized in the table below. The negative values represent rearward movements in a.c. with increased Mach number.

Model	$(\Delta a.c.)_{\max_{M=0.4 \rightarrow M_{trans}}}$	$(\Delta a.c.)_{M=0.4 \rightarrow 2.94}$
1	-0.15 \bar{c}	-0.08 \bar{c}
2	-.11 \bar{c}	-.02 \bar{c}
3	-.15 \bar{c}	.01 \bar{c}
7	-.15 \bar{c}	.06 \bar{c}
8	-.14 \bar{c}	.05 \bar{c}
9	-.16 \bar{c}	-.01 \bar{c}
10	-.13 \bar{c}	-.03 \bar{c}

Theoretical.- At subsonic Mach numbers, for the planforms with triangular wing panels, the experimental variation of a.c. with Mach number agreed better with the theoretical variation given by method 2 than by method 1 (see figs. 17(a), (h), and (j)). For those models without triangular wing panels, method 1, in which the lift is arbitrarily placed on the 25-percent chord line, gives an inadequate estimate of the aerodynamic movement with Mach number. At supersonic Mach numbers, the variation in a.c. location with Mach number was generally predicted correctly, although the absolute location of the a.c. was not closely predicted for models 8 and 10, as shown in figures 17(h) and 17(j), respectively. The discrepancy between the theoretical and experimental a.c. locations for these two models was probably related to an inaccurate assumption of the location of the center of pressure on the body in the presence of the wing.

Reynolds Number Effects

As an aid in interpreting the subsonic results obtained with the small models investigated herein at a Reynolds number of only 0.89 million, results are presented for two larger scale models of models 1 and 11, which had been investigated previously in the Ames 40- by 80-Foot Wind Tunnel at a Reynolds number of 13.7 million and a Mach number of 0.10. Data in figure 18(a) indicate practically no Reynolds number effect on either the lift or pitching-moment curves for model 1;⁶ however, data in figure 18(b) indicate a slight Reynolds number effect on the minimum drag and the drag due to lift. Part of the reason for the higher minimum drag in the 40- by 80-foot wind tunnel is the strut drag and strut influence on the wing drag. A three-strut support system was used in the 40- by 80-foot wind tunnel and a sting support was used in the 2- by 2-foot wind tunnel. For model 11, data in figure 19(a) indicate only a slight Reynolds number effect on the pitching-moment curves and the lift-curve slope at the higher angles of attack, the higher value being measured for the model at the higher Reynolds number of 13.7 million. As shown in figure 19(b), practically no Reynolds number effect was indicated for the drag due to lift, but the minimum drag is again higher for the model investigated at the higher Reynolds number in the 40- by 80-foot wind tunnel.

⁶A similar result can be noted for a sharp-edged triangular wing with an aspect ratio of 2.0 by comparing the lift and pitching-moment data obtained at a Reynolds number of 1.8 million (ref. 9) with those obtained at a Reynolds number of 15.4 million (ref. 10).

CONCLUSIONS

From an investigation of several wing-body combinations employing wings of cranked planforms throughout a Mach number range from 0.4 to 2.94, the following conclusions can be drawn.

(1) Large leading-edge extensions on the cranked planforms severely reduced static longitudinal stability at high angles of attack. There was evidence that models that tended to be longitudinally unstable at $M = 0.4$ would have similar tendencies at $M = 2.94$ at the higher angles of attack.

(2) A small leading-edge extension produced a nonlinear lift curve and reduced the angle of attack required to attain a given high lift coefficient, but large extensions increased this angle.

(3) Although the maximum travel in a.c. location with a change from subsonic to transonic Mach numbers was not greatly different for any of the planforms, with the leading-edge extensions the a.c. location was approximately the same at Mach numbers of 0.40 and 2.94.

(4) At $M = 0.4$ some of the cranked planforms with round-nosed profiles had less drag due to lift than the triangular planform with a sharp-nosed profile; a cranked planform with a round-nosed profile on only the leading-edge extension also had less drag. The advantage, however, was not realized at supersonic Mach numbers.

(5) Some of the cranked planforms had greater aerodynamic efficiency than the triangular planform, as reflected in the maximum lift-drag ratio at subsonic and supersonic Mach numbers. These wings also had considerably more usable volume than the triangular planform.

(6) At low subsonic Mach numbers, practically no Reynolds number effect was indicated for the pitching-moment results obtained for two of the models at Reynolds numbers of 0.89 and 13.7 million.

(7) At supersonic Mach numbers, the experimental lift-drag ratios agreed generally with the values predicted by linear theory combined with lift carry-over factors from slender-body theory.

(8) The maximum lift-drag ratio of one cranked planform was not only higher than that of the triangular planform but, theoretically, warping would have improved this ratio about 10 percent at flight Reynolds number.

Ames Research Center

National Aeronautics and Space Administration

Moffett Field, Calif., 94035, July 24, 1967

720-01-00-02-00-21

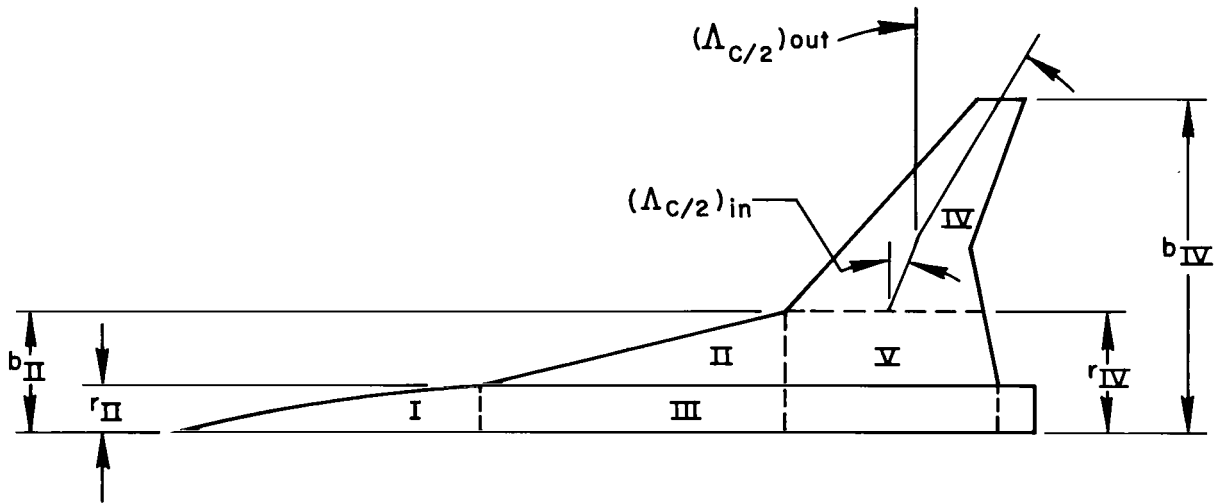
APPENDIX A

SUBSONIC THEORY

Two methods will be presented for computing the lift and pitching-moment parameters at subsonic Mach numbers. Lift on the body and on the forward extensions of the cranked wings and the lift carry-over factors are the same for both methods. However, these methods differ in the theory chosen to estimate the lift and center of pressure on the primary lift producing panels (the outboard panels). In method 1, the DeYoung "rule of thumb" method (ref. 2) was used to estimate the primary panel lift and in method 2 the Lomax-Sluder theory (ref. 3) was used to estimate this panel lift. Details of method 1 and method 2 will be discussed below.

Method 1

Lift.- The lift-curve slope for each wing-body combination was computed as the sum of the contributions from the individual components. The areas and dimensions associated with these components are shown in the sketch below.



The lift-curve slope of the body nose $(C_{L_{\alpha}})_I$ was computed from slender-body concepts presented in reference 5 as

$$(C_{L_{\alpha}})_I = \frac{2S_b}{S_{ref}} \quad (A1)$$

where

S_b maximum cross-sectional area of the body

S_{ref} reference area of the triangular wing (21.75 in.²)

The lift-curve slope of area II without body-induced effects $(C_{L\alpha})_{II}$ was computed by the theory of reference 3. The lift-curve slope of area II with body-induced effects accounted for was obtained by multiplying $(C_{L\alpha})_{II}$ by the slender-body factor, $K_{W(B)}$, from chart I of reference 5 for a given r_{II}/b_{II} . The lift-curve slope of area III was computed by applying the slender-body factor $K_{B(W)}$ from chart I of reference 2 to $(C_{L\alpha})_{II}$ for a given r_{II}/b_{II} . The total lift-curve slope of areas II and III, $(C_{L\alpha})_{II+III}$, becomes

$$(C_{L\alpha})_{II+III} = (C_{L\alpha})_{II} [K_{W(B)} + K_{B(W)}] r_{II}/b_{II} \frac{S_{II}}{S_{ref}} \quad (A2)$$

where S_{II} denotes area II.

To compute the lift-curve slope of area IV, an effective sweep angle of the midchord line was first determined as

$$\Lambda_{eff} = \cos^{-1} \left[\frac{\cos(\Lambda_{c/2})_{in} S_{in} + \cos(\Lambda_{c/2})_{out} S_{out}}{S_{in} + S_{out}} \right] \quad (A3)$$

where

S_{in} wing area between r_{IV} and the trailing-edge notch point in area sketch

S_{out} wing area between the trailing-edge notch point and the wing tip in area sketch

This effective sweep angle was used in the DeYoung rule of thumb method (ref. 2) to find the wing-alone lift-curve slope of area IV, $(C_{L\alpha})_{IV}$. This method was chosen because it is simple and gives approximately the same result for low-aspect-ratio wings as the more complicated Weissinger method (ref. 11) which gives an accurate prediction of lift-curve slope at subsonic speeds. The lift-curve slope of area IV, with body induction included, was computed by multiplying the slender-body factor $K_{W(B)}$ from chart 1 of reference 5 times $(C_{L\alpha})_{IV}$ for a given r_{IV}/b_{IV} . Then the lift-curve slope of area V was computed by multiplying $(C_{L\alpha})_{IV}$ times the factor $K_{B(W)}$ from reference 5 for a given r_{IV}/b_{IV} . The total lift-curve slope of area IV and V becomes

$$(C_{L\alpha})_{IV+V} = \left[\frac{2\pi A}{\beta A + 2 \left(\frac{4 \cos \Lambda_{eff} + \beta A}{2 \cos \Lambda_{eff} + \beta A} \right)} \right]_{IV} [K_{W(B)} + K_{B(W)}] r_{IV}/b_{IV} \frac{S_{IV}}{S_{ref}} \quad (A4)$$

where

A aspect ratio of area IV, $\frac{4(b_{IV} - r_{IV})^2}{S_{IV}}$

β $\sqrt{1 - M^2}$

M Mach number

Λ_{eff} effective sweep angle defined by equation (A3)

The lift-curve slope for the entire wing-body combination at subsonic speeds, therefore, is

$$C_{L\alpha} = (C_{L\alpha})_I + (C_{L\alpha})_{II+III} + (C_{L\alpha})_{IV+V} \quad (A5)$$

Pitching moment. - The center of pressure for the body nose, S_I , was taken from chart 9 of reference 5. No additional corrections were applied because the nose was a Sears-Haack nose rather than the ogival nose of chart 9; this small difference in the noses would have small effect on the final results.

The center of pressure of area II was taken from figure 14 of reference 3. Center of pressures of areas III and V were computed separately from chart 16 of reference 5 for values of βA of areas II and IV and their respective r/s values (r_{II}/b_{II} and r_{IV}/b_{IV}).

Implicit in the application of the Prandtl-Glauert compressibility rule to the Weissinger method presented in reference 2, the span-load distribution with compressibility effects accounted for is considered to be carried by the 1/4-chord line of the undistorted wing. In method 1 herein, with an elliptic span load assumed on area IV, it follows that the centroid of this load will act on the 1/4-chord line at a lateral distance out from the leading-edge notch point of (0.424) ($b_{IV} - r_{IV}$). This 1/4-chord line was taken as that for the equivalent planform with its midchord sweep defined by equation (A3).

Finally, the slope of the pitching-moment curve was computed as

$$\frac{\partial C_m}{\partial C_L} = \frac{l_I(C_{L\alpha})_I + l_{II}(C_{L\alpha})_{II} + l_{III}(C_{L\alpha})_{III} + l_{IV}(C_{L\alpha})_{IV} + l_V(C_{L\alpha})_V}{\bar{c}[(C_{L\alpha})_I + (C_{L\alpha})_{II} + (C_{L\alpha})_{III} + (C_{L\alpha})_{IV} + (C_{L\alpha})_V]} \quad (A6)$$

where

l_I, l_{II}, l_{III}
 $l_{IV},$ and l_V distances from the assumed pitching-moment center to the center of pressures of each area shown in the area sketch (positive distances are ahead of the pitching-moment center)

\bar{c} mean aerodynamic chord of the triangular wing (4.218 in.)

Skin-friction drag.- The skin-friction drag coefficient was computed by integrating the average skin-friction coefficients over the entire surface of each model and then adjusting the result by the appropriate ratio of wetted area to reference area. The average skin-friction coefficient at a local spanwise station was computed from the Schlichting incompressible equation given in reference 6 adjusted for compressibility by the T' method of reference 7 as

$$C_{F_{av}} = \frac{0.455(C_F/C_{F_i})}{(\log_{10} R_x)^{2.58}} \quad (A7)$$

where

C_F/C_{F_i} compressibility factor for a turbulent boundary layer given explicitly by equation (A6) of reference 1

R_x Reynolds number based on the local reference length (either the local wing chord or the body length)

In these calculations, the complete model was treated as a sharp-edged flat plate; therefore, wing thickness effects, body three-dimensional effects, and leading-edge bluntness effects were estimated to be small and were not taken into account.

Drag due to lift.- In all cases, since the wings were thin and of low aspect ratio, drag due to lift was assumed to be equal to the lift times the angle of attack; hence, no leading-edge thrust was assumed. For symmetrical models, the drag-due-to-lift factor ($\partial C_D / \partial C_L^2$) becomes the reciprocal of the lift-curve slope.

Maximum lift-drag ratio.- In accordance with the above assumptions, a parabolic drag polar was assumed so that the maximum lift-drag ratio is

$$\left(\frac{L}{D}\right)_{\max} = \frac{1}{2} \sqrt{\frac{C_{L\alpha}}{C_{D_0}}} \quad (A8)$$

where

$C_{L\alpha}$ lift-curve slope per radian

C_{D_0} minimum drag coefficient

Method 2

In reference 1 it was found that the low-speed theory of Lomax-Sluder for low-aspect-ratio triangular wings (ref. 3) gave a better estimate of lift and center of pressure for this type wing than the theory of Weissinger (ref. 11). For this reason, the lift and center of pressure for area IV of

the wings with triangular panels, models 1, 8, and 10, were also computed by the Lomax-Sluder theory. This method, in which the lift and center of pressure for all areas except area IV were computed as described for method 1, is designated method 2.

APPENDIX B

SUPERSONIC THEORY

Method 3

Lift and pitching moment.- The estimates of the lift and pitching-moment curve slopes for the wing alone were made by the method of reference 4. A similar but alternate method of computing the wing-alone values is given in reference 12.

The mutual interference effects between the body and the wing lift were calculated by the method of reference 5. Again, the lift and pitching moments from the body nose were calculated by slender-body concepts as presented in appendix A. The center of pressure on the cylindrical portion of the body from which the pitching moments were derived was assumed to lie at 50 percent of the root chord.

Drag.- Skin-friction drag was computed by equation (A7). Wave drag was computed for an "equivalent" body of revolution for each wing-body combination by application of the supersonic area rule (ref. 1).

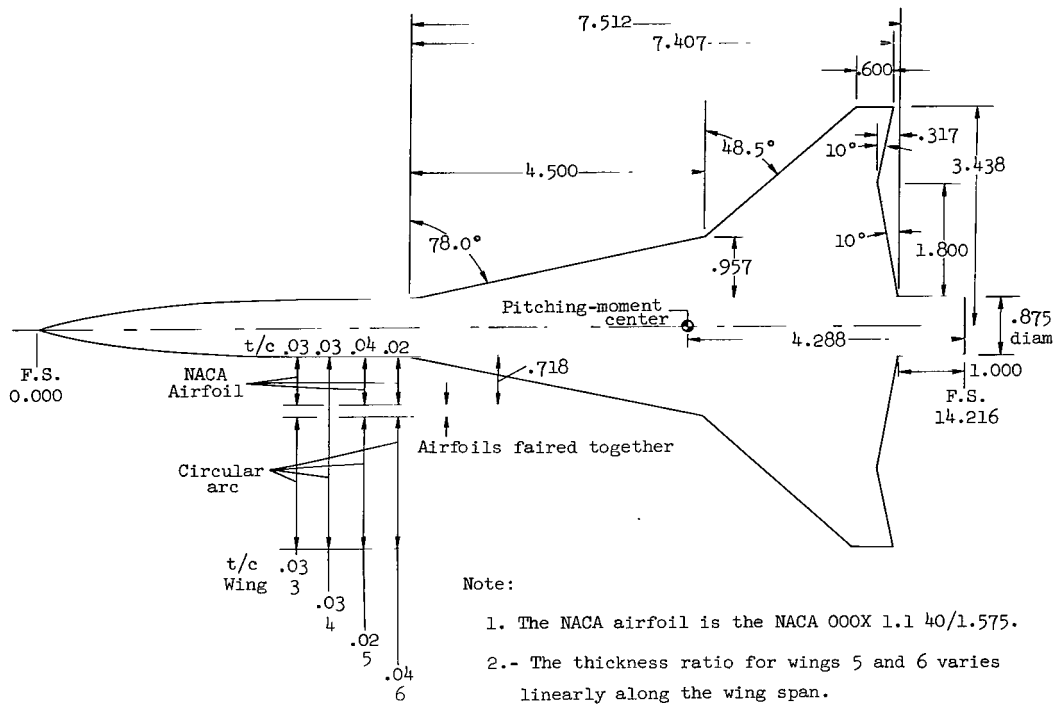
Drag due to lift and maximum lift-drag ratio.- In computing the drag due to lift, no leading-edge thrust was assumed; therefore, the drag due to lift was assumed to be equal to the lift times the angle of attack. In accordance with this assumption, the maximum lift-drag ratio was computed by equation (A8).

REFERENCES

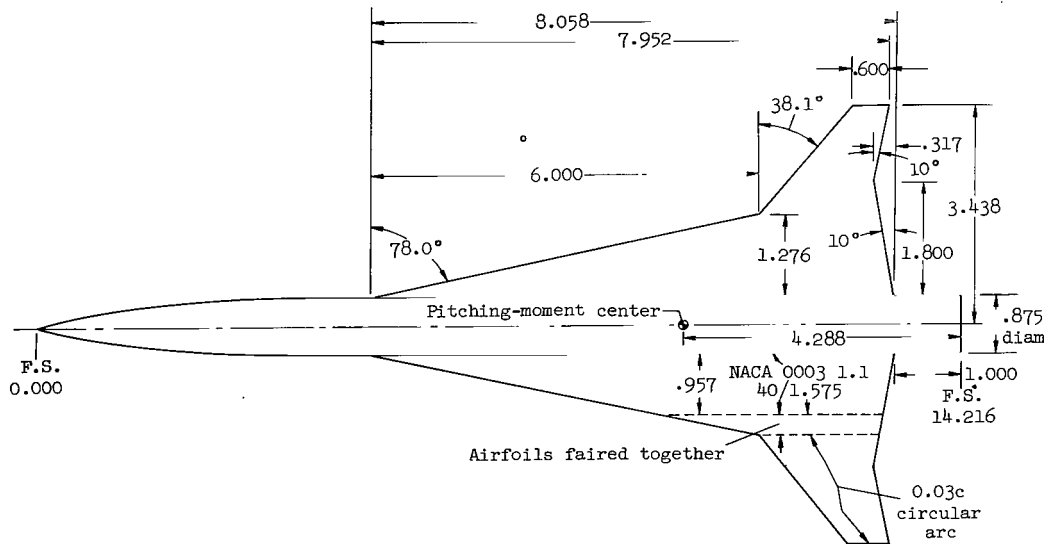
1. Hicks, Raymond M.; and Hopkins, Edward J.: Effects of Spanwise Variation of Leading-edge Sweep on the Lift, Drag, and Pitching Moment of a Wing-Body Combination at Mach Numbers From 0.7 to 2.94. NASA TN D-2236, 1964.
2. DeYoung, John: Rule of Thumb Equation for Predicting Lifting-Surface-Theory Values of Lift. J. Aero. Sci., vol. 24, no. 8, Aug. 1957, p. 629.
3. Lomax, Harvard; and Sluder, Loma: Chordwise and Compressibility Corrections to Slender-Wing Theory. NACA Rept. 1105, 1952.
4. Woodward, F. A.: A Method of Aerodynamic Influence Coefficients With Application to the Analysis and Design of Supersonic Wings. Boeing Document D6-8178, April 1962.
5. Pitts, William C.; Neilsen, Jack N.; and Kaattari, George E.: Lift and Center of Pressure of Wing-Body-Tail Combinations at Subsonic, Transonic, and Supersonic Speeds. NACA Rept. 1307, 1957.
6. Schlichting, Hermann (J. Kestin, trans.): Boundary Layer Theory. McGraw-Hill Book Co., Inc., 1955, p. 540.
7. Sommer, Simon C.; and Short, Barbara J.: Free-Flight Measurements of Turbulent Boundary-Layer Skin Friction in the Presence of Severe Aerodynamic Heating at Mach Numbers From 2.8 to 7.0. NACA TN 3391, 1955.
8. Hopkins, Edward J.: Some Effects of Planform Modification on the Skin Friction Drag. AIAA J., vol. 2, no. 2, Feb. 1964, pp. 413-414.
9. Rose, Leonard M.: Low-Speed Investigation of a Small Triangular Wing of Aspect Ratio 2.0. II. Flaps. NACA RM A7L11, 1948.
10. Anderson, Adrien E.: An Investigation at Low Speed of a Large-Scale Triangular Wing of Aspect Ratio Two. I. Characteristics of a Wing Having a Double-Wedge Airfoil Section With Maximum Thickness at 20-Percent Chord. NACA RM A7F06, 1947.
11. DeYoung, John; and Harper, Charles W.: Theoretical Symmetric Span Loading at Subsonic Speeds for Wings Having Arbitrary Plan Form. NACA Rept. 921, 1948.
12. Middleton, Wilbur D.; and Carlson, Harry W.: A Numerical Method for Calculating the Flat-Plate Pressure Distributions on Supersonic Wings of Arbitrary Planform. NASA TN D-2570, 1965.

TABLE I. - ESTIMATED SKIN-FRICTION AND LEADING-EDGE BLUNTNES-DRAG CORRECTIONS

M	$\Delta C_{D_{SF}}$	ΔC_{D_B}	M	$\Delta C_{D_{SF}}$	ΔC_{D_B}
Model 1			Model 6		
0.4	0.0032	0	0.4	0.0030	0
.7	.0032	0	.7	.0027	0
.9	.0033	0	.9	.0026	0
1.0	.0034	0	1.0	.0026	0
1.1	.0035	0	1.1	.0027	0
1.4	.0039	0	1.4	.0029	0
1.98	.0027	.0004	1.98	.0030	.0011
2.94	.0027	.0006	2.94	.0026	.0011
Model 2			Model 7		
.4	.0033	0	.4	.0031	0
.7	.0029	0	.7	.0023	0
.9	.0027	0	.9	.0020	0
1.0	.0027	0	1.0	.0021	0
1.1	.0027	0	1.1	.0022	0
1.4	.0030	0	1.4	.0026	.0009
1.98	.0034	.0007	1.98	.0025	.0009
2.94	.0025	.0007	2.94	.0020	.0009
Model 3			Model 8		
.4	.0030	0	.4	.0015	0
.7	.0027	0	.7	.0014	0
.9	.0026	0	.9	.0013	0
1.0	.0026	0	1.0	.0013	0
1.1	.0027	0	1.1	.0012	0
1.4	.0029	0	1.4	.0012	0
1.98	.0030	.0003	1.98	.0018	.0003
2.94	.0026	.0003	2.94	.0015	.0003
Model 4			Model 9		
.4	.0030	0	.4	.0020	0
.7	.0027	0	.7	.0019	0
.9	.0026	0	.9	.0018	0
1.0	.0026	0	1.0	.0018	0
1.1	.0027	0	1.1	.0018	0
1.4	.0029	0	1.4	.0019	0
1.98	.0030	.0006	1.98	.0024	.0002
2.94	.0026	.0006	2.94	.0019	.0002
Model 5			Model 10		
.4	.0030	0	.4	.0030	0
.7	.0027	0	.7	.0029	0
.9	.0026	0	.9	.0028	0
1.0	.0026	0	1.0	.0027	0
1.1	.0027	0	1.1	.0027	0
1.4	.0029	0	1.4	.0024	0
1.98	.0030	.0007	1.98	.0024	.0003
2.94	.0026	.0007	2.94	.0019	.0003

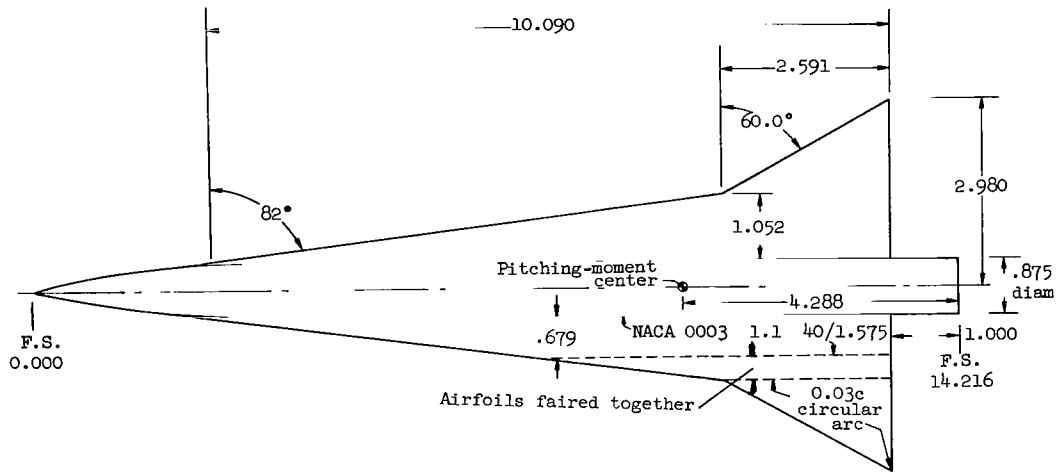


(c) Models 3, 4, 5, 6

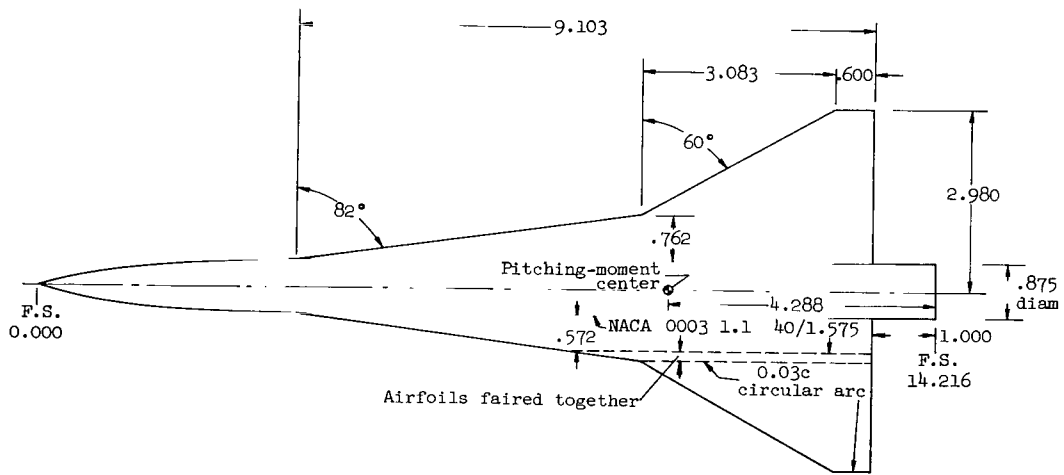


(d) Model 7

Figure 1.- Continued.

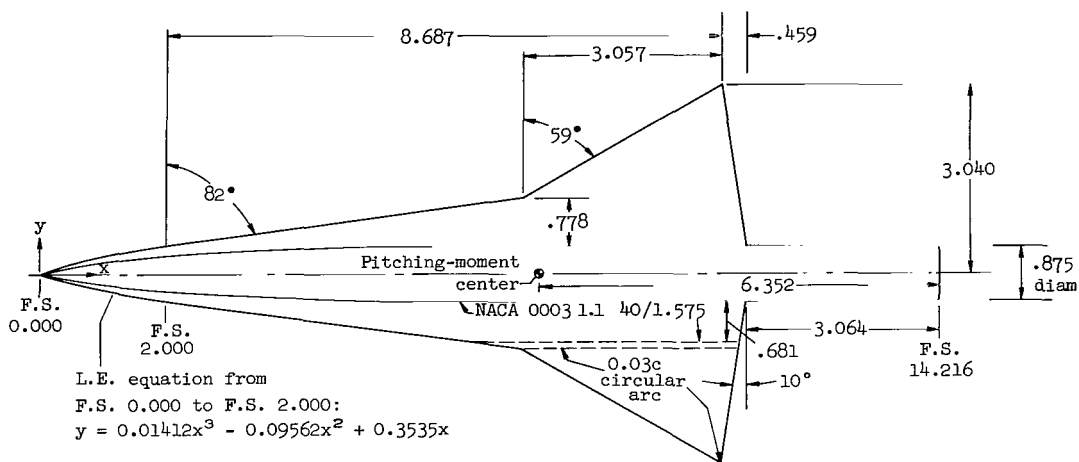


(e) Model 8

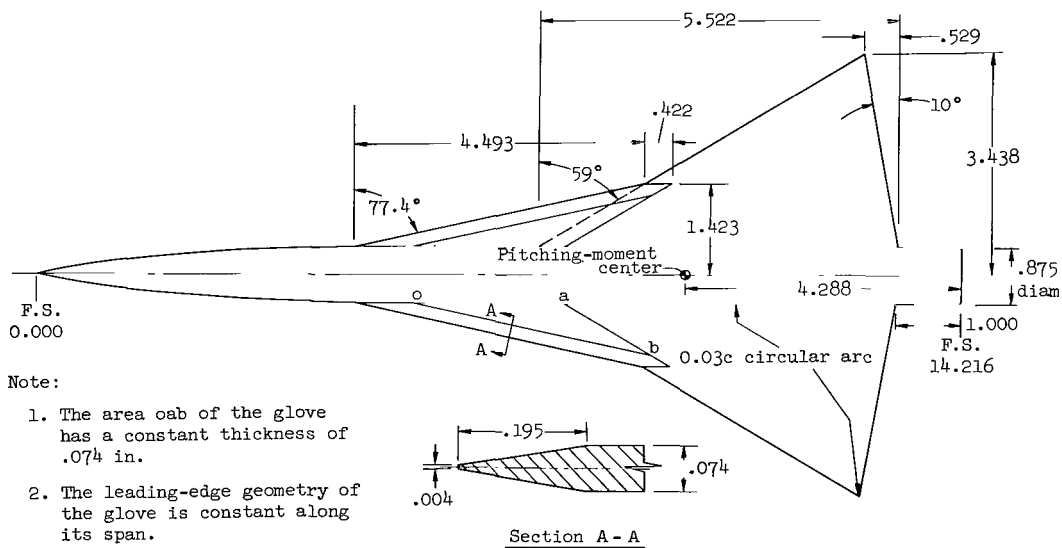


(f) Model 9

Figure 1.- Continued.



(g) Model 10



(h) Model 11

Figure 1.- Concluded.

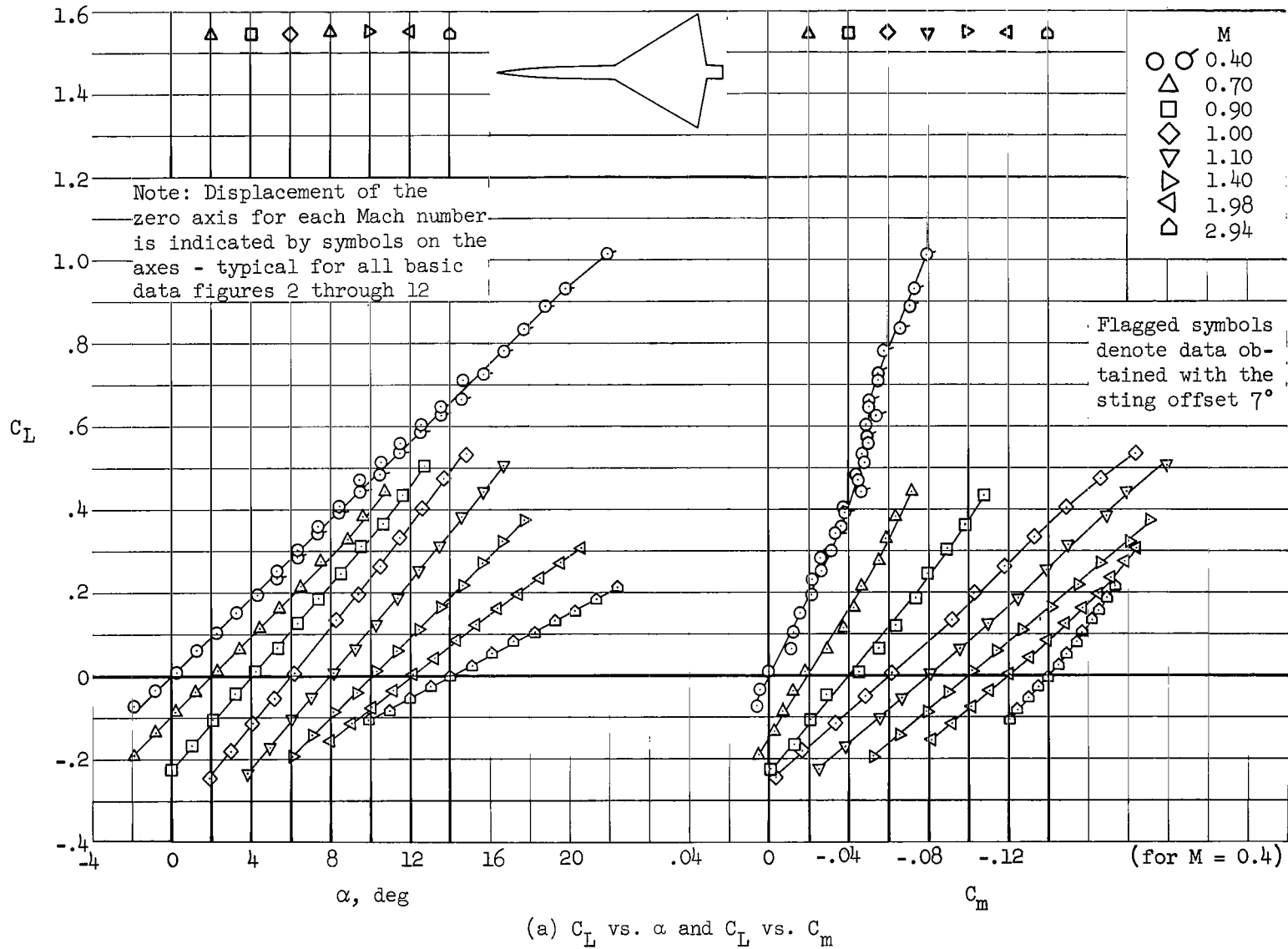
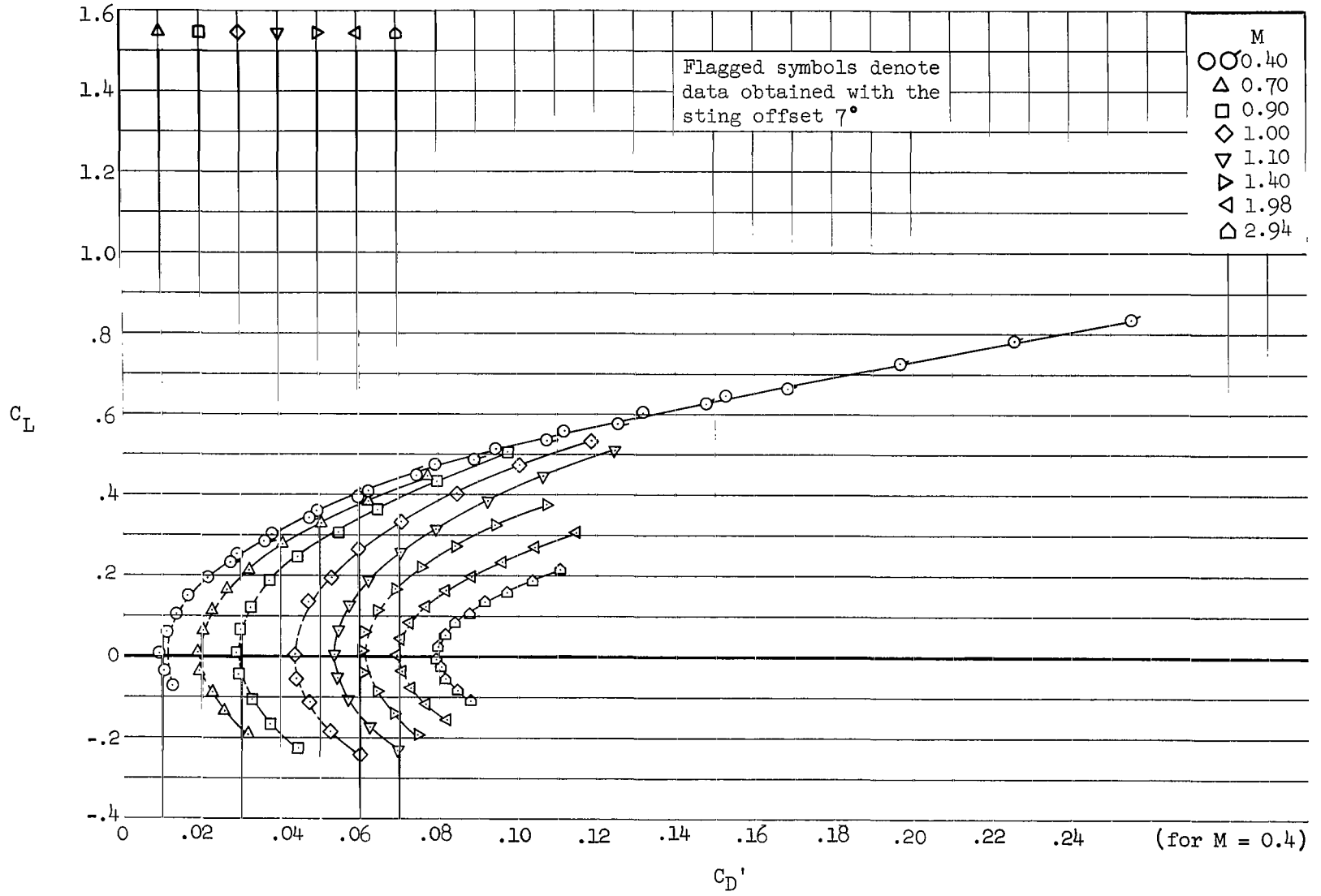
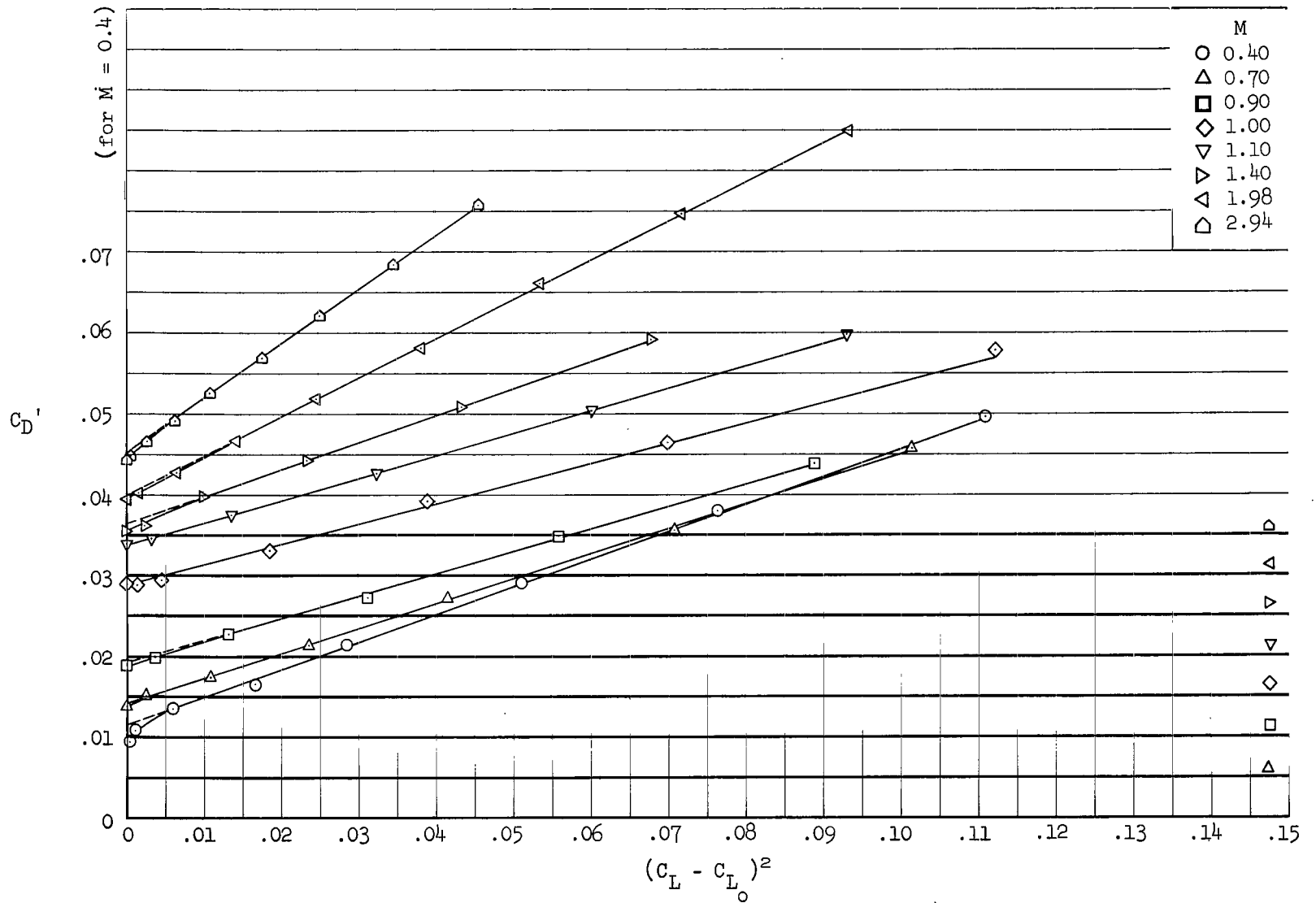


Figure 2.- Lift, drag, and pitching-moment characteristics of model 1.



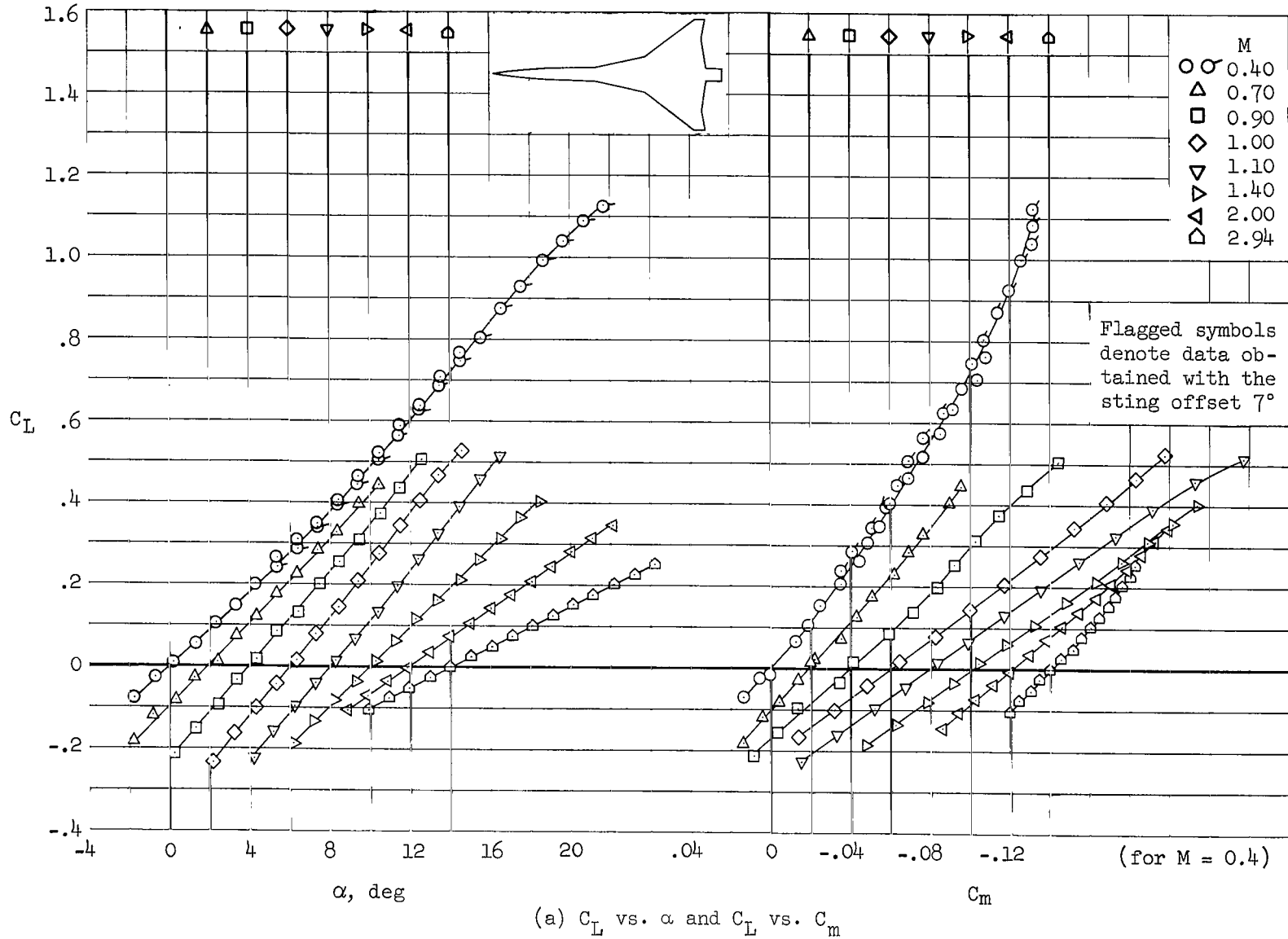
(b) C_L vs. C_D'

Figure 2.- Continued.



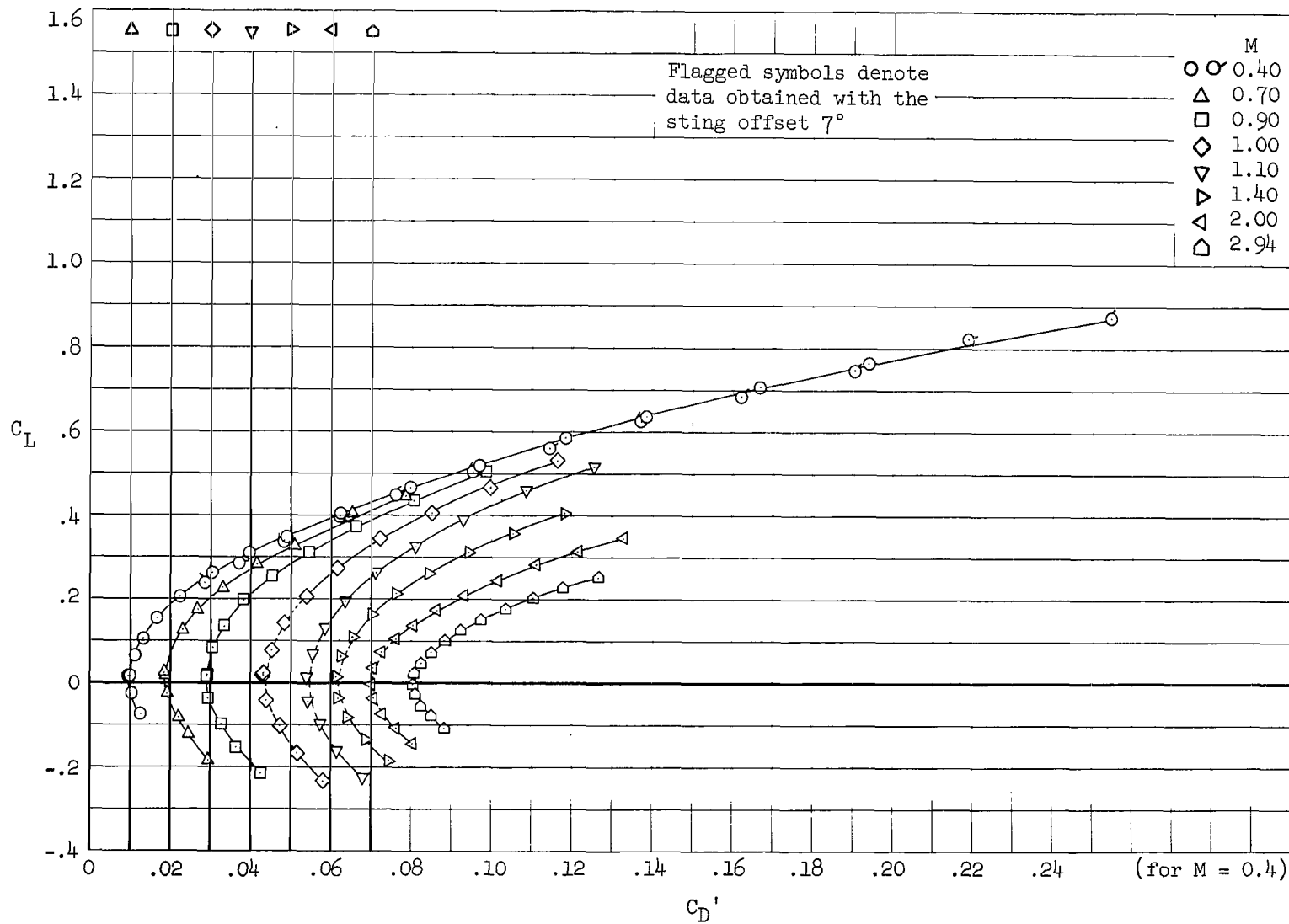
(c) C_D' vs. $(C_L - C_{L_0})^2$

Figure 2.- Concluded.



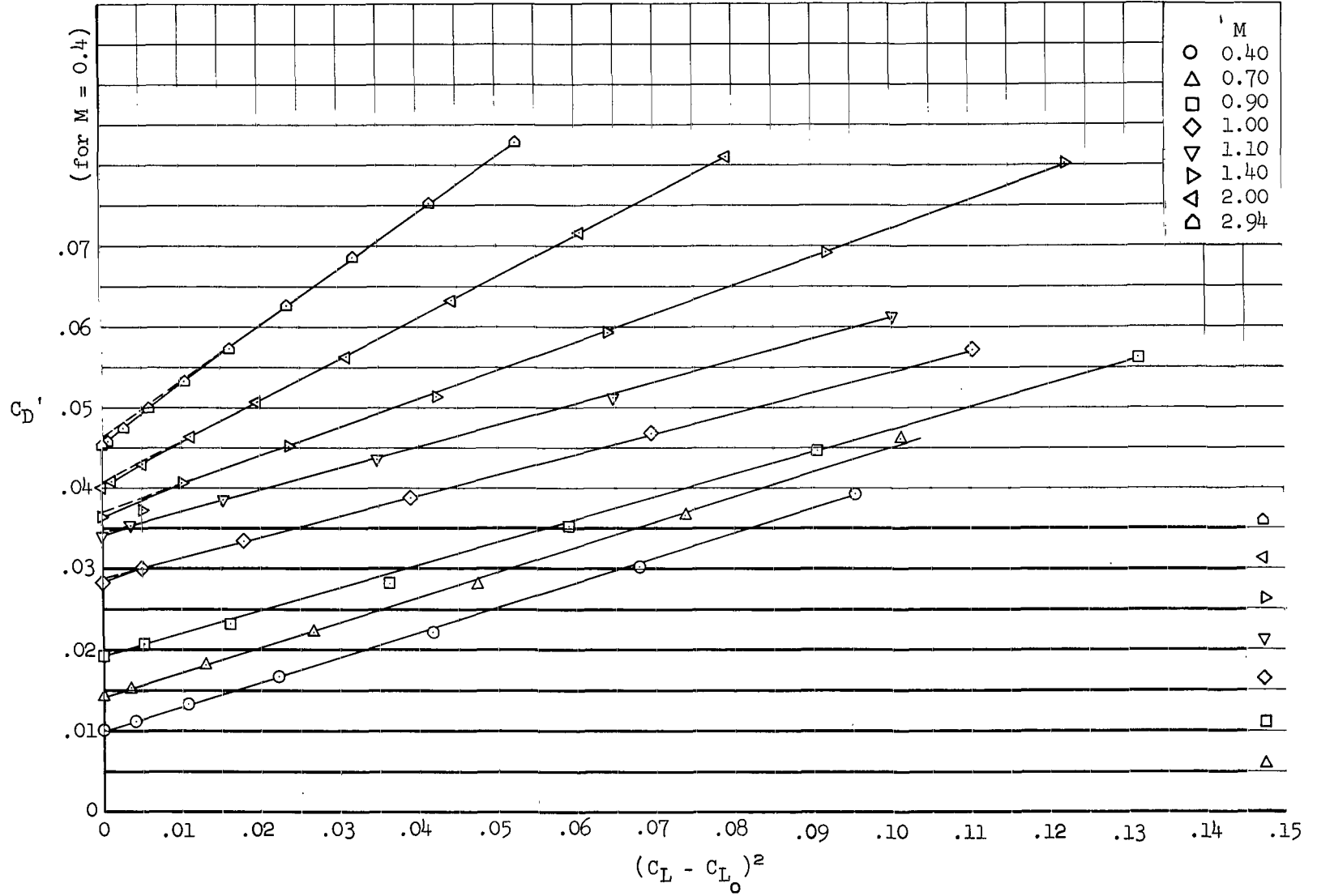
(a) C_L vs. α and C_L vs. C_m

Figure 3.- Lift, drag, and pitching-moment characteristics of model 2.



(b) C_L vs. C_D'

Figure 3.- Continued.



(c) C_D' vs. $(C_L - C_{L_0})^2$

Figure 3.- Concluded.

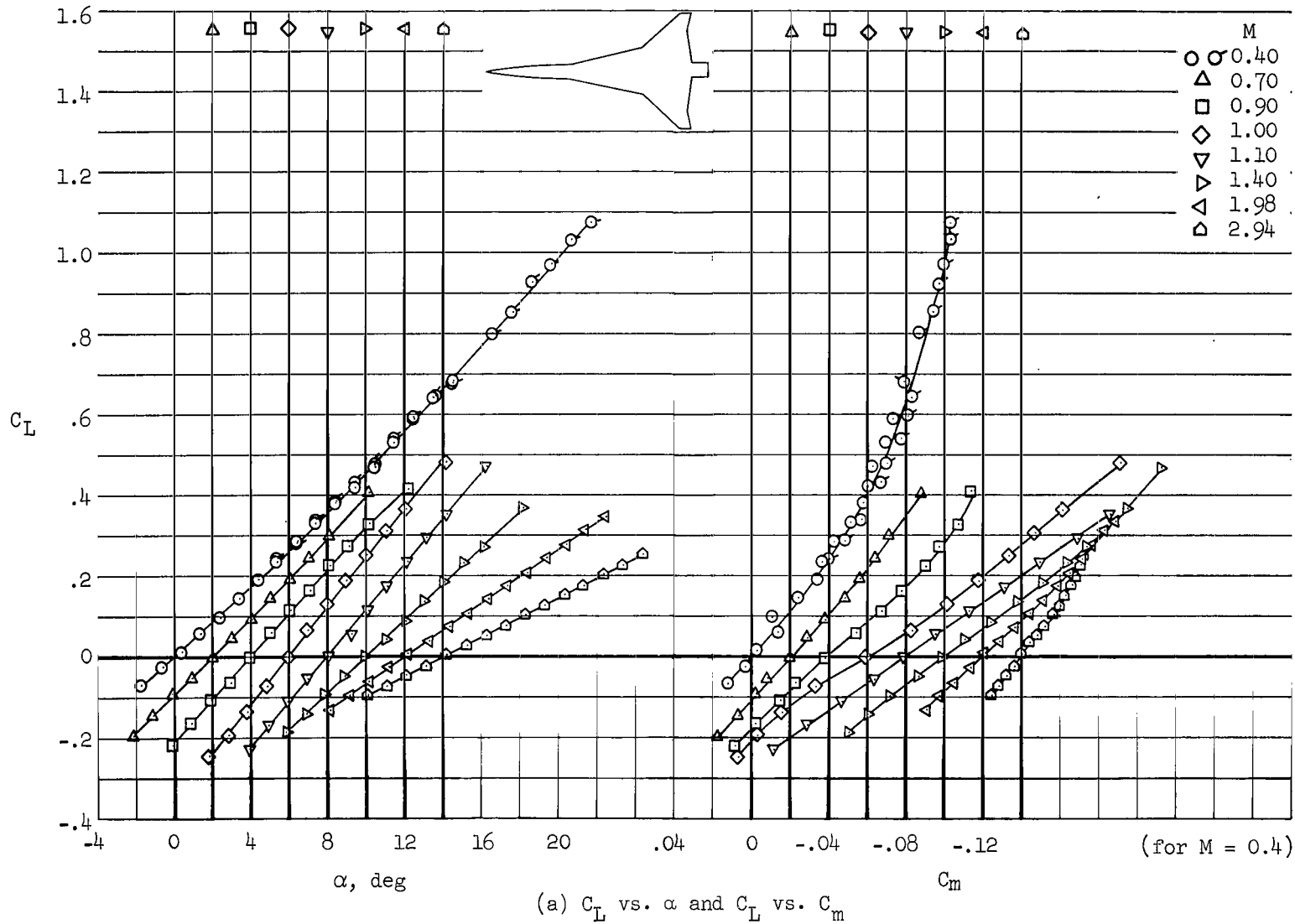
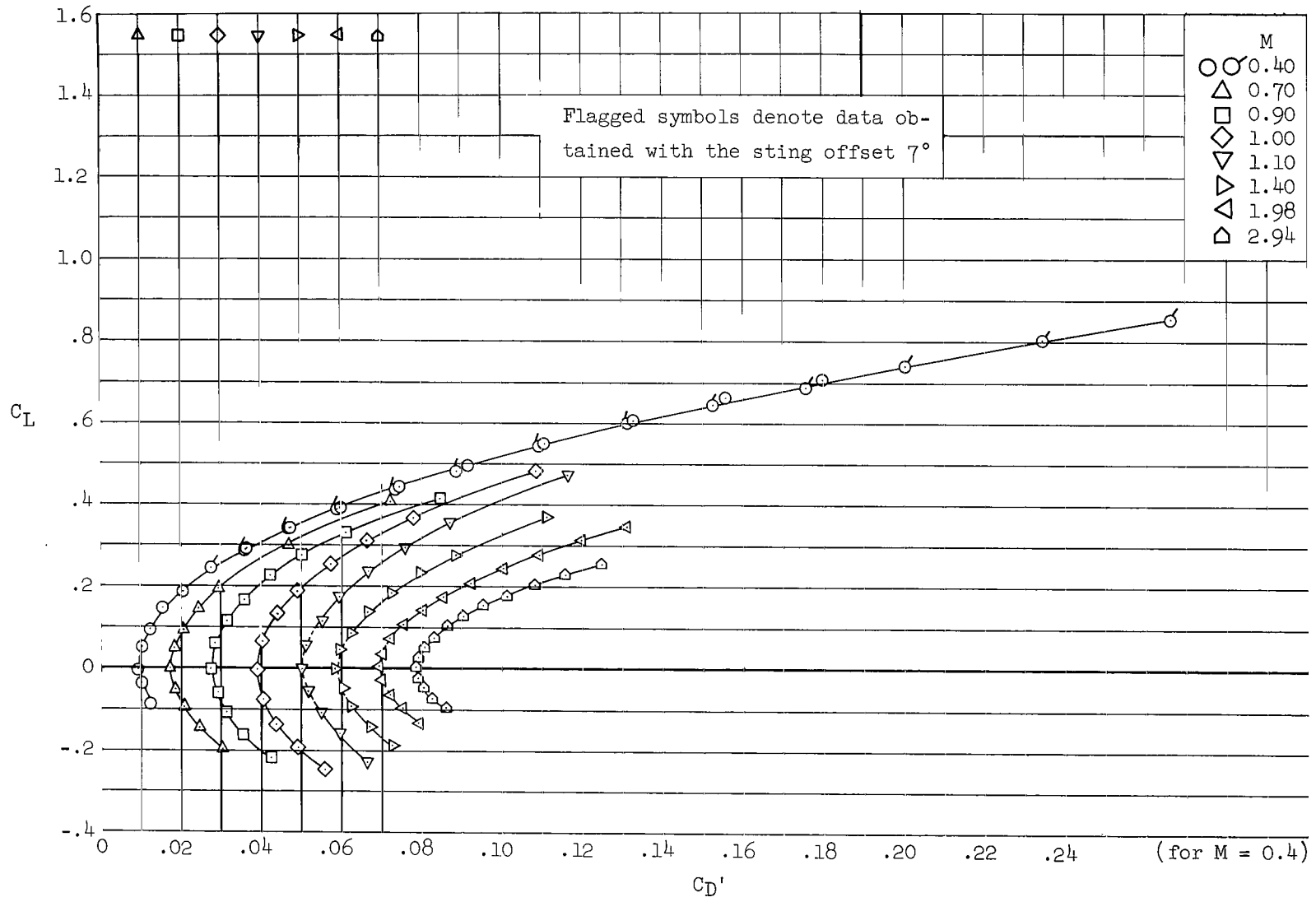
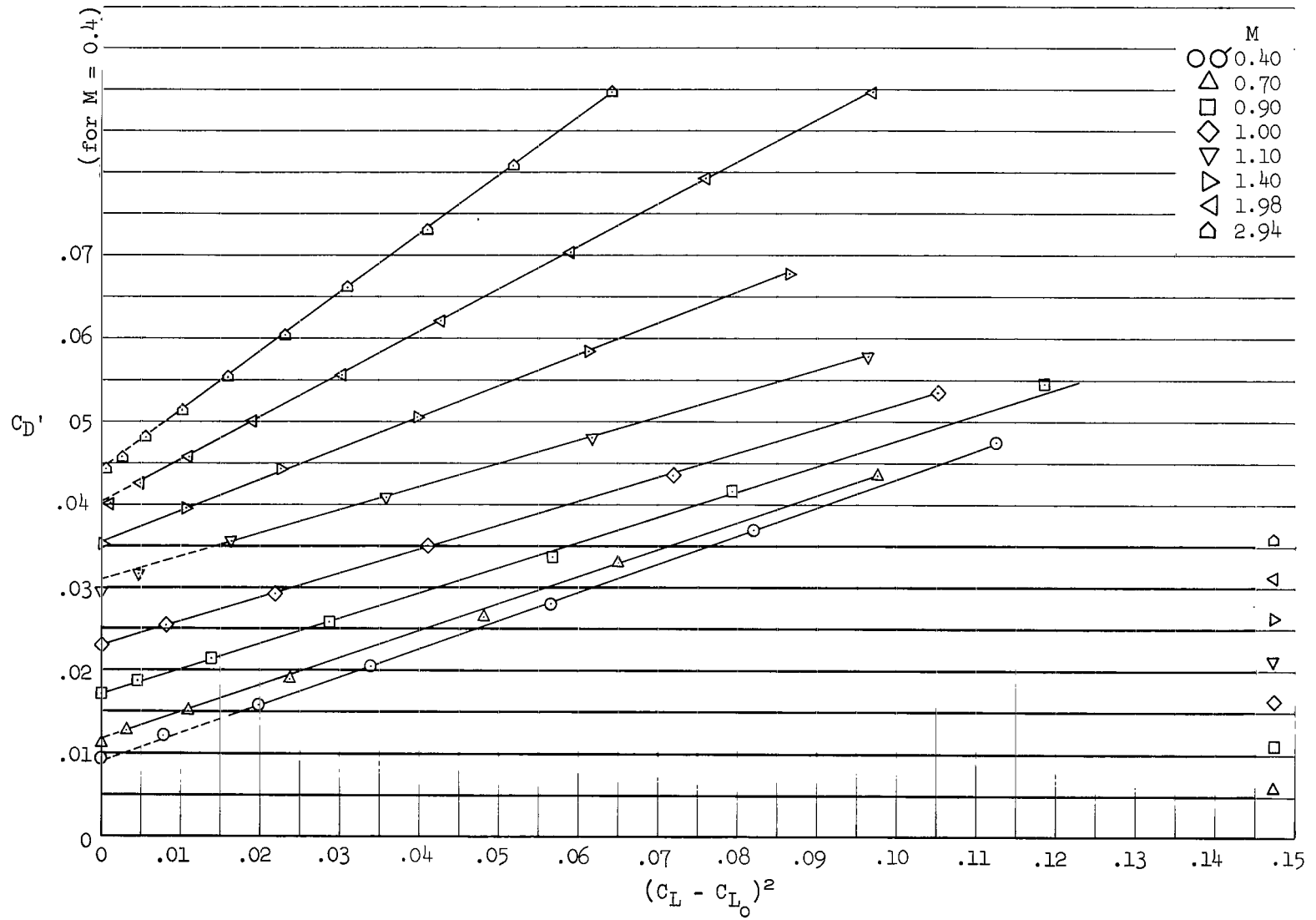


Figure 4.- Lift, drag, and pitching-moment characteristics of model 3.



(b) C_L vs. C_D'

Figure 4.- Continued.



(c) C_D' vs. $(C_L - C_{L_0})^2$

Figure 4.- Concluded.

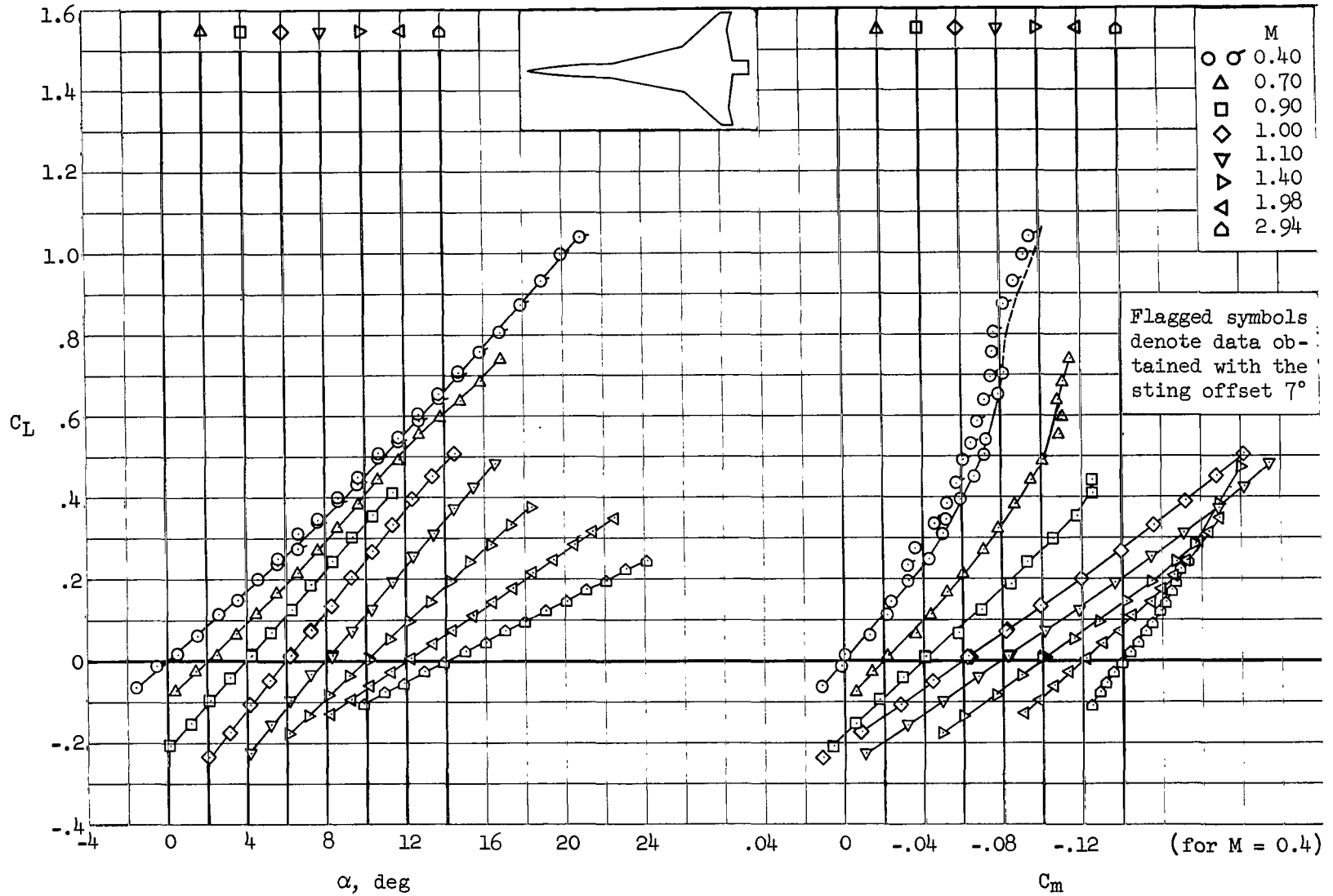
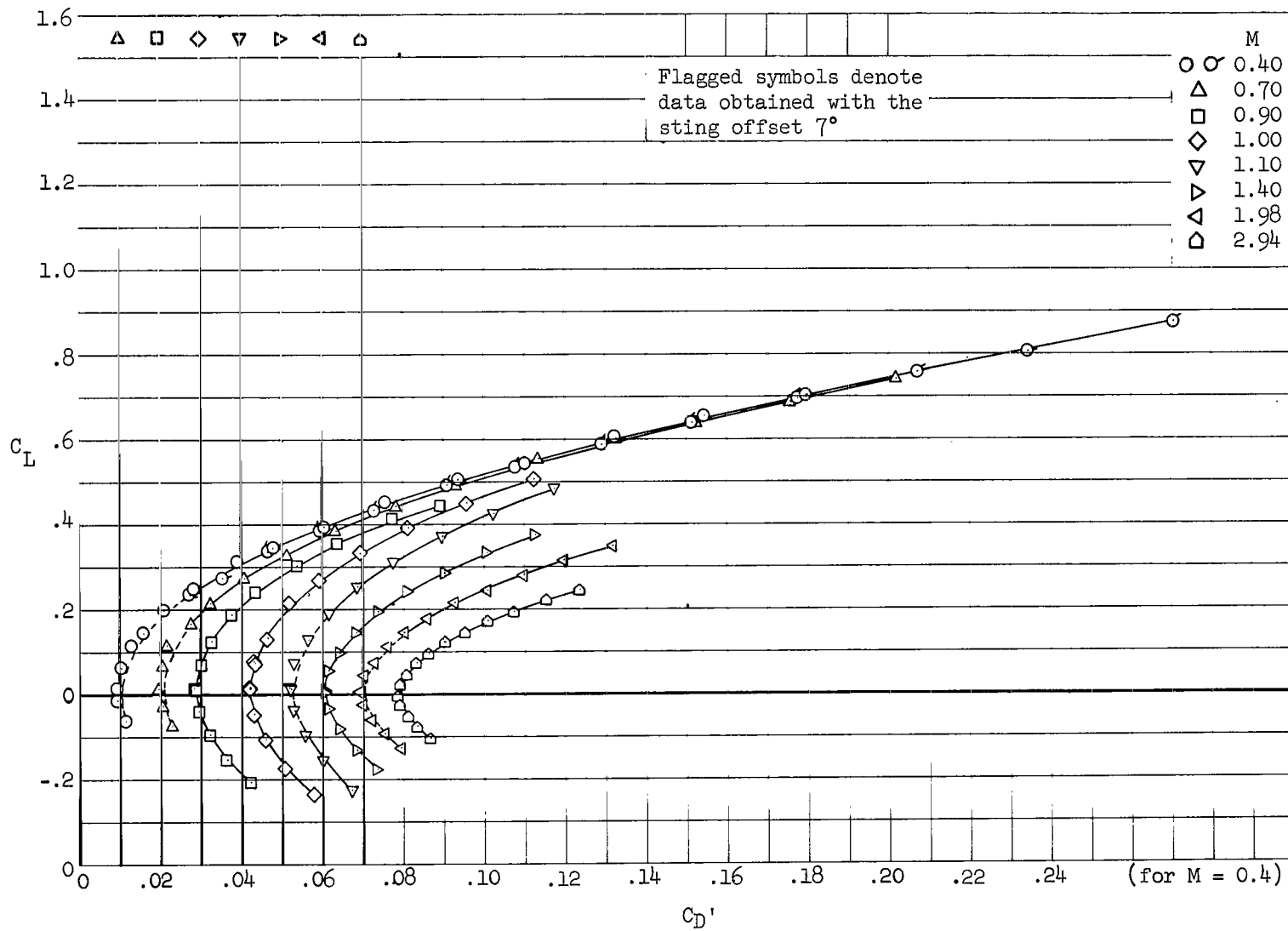
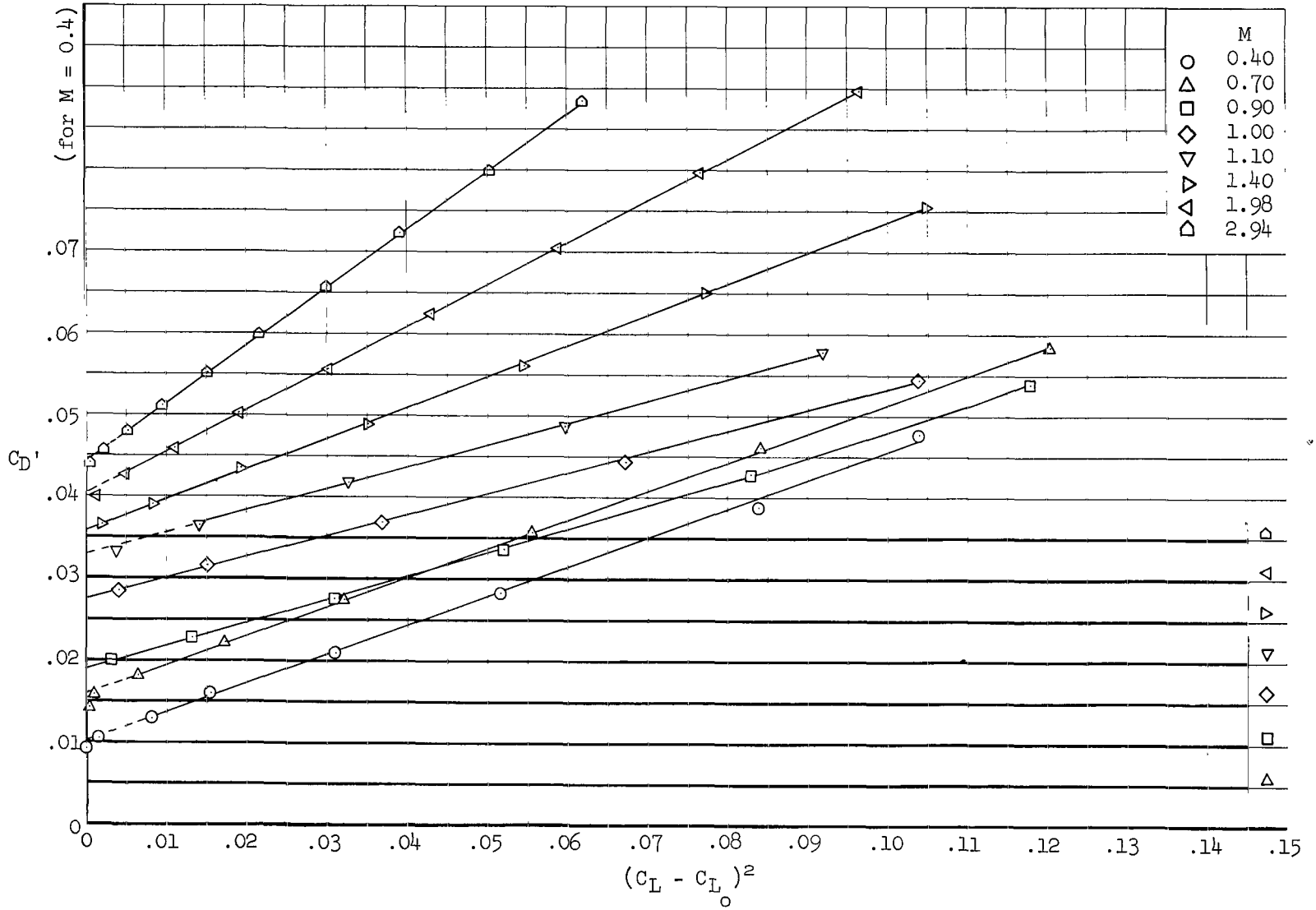
(a) C_L vs. α and C_L vs. C_m

Figure 5.- Lift, drag, and pitching-moment characteristics of model 4.



(b) C_L vs. C_D'

Figure 5.- Continued.



(c) C_D' vs. $(C_L - C_{L_0})^2$

Figure 5.- Concluded.

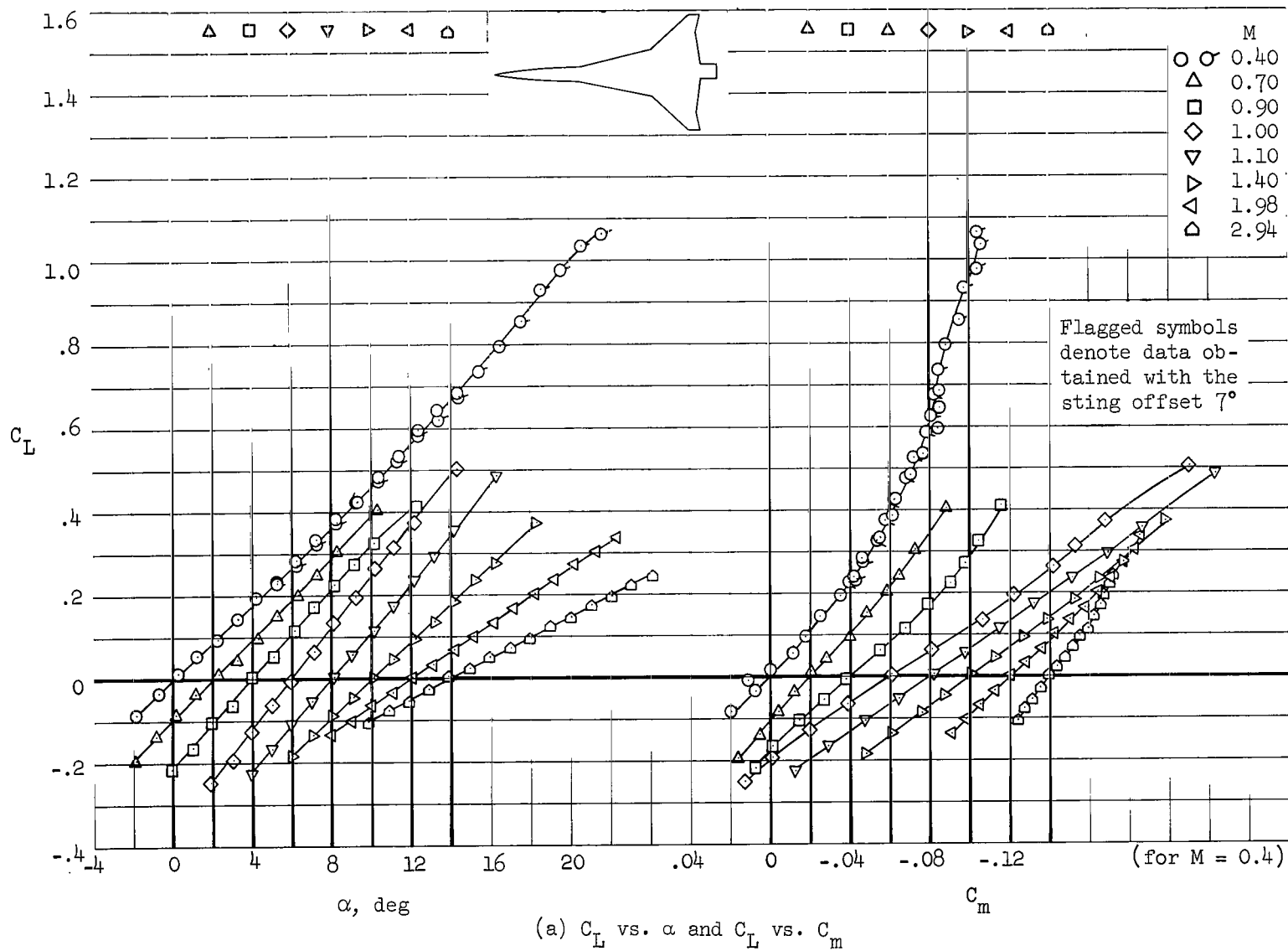
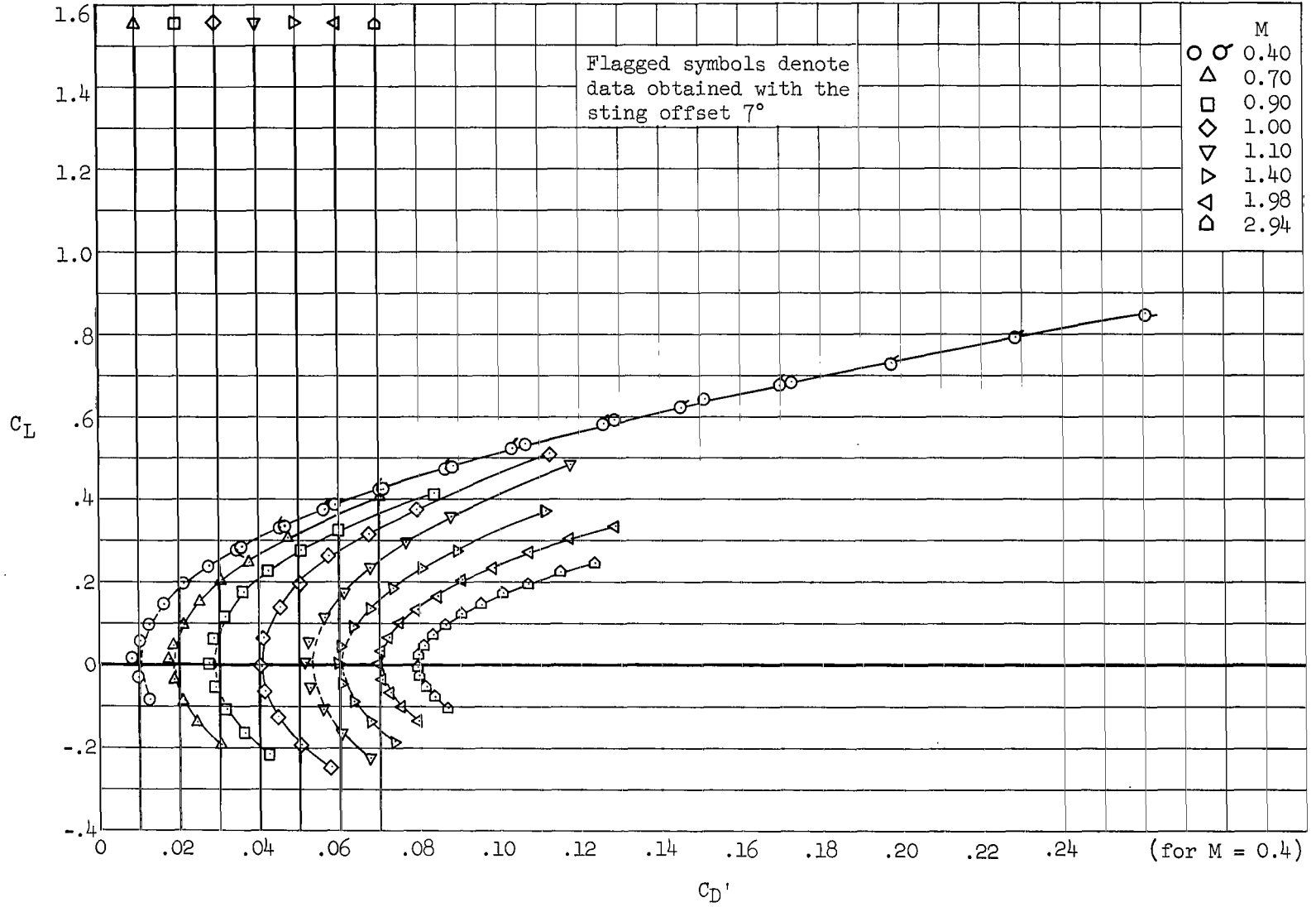
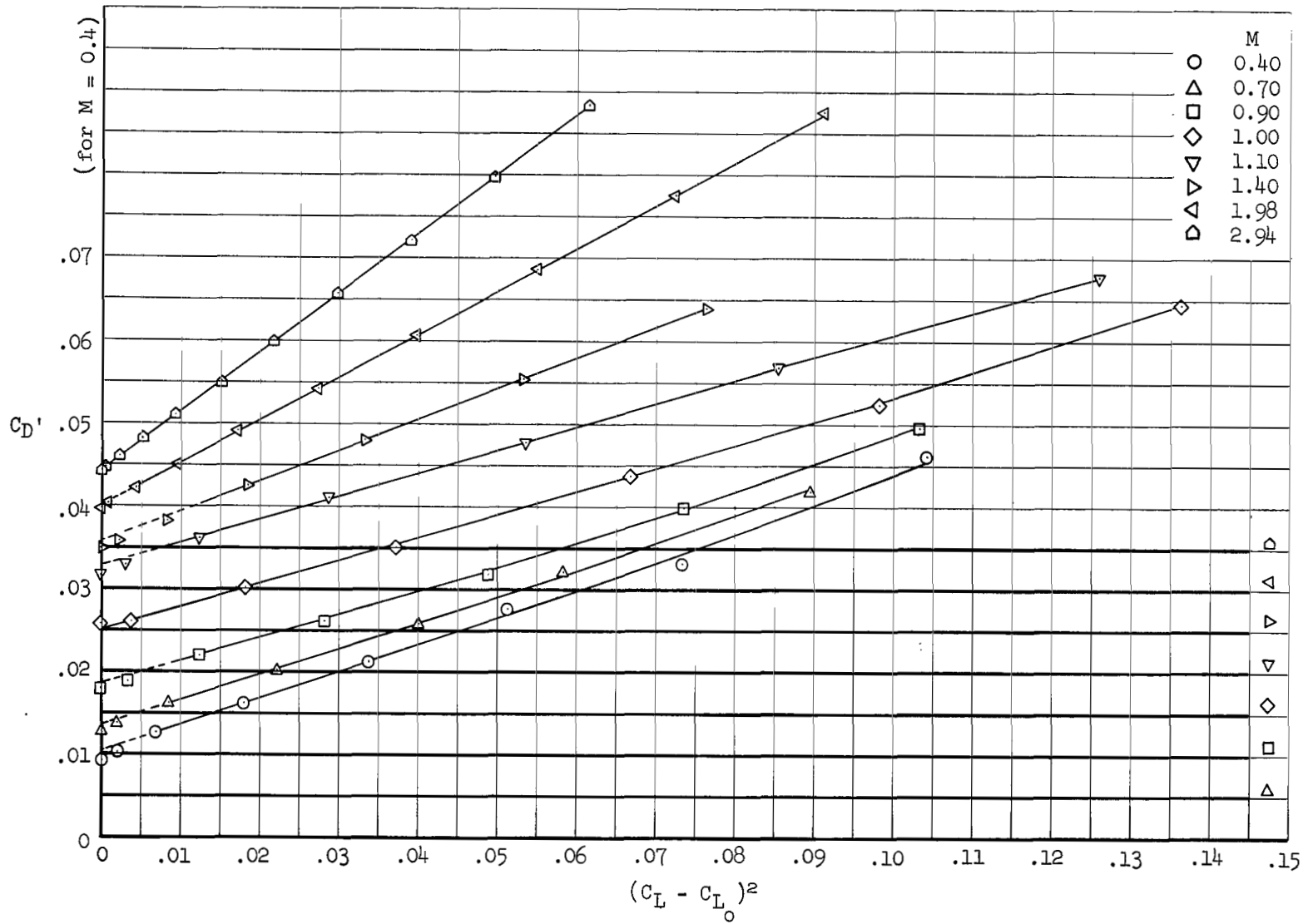


Figure 6.- Lift, drag, and pitching-moment characteristics of model 5.



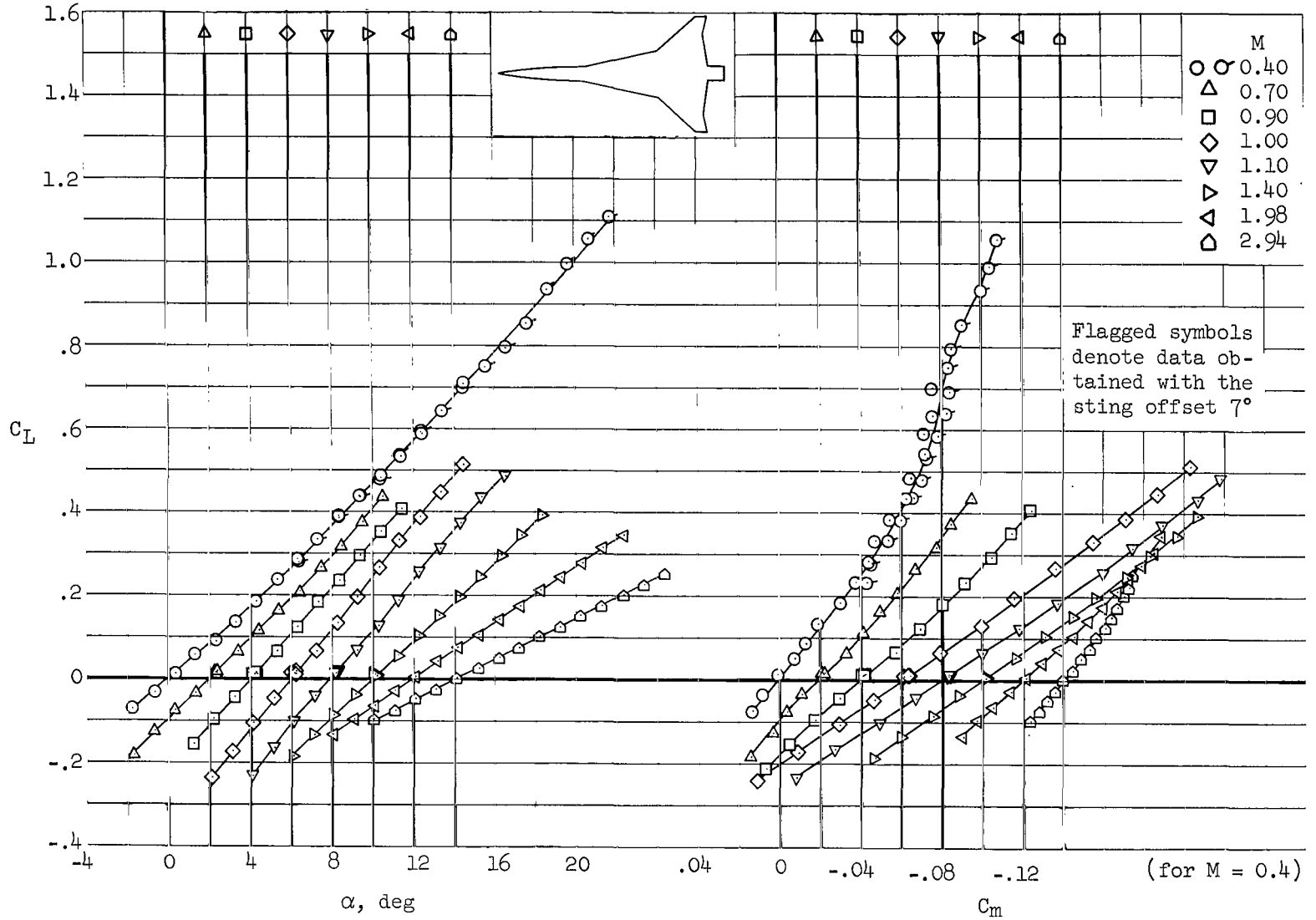
(b) C_L vs. C_D'

Figure 6.- Continued.



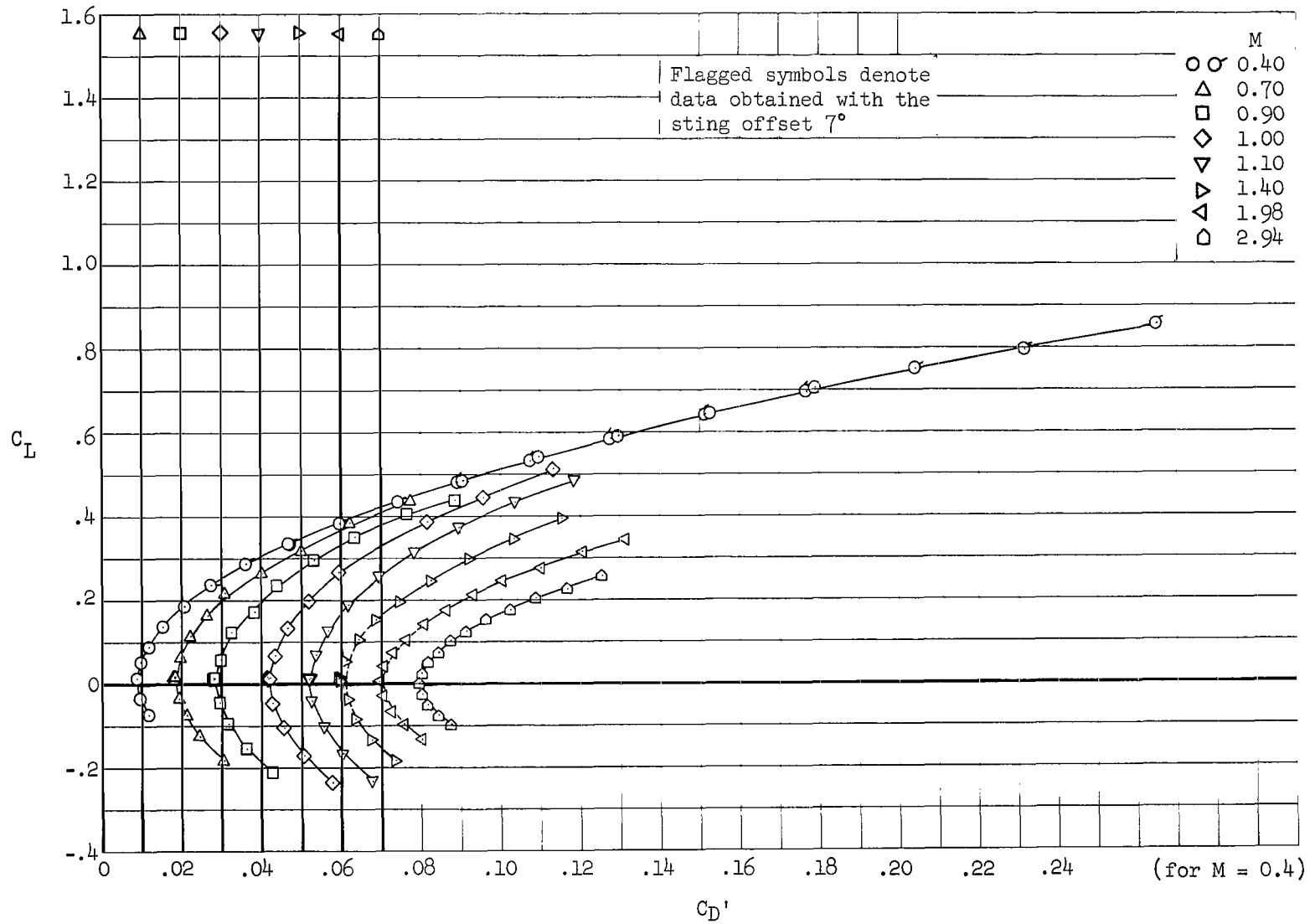
(c) C_D' vs. $(C_L - C_{L_0})^2$

Figure 6.- Concluded.



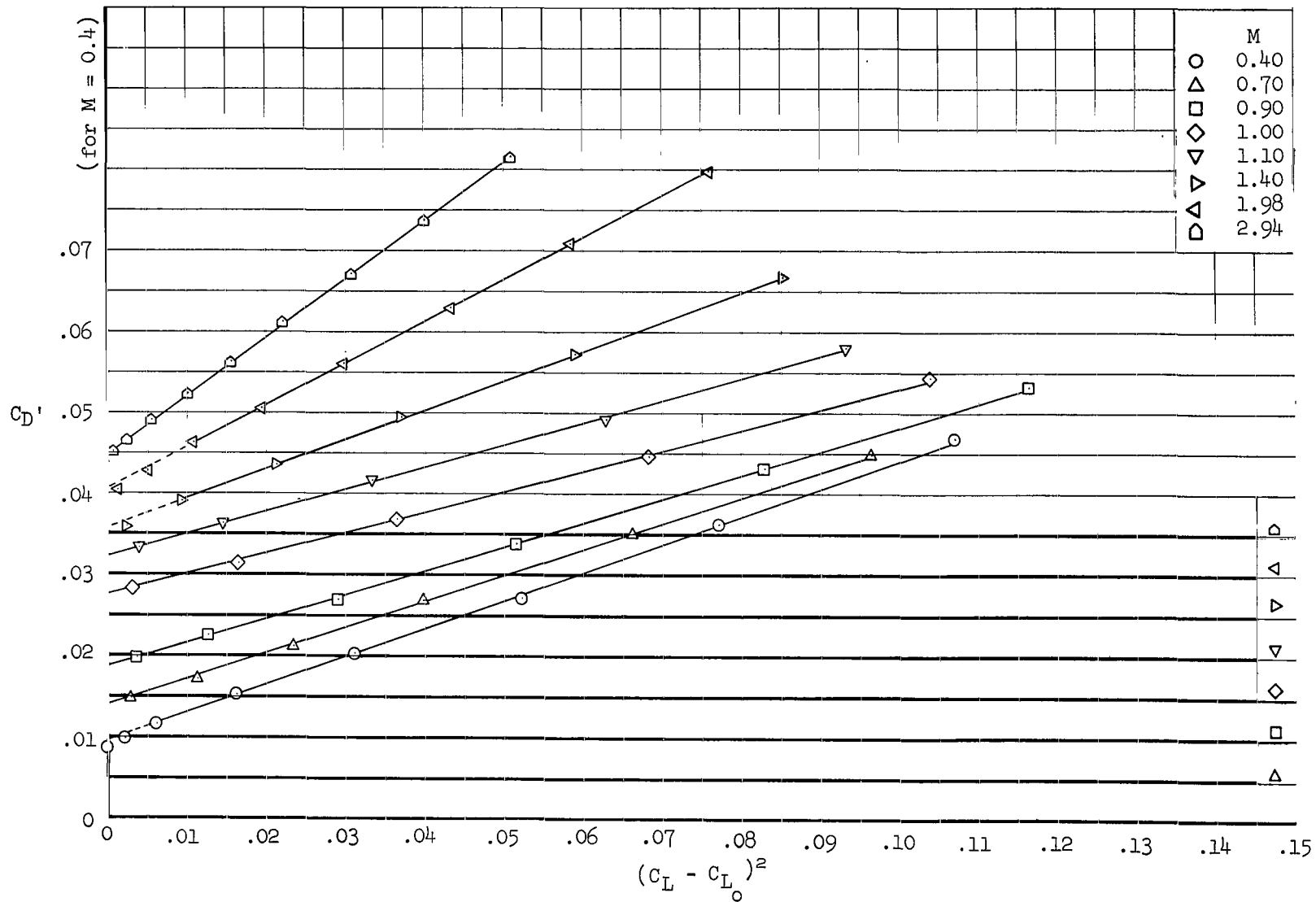
(a) C_L vs. α and C_L vs. C_m

Figure 7.- Lift, drag, and pitching-moment characteristics of model 6.



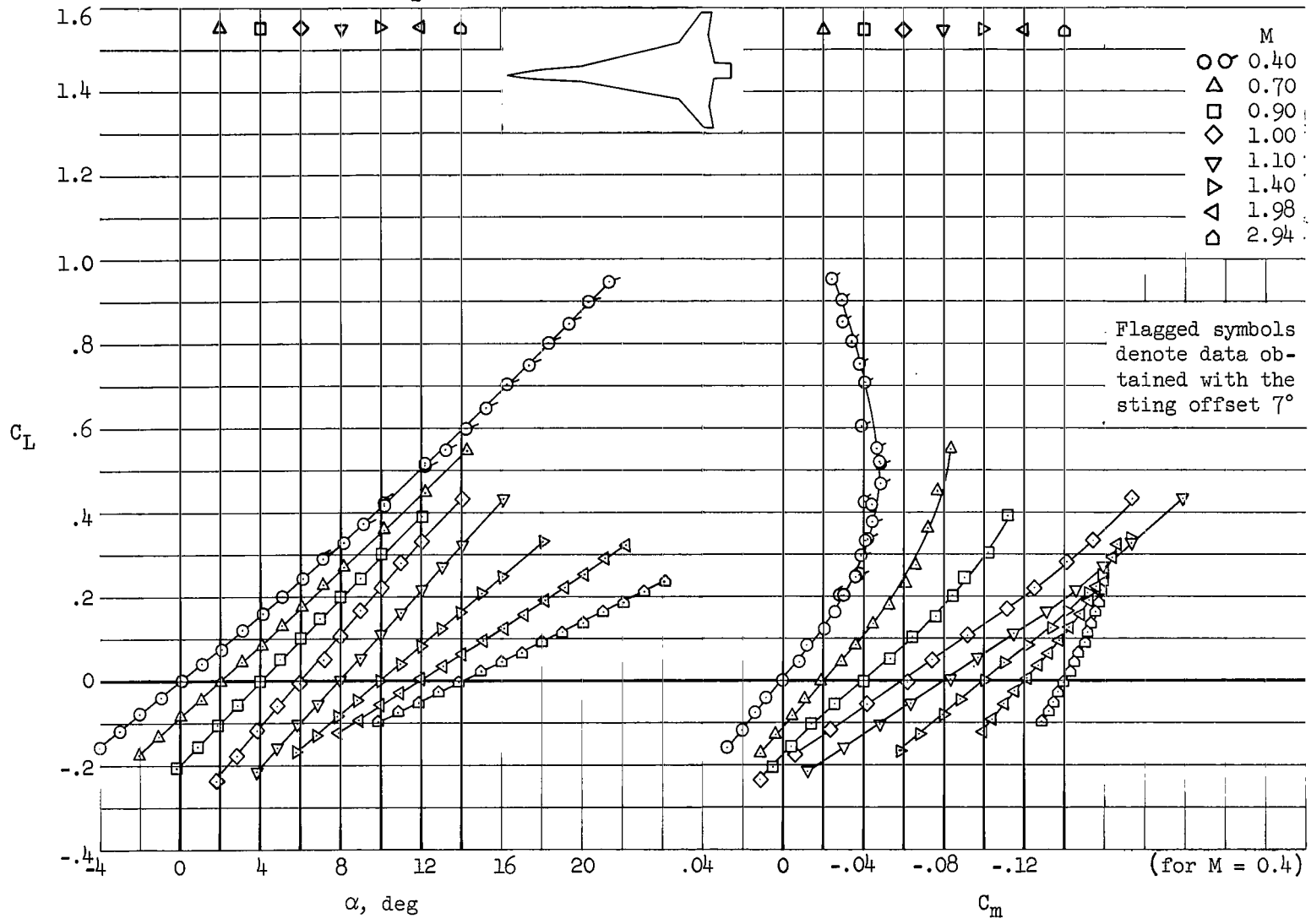
(b) C_L vs. C_D'

Figure 7.- Continued.



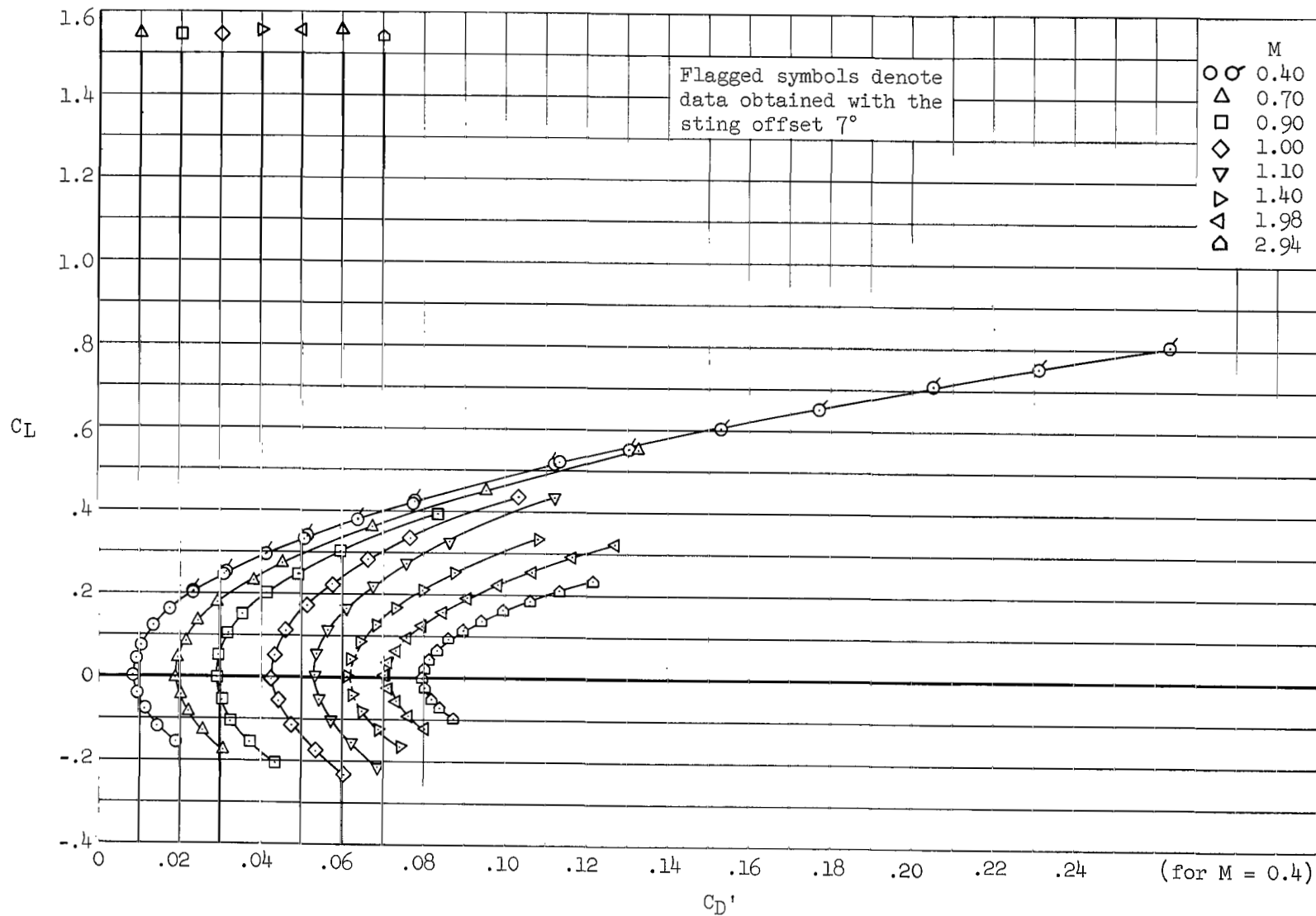
(c) C_D' vs. $(C_L - C_{L_0})^2$

Figure 7.- Concluded.



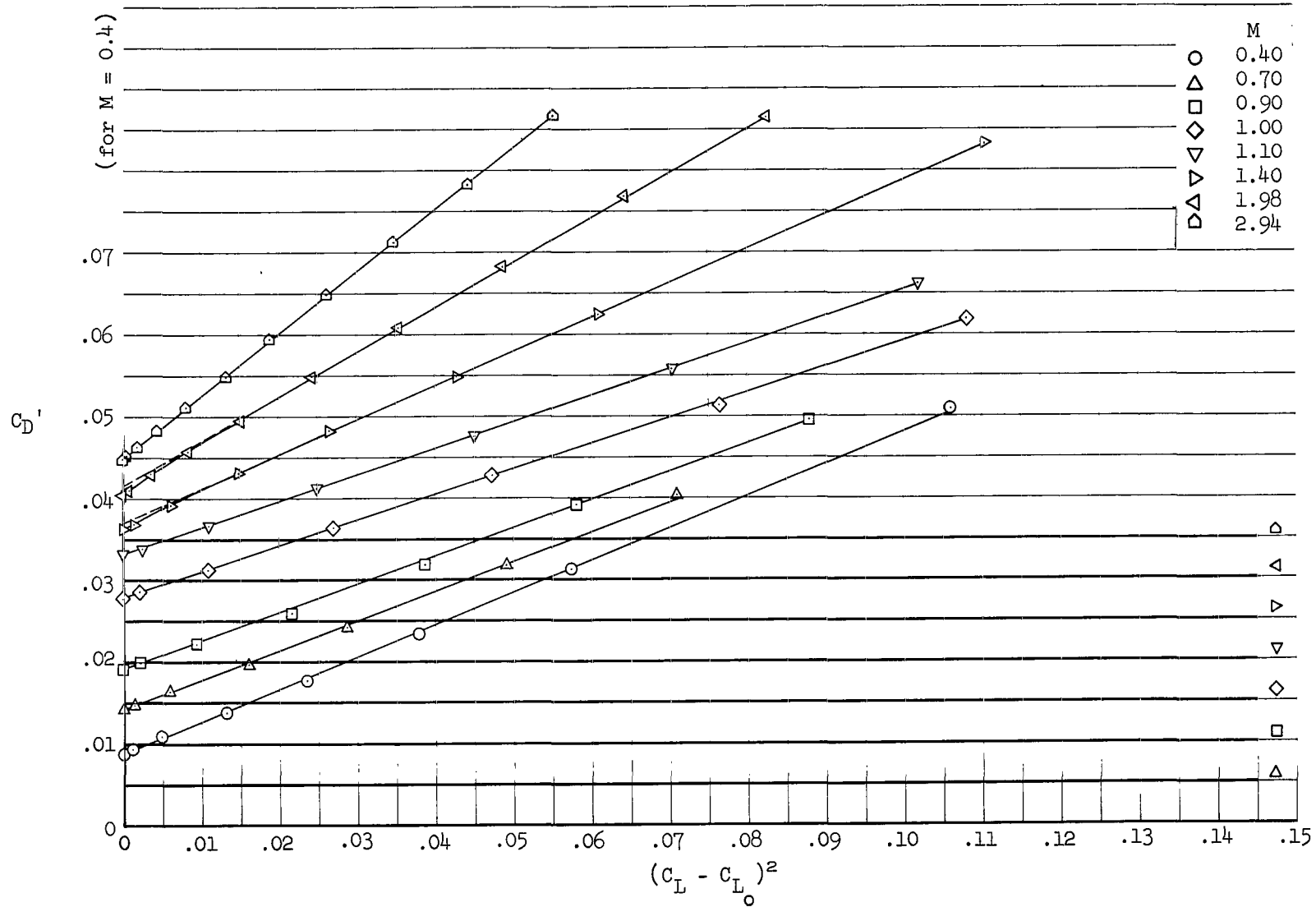
(a) C_L vs. α and C_L vs. C_m

Figure 8.- Lift, drag, and pitching-moment characteristics of model 7.



(b) C_L vs. C_D'

Figure 8.- Continued.



(c) C_D' vs. $(C_L - C_{L_0})^2$

Figure 8.- Concluded.

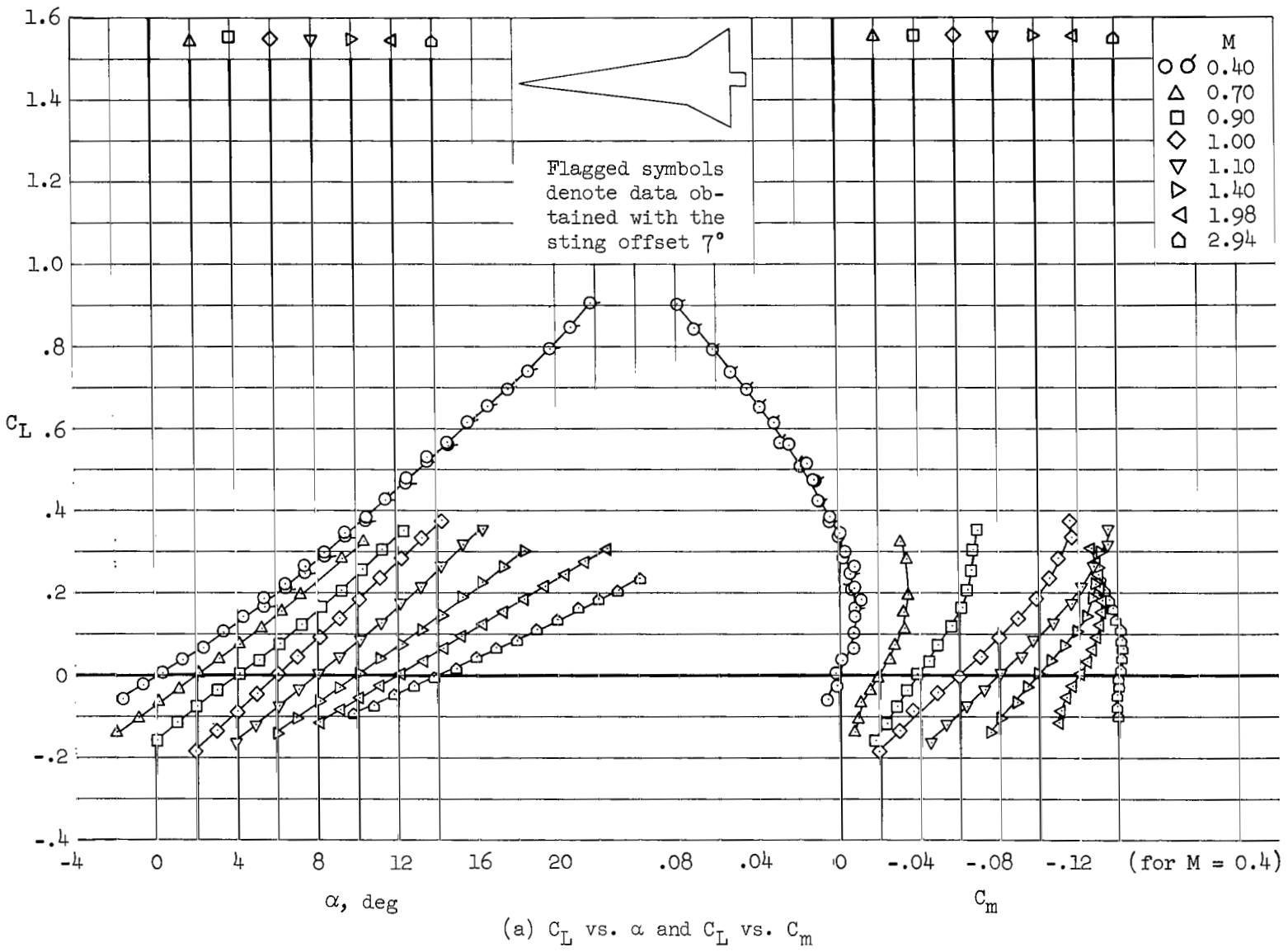
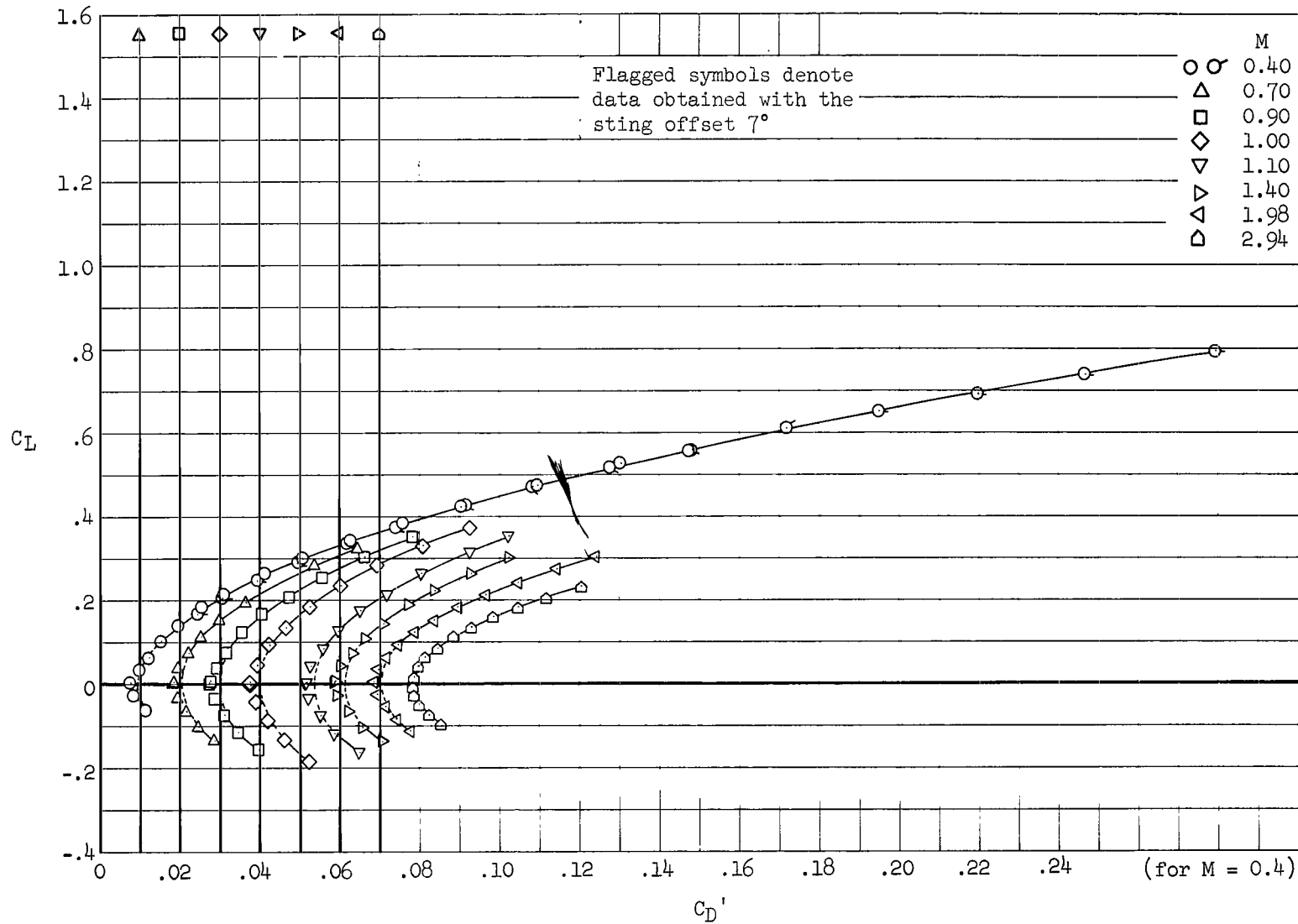
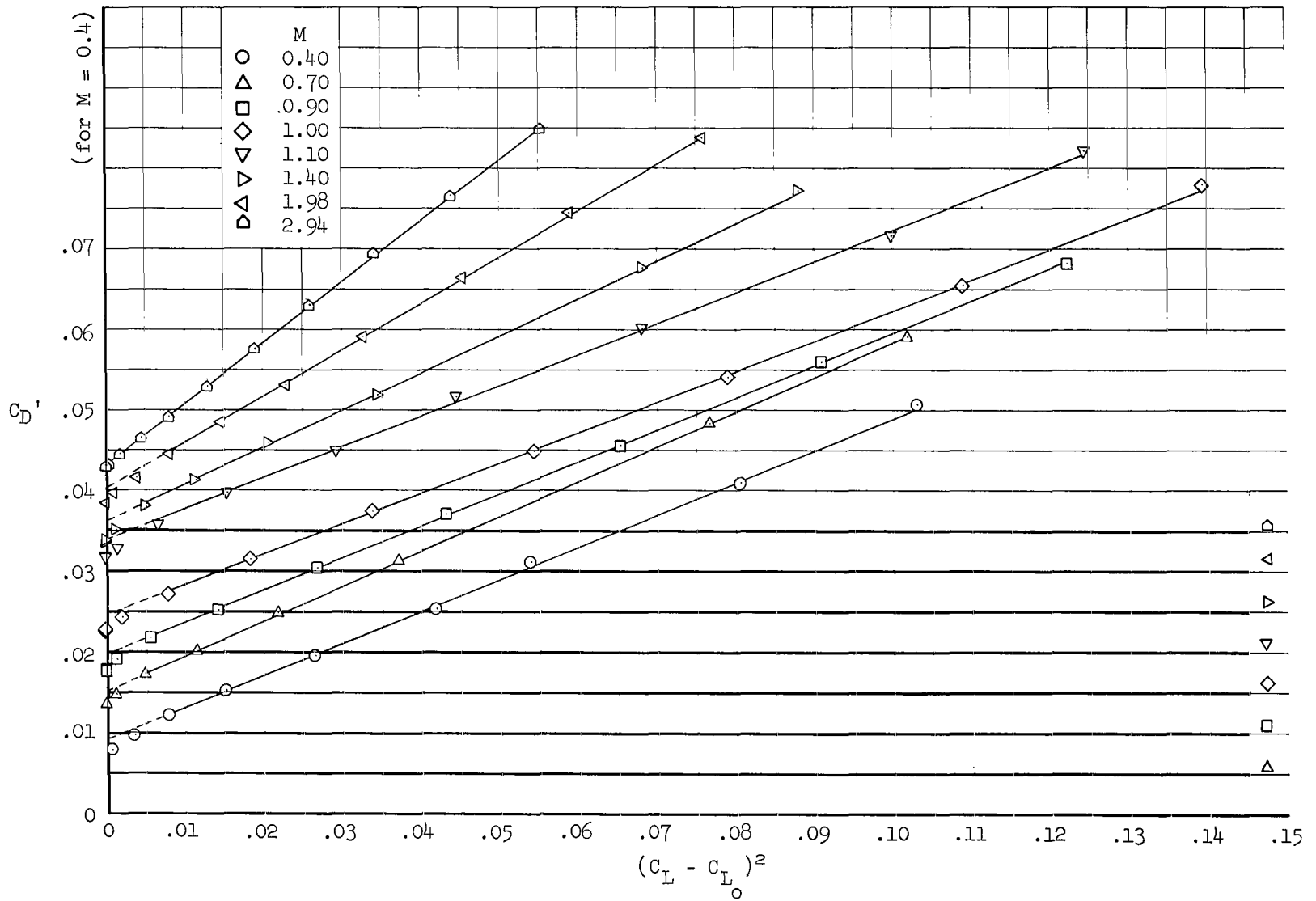


Figure 9.- Lift, drag, and pitching-moment characteristics of model 8.



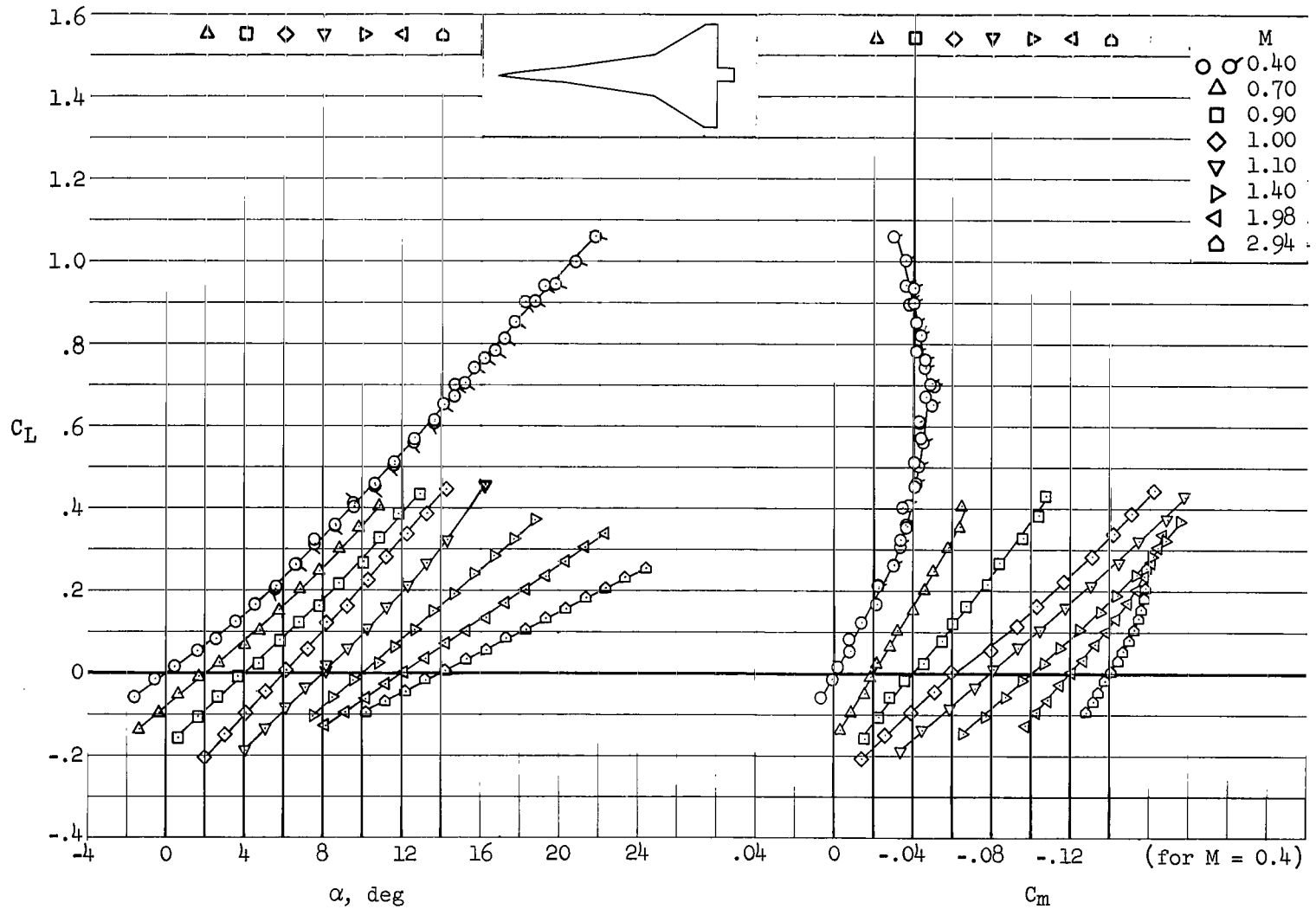
(b) C_L vs. C_D'

Figure 9.- Continued.



(c) C_D' vs. $(C_L - C_{L_0})^2$

Figure 9.- Concluded.



(a) C_L vs. α and C_L vs. C_m

Figure 10.- Lift, drag, and pitching-moment characteristics of model 9.

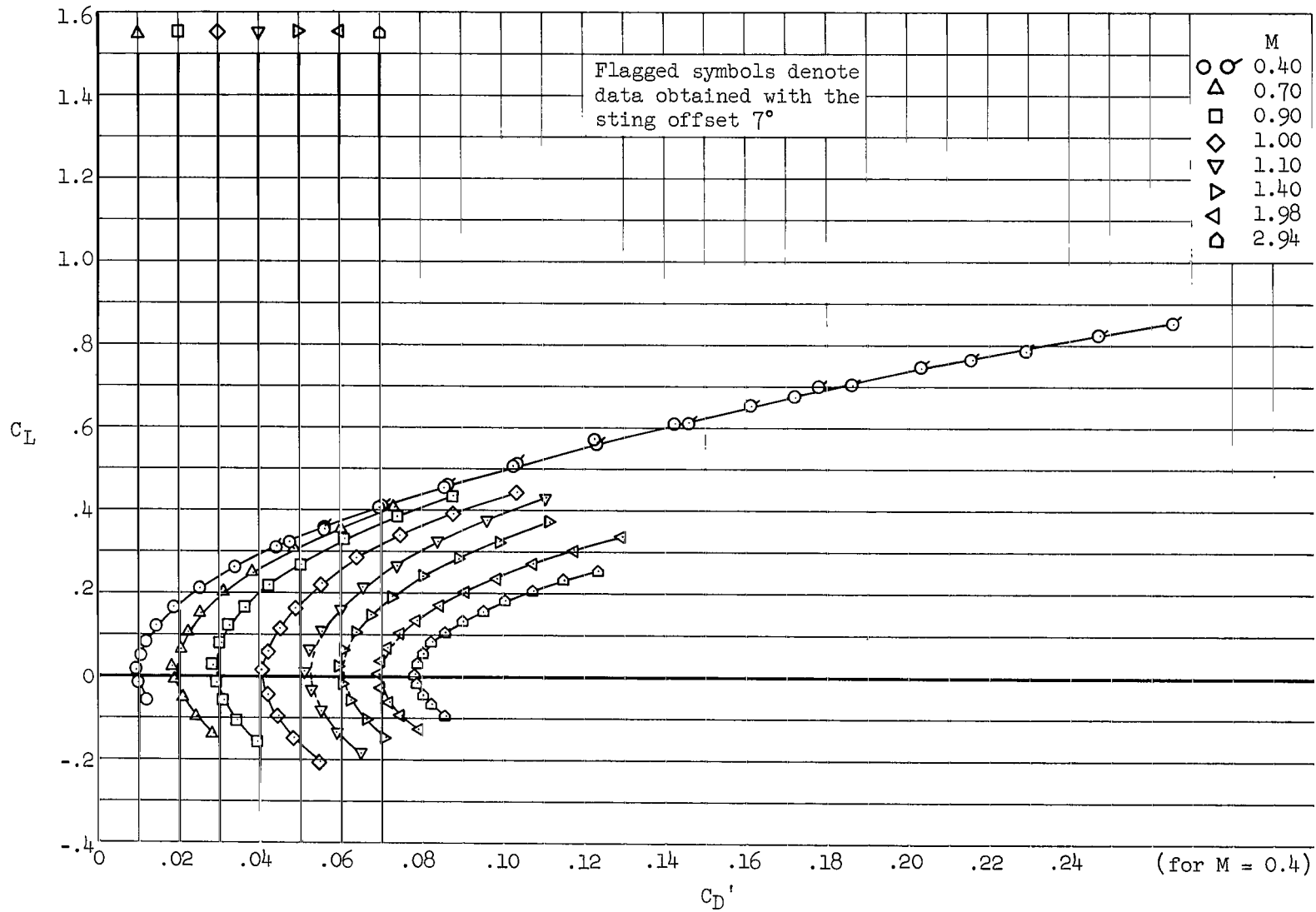
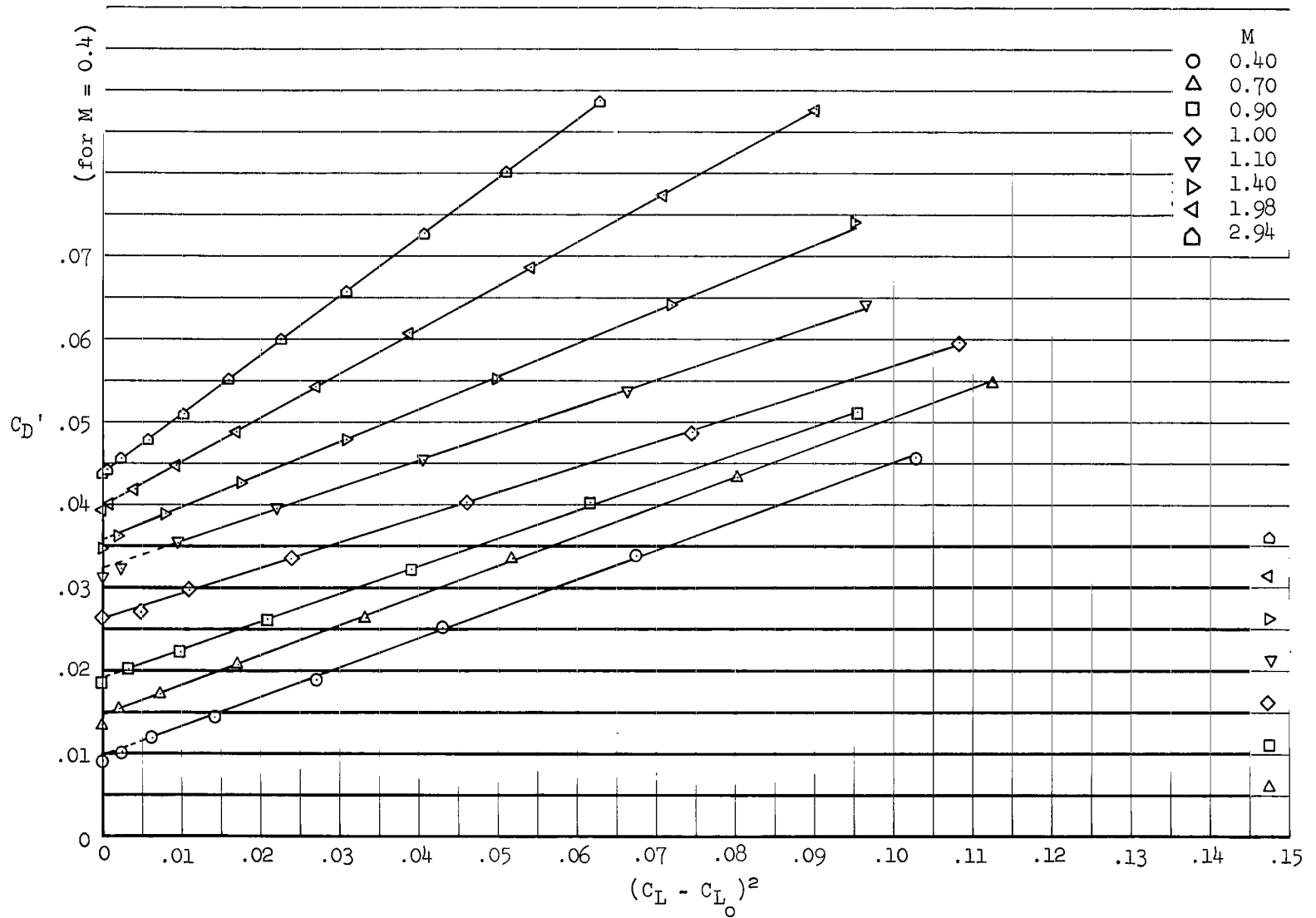
(b) C_L vs. C_D'

Figure 10.- Continued.



(c) C_D' vs. $(C_L - C_{L_0})^2$

Figure 10.- Concluded.

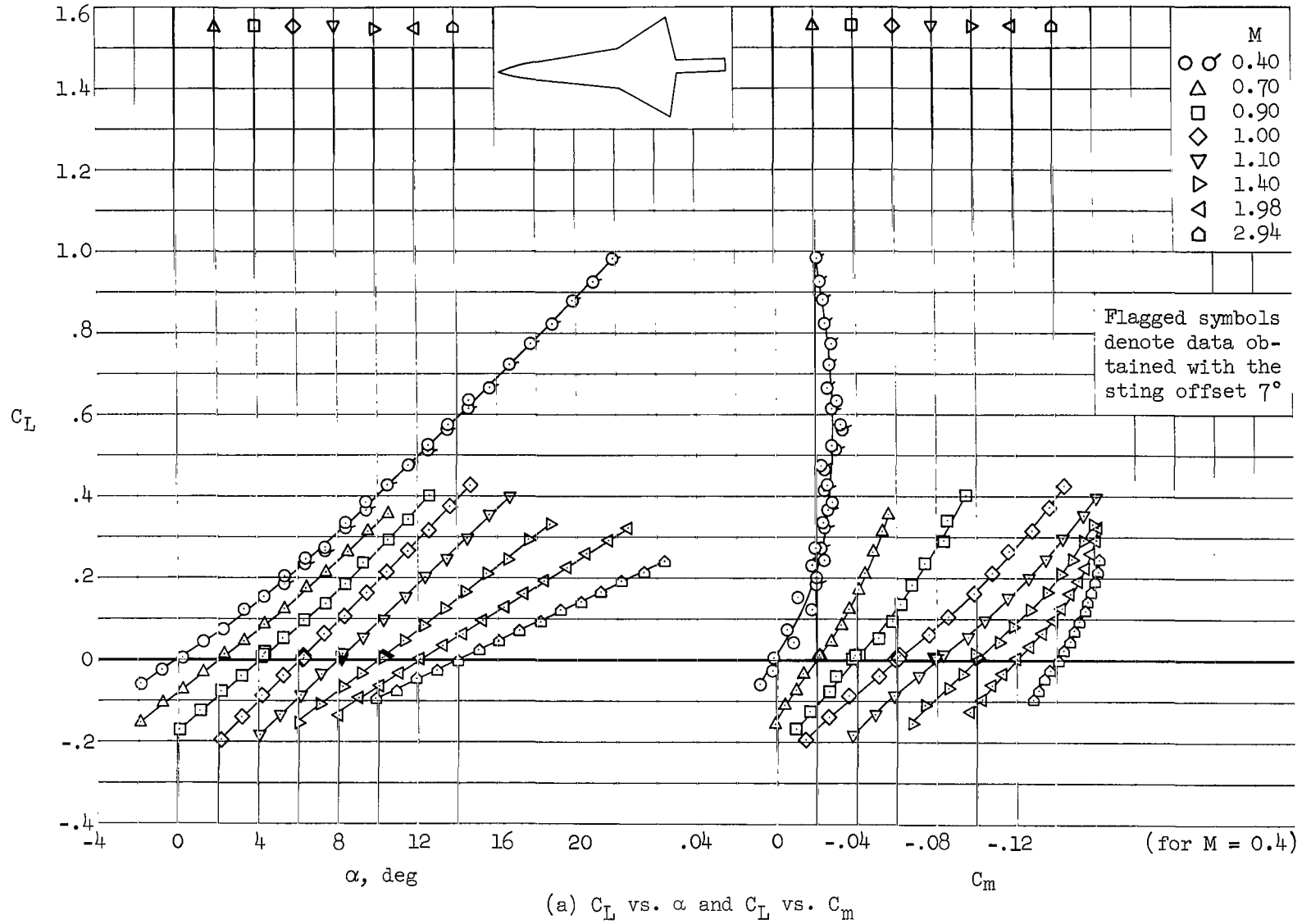
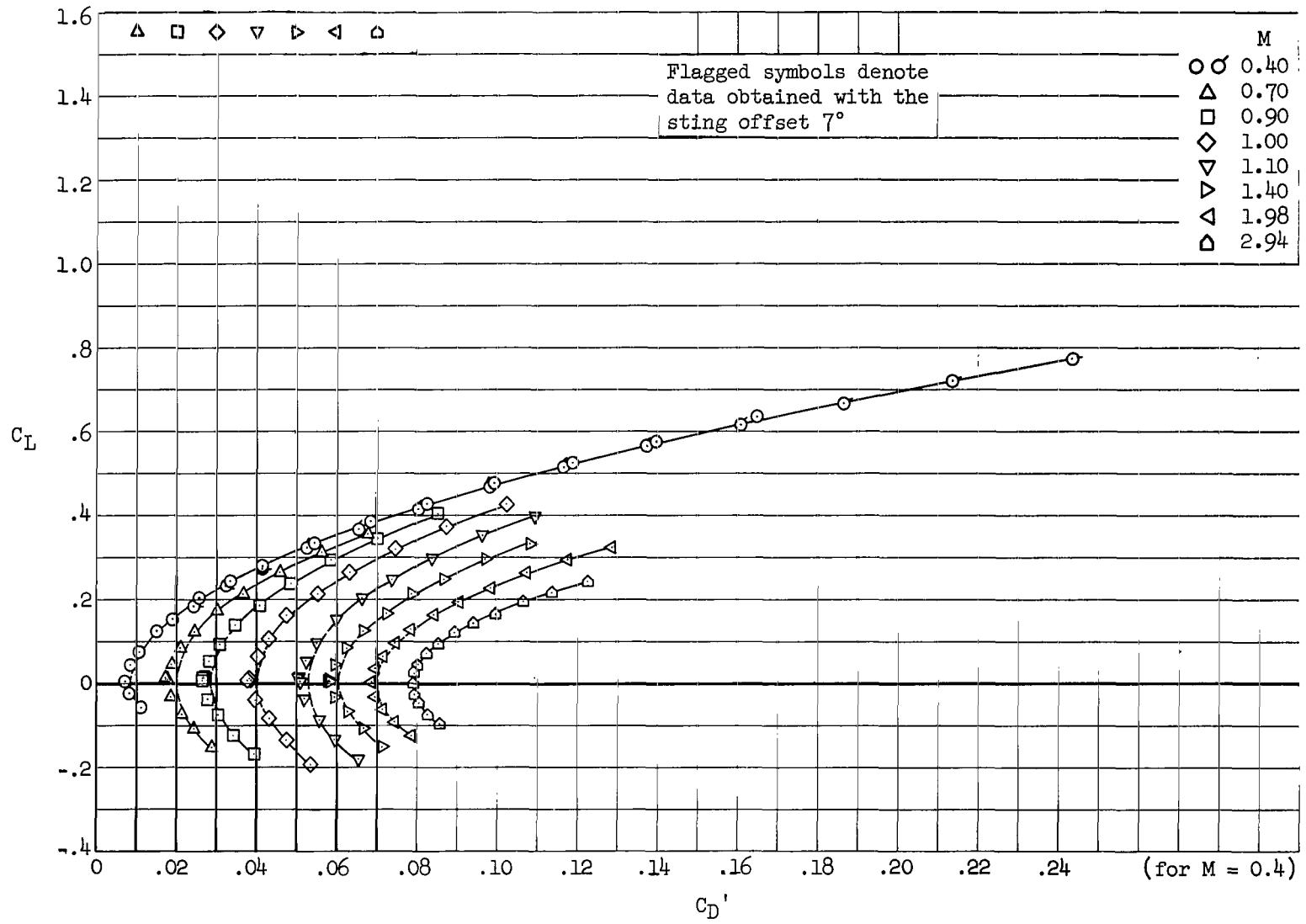
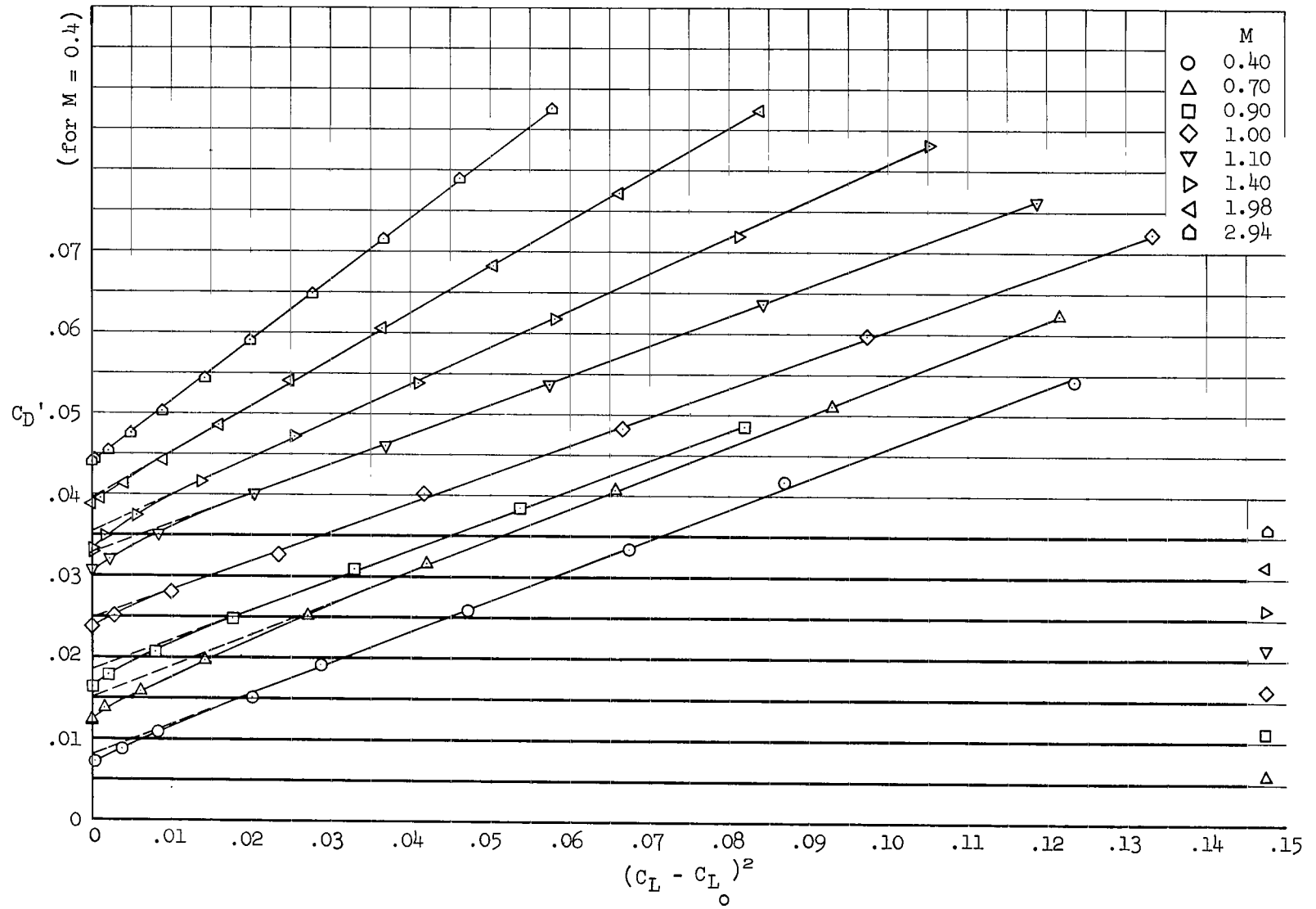


Figure 11.- Lift, drag, and pitching-moment characteristics of model 10.



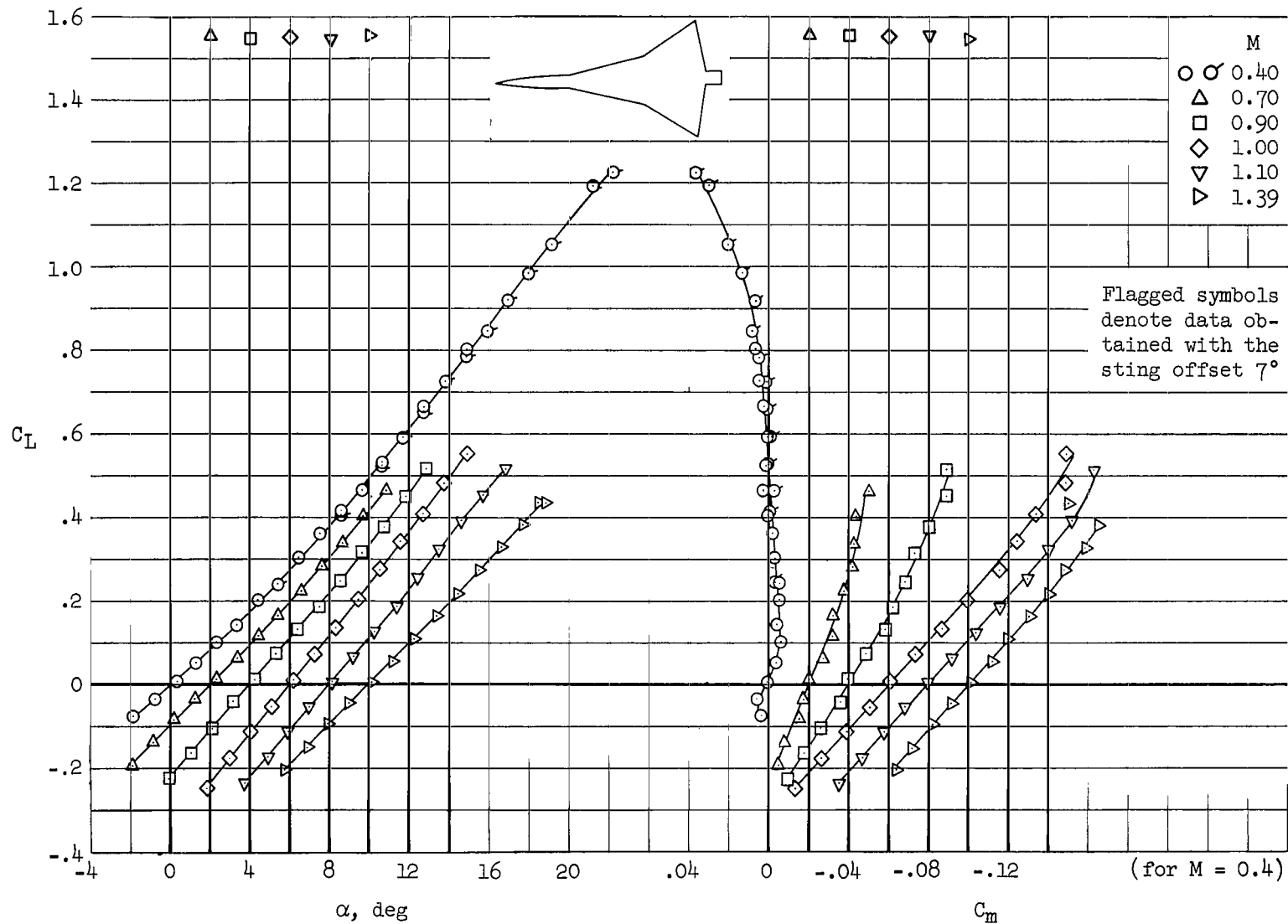
(b) C_L vs. C_D'

Figure 11.- Continued.



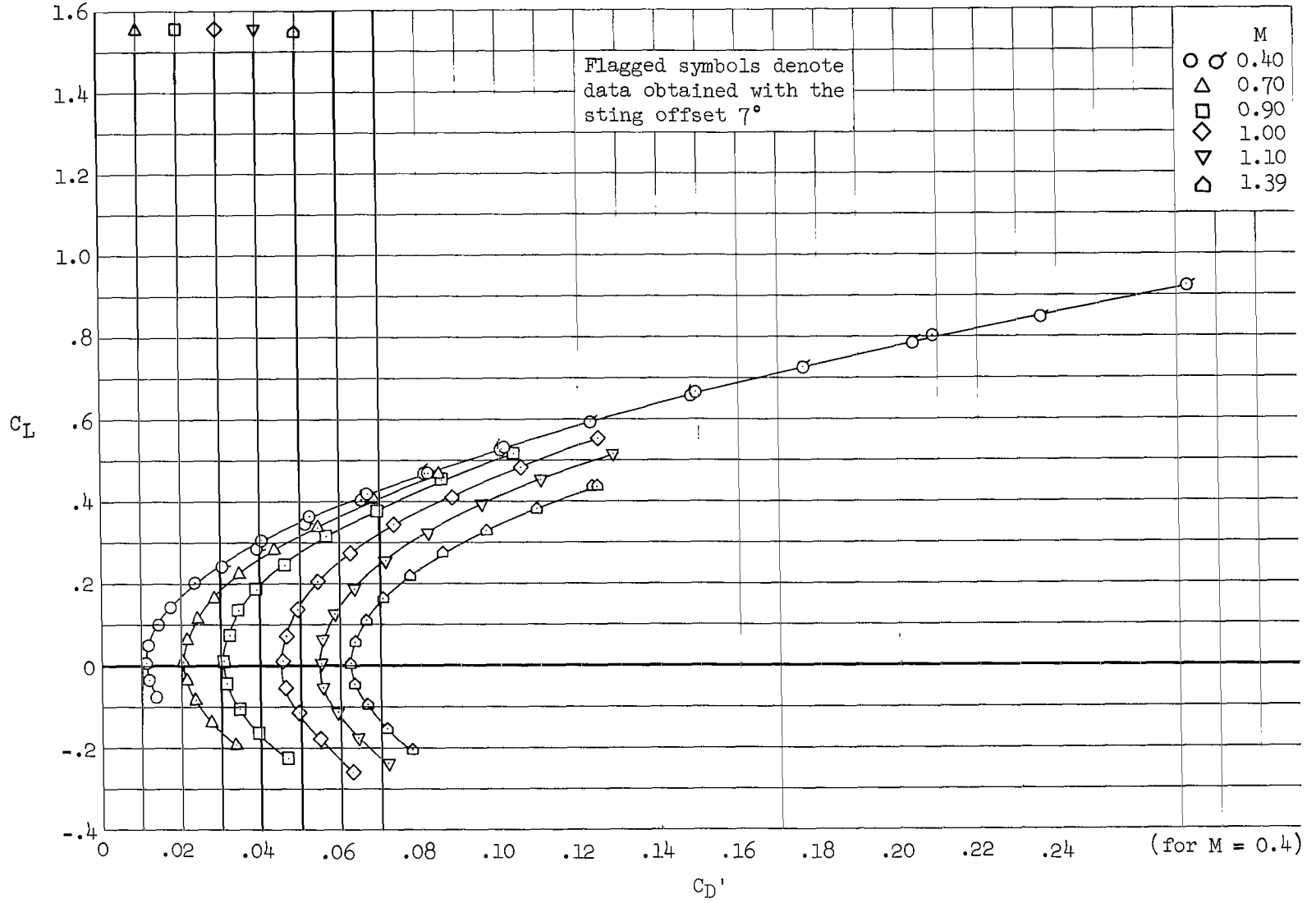
(c) C_D' vs. $(C_L - C_{L_0})^2$

Figure 11.- Concluded.



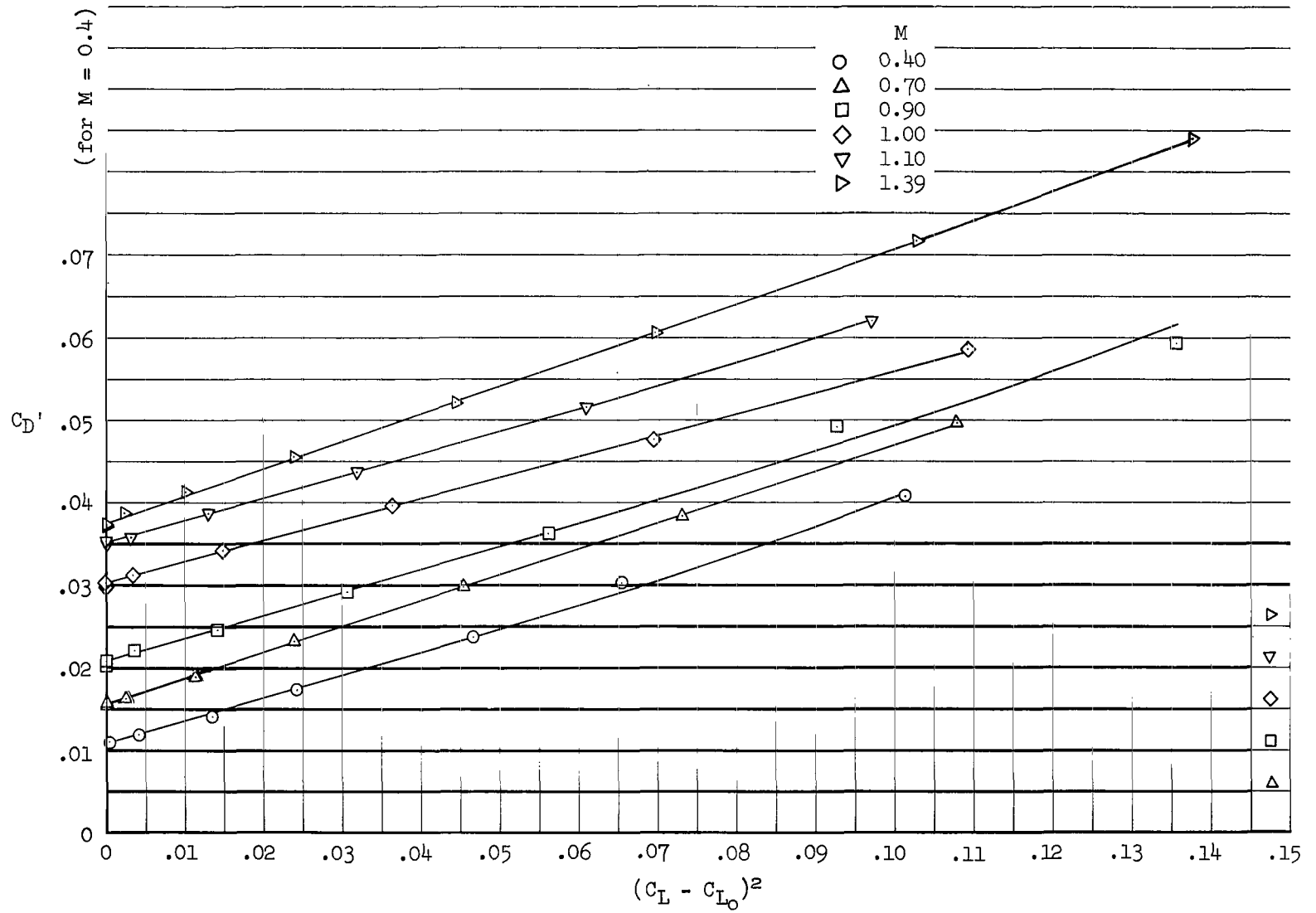
(a) C_L vs. α and C_L vs. C_m

Figure 12.- Lift, drag, and pitching-moment characteristics of model 11.



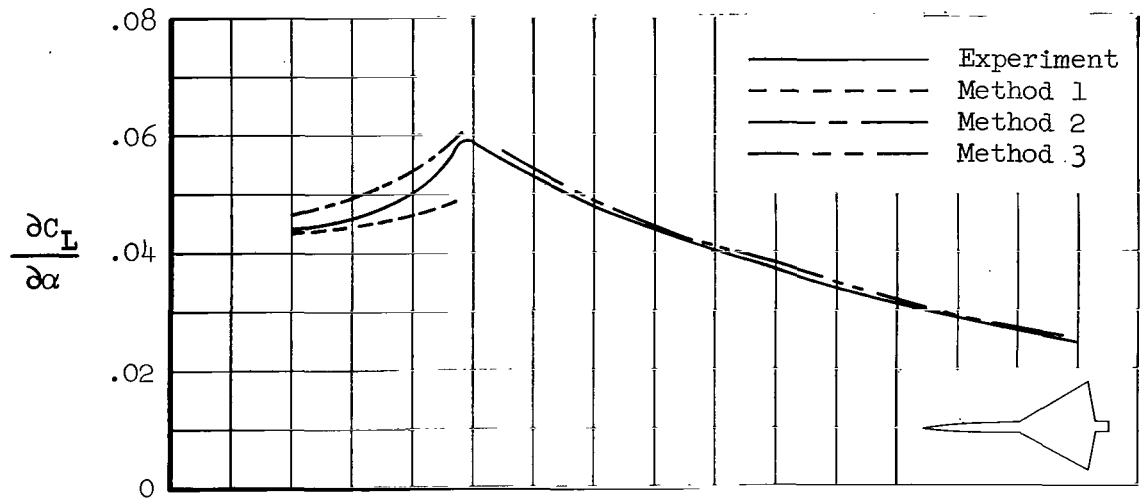
(b) C_L vs. C_D'

Figure 12.- Continued.

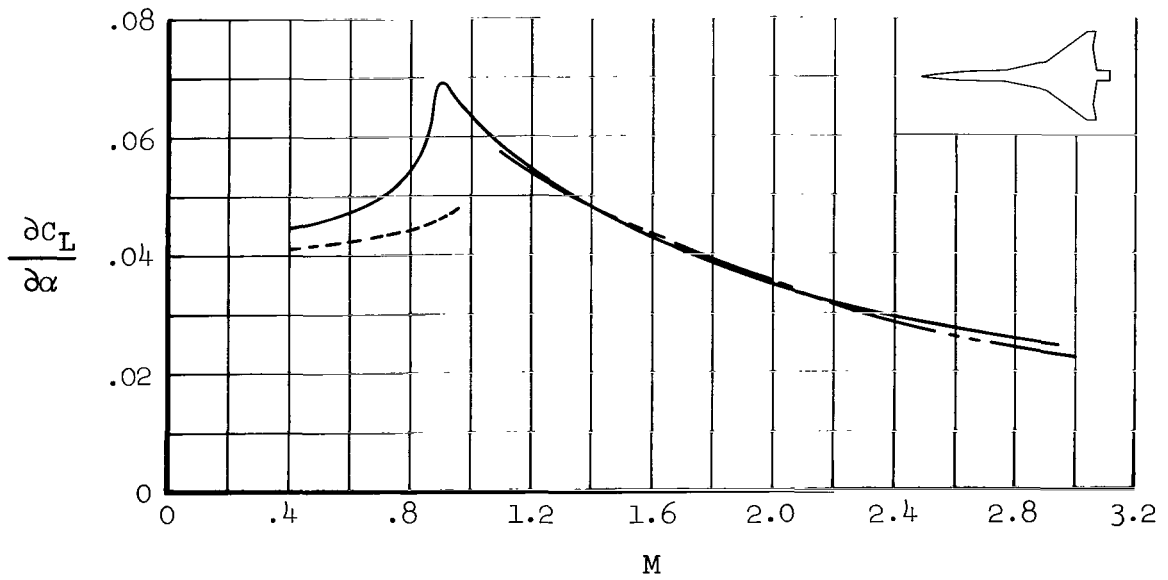


(c) C_D' vs. $(C_L - C_{L0})^2$

Figure 12.- Concluded.

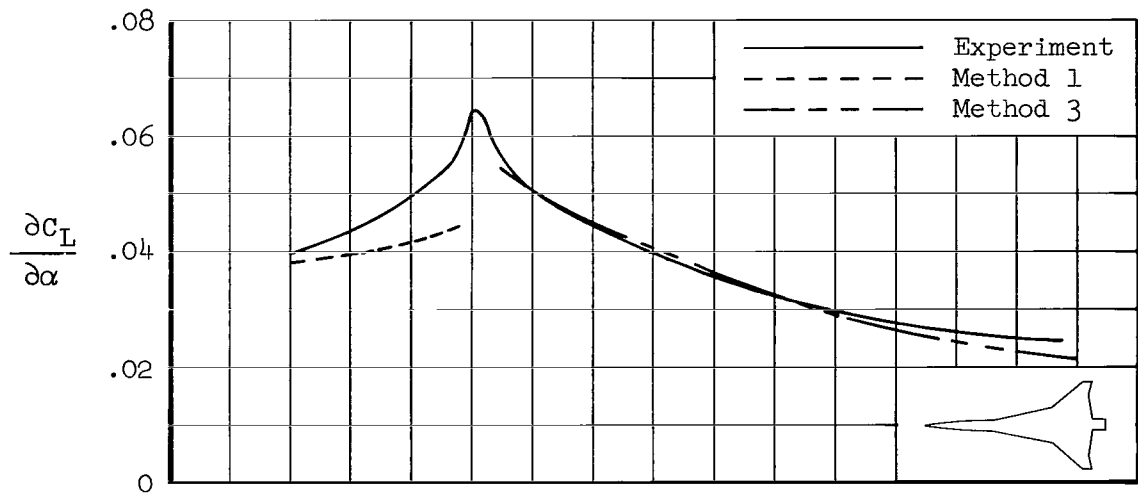


(a) Model 1

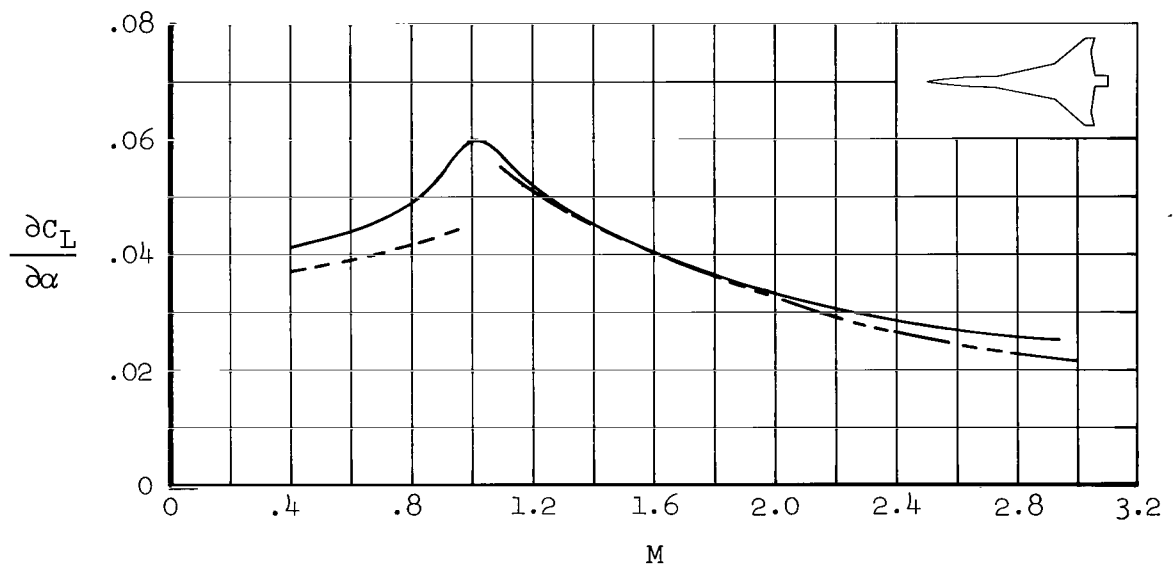


(b) Model 2

Figure 13.- Lift-curve slope as a function of Mach number.

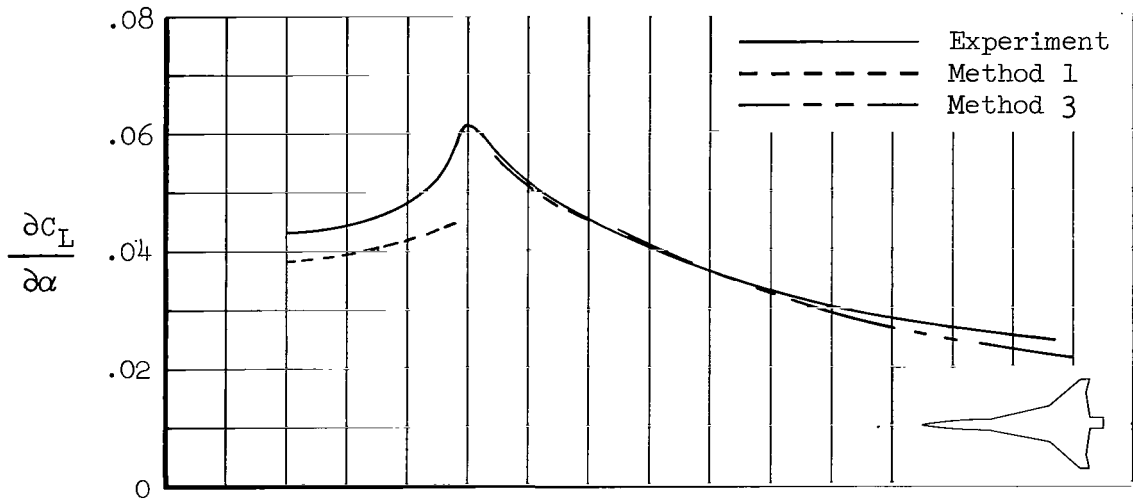


(c) Model 3

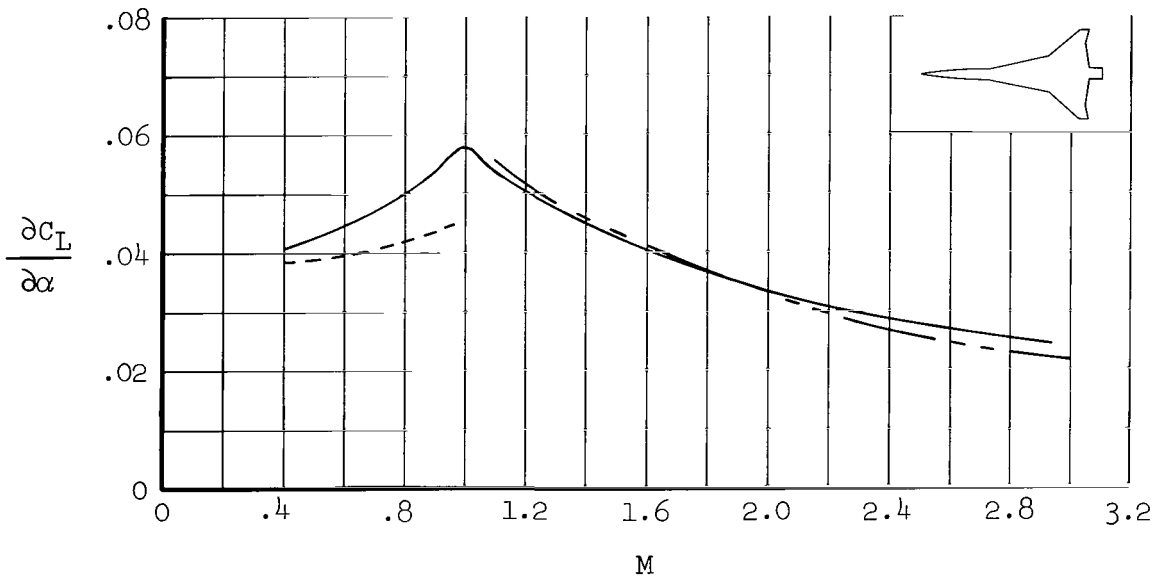


(d) Model 4

Figure 13.- Continued.

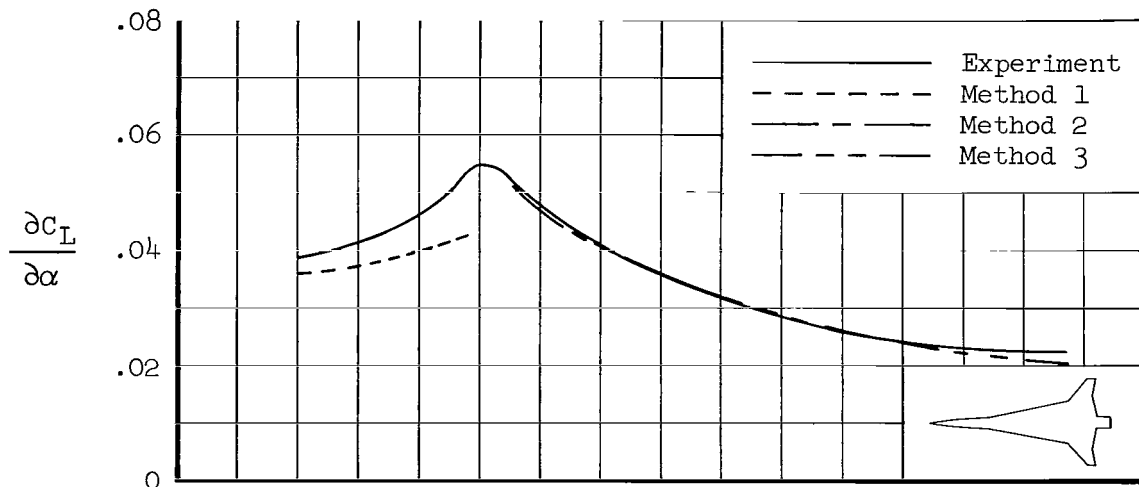


(e) Model 5

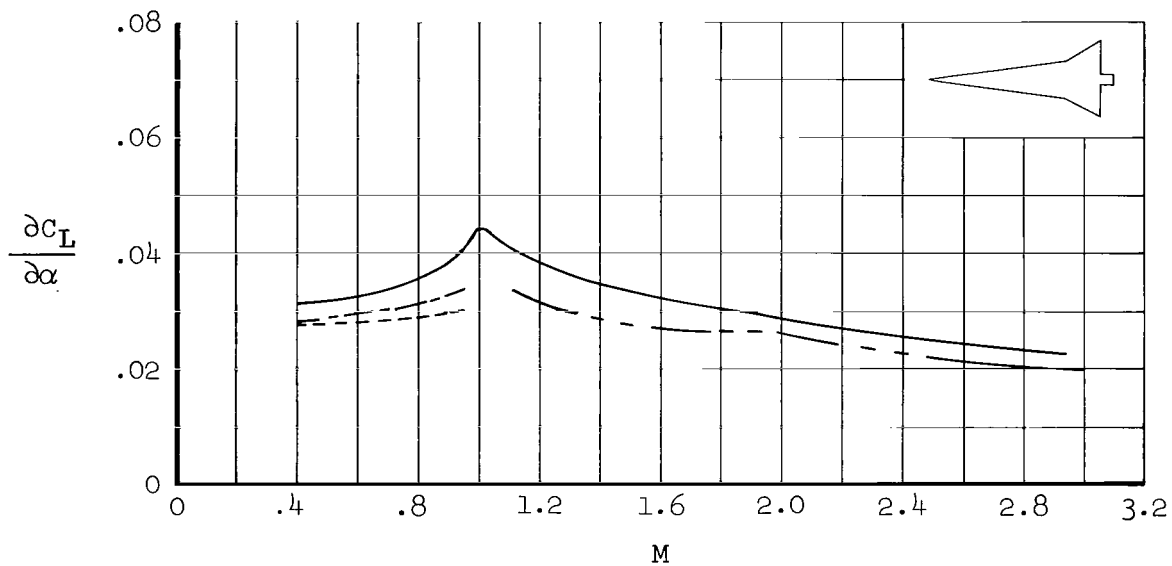


(f) Model 6

Figure 13.- Continued.

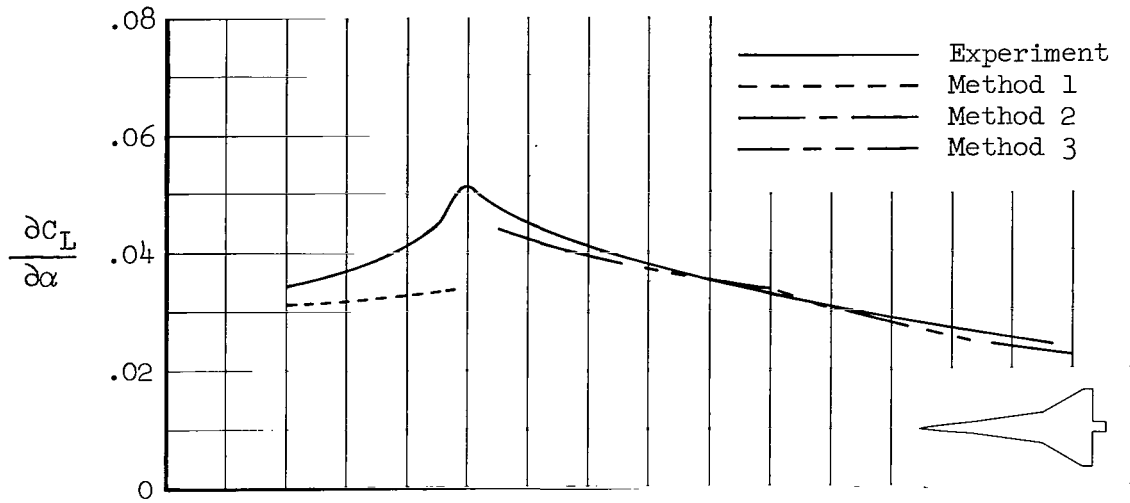


(g) Model 7

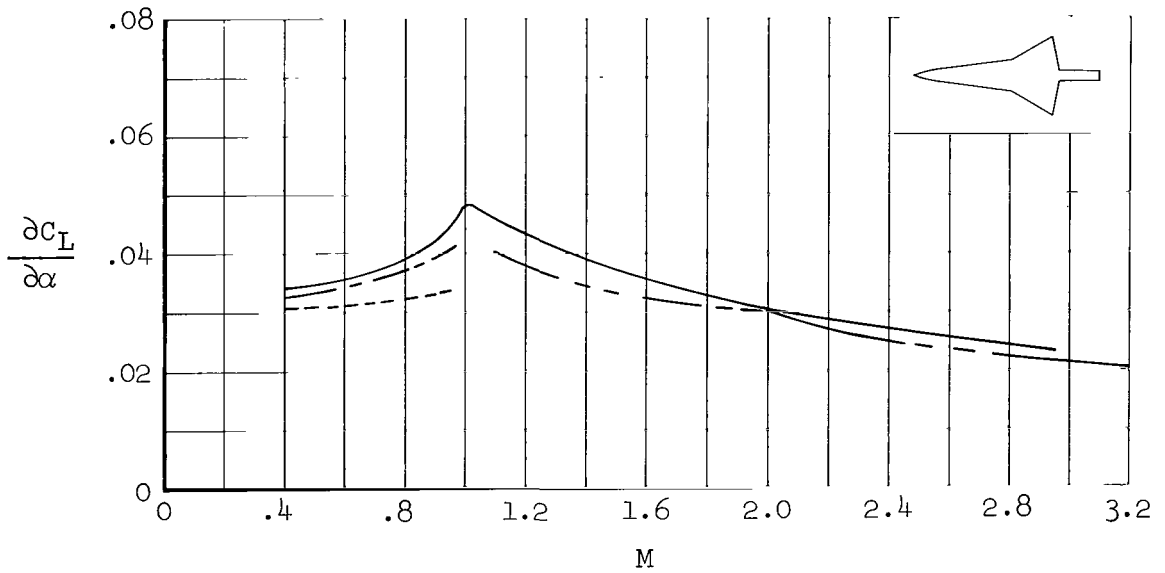


(h) Model 8

Figure 13.- Continued.

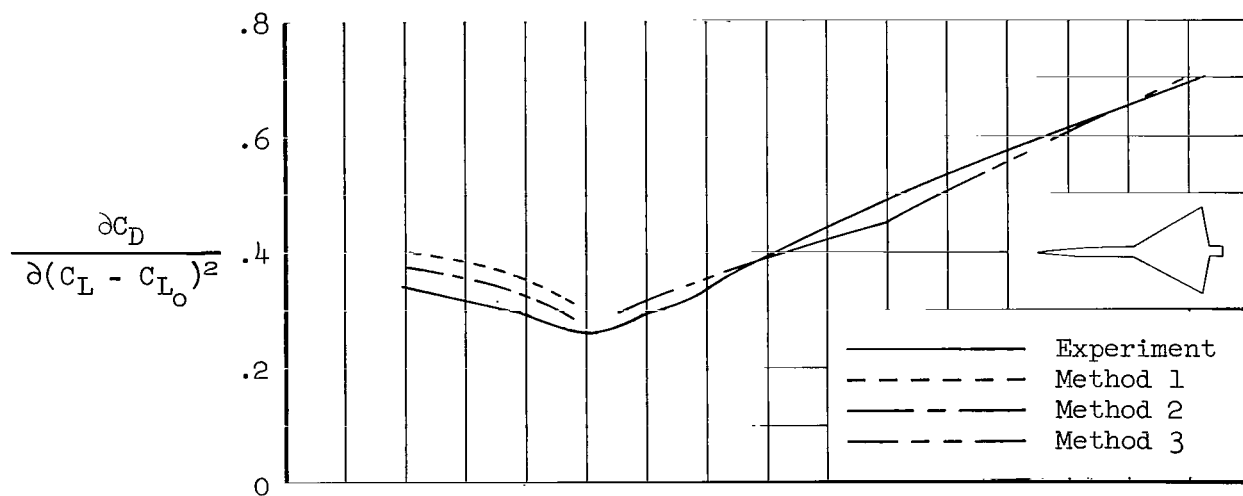


(i) Model 9

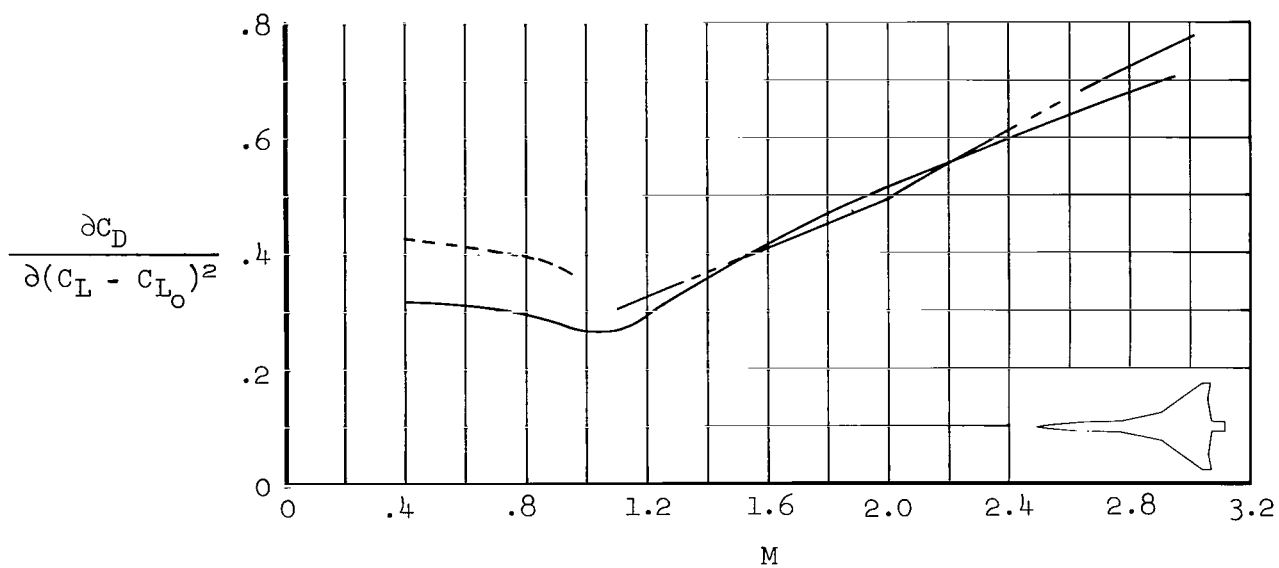


(j) Model 10

Figure 13.- Concluded.

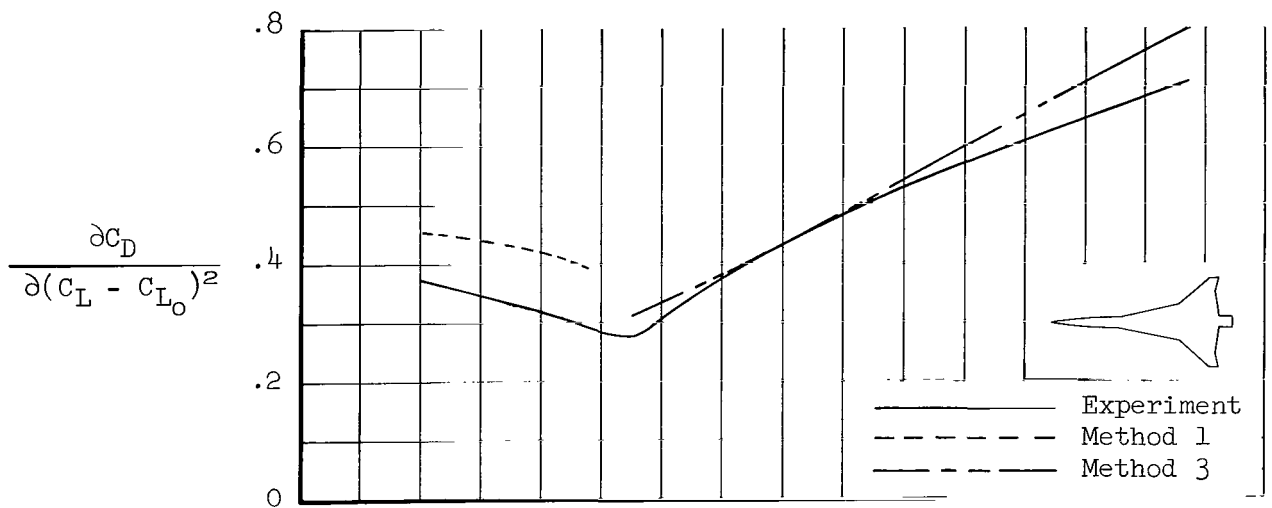


(a) Model 1

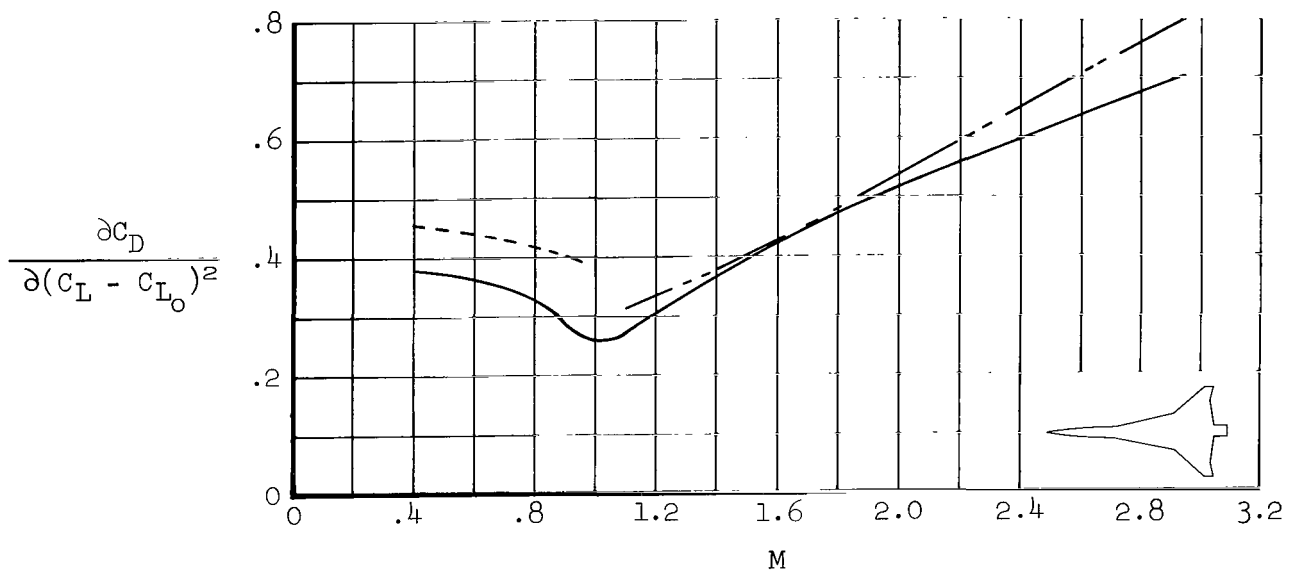


(b) Model 2

Figure 14.- Drag-due-to-lift factor as a function of Mach number.

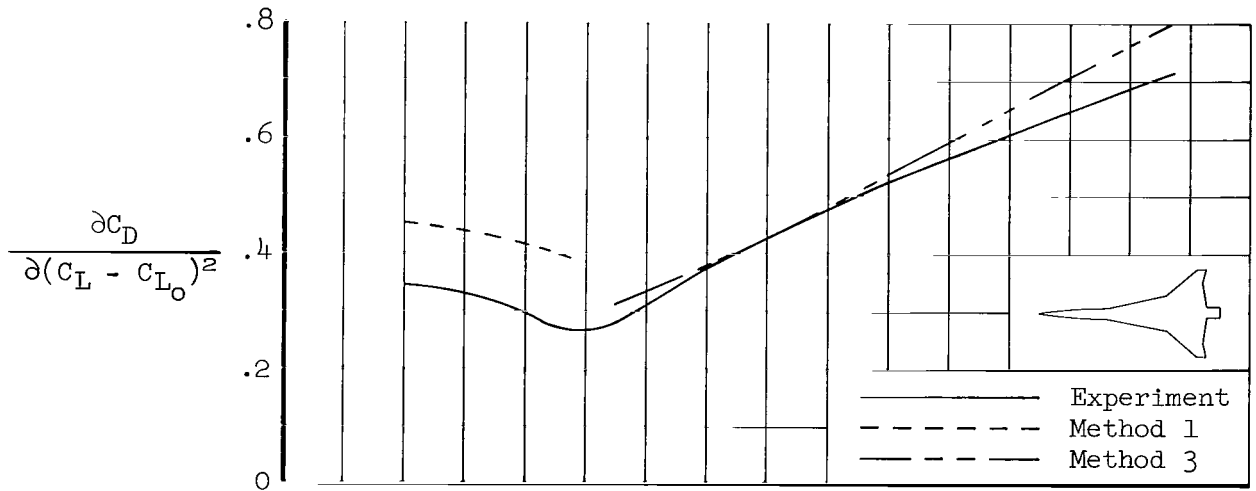


(c) Model 3

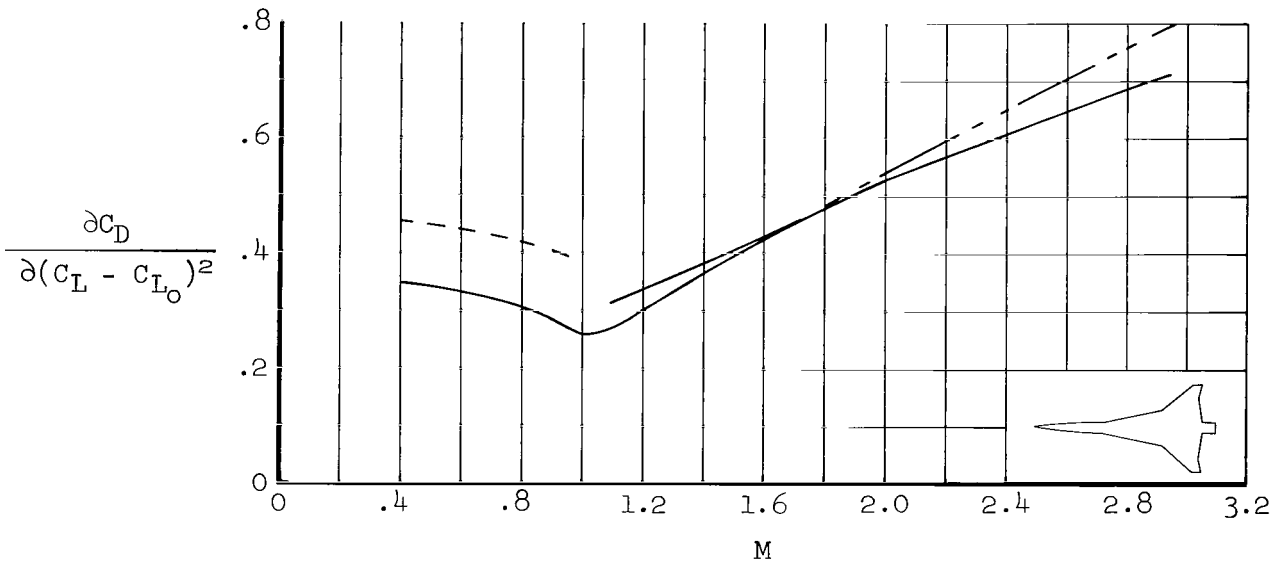


(d) Model 4

Figure 14.- Continued.

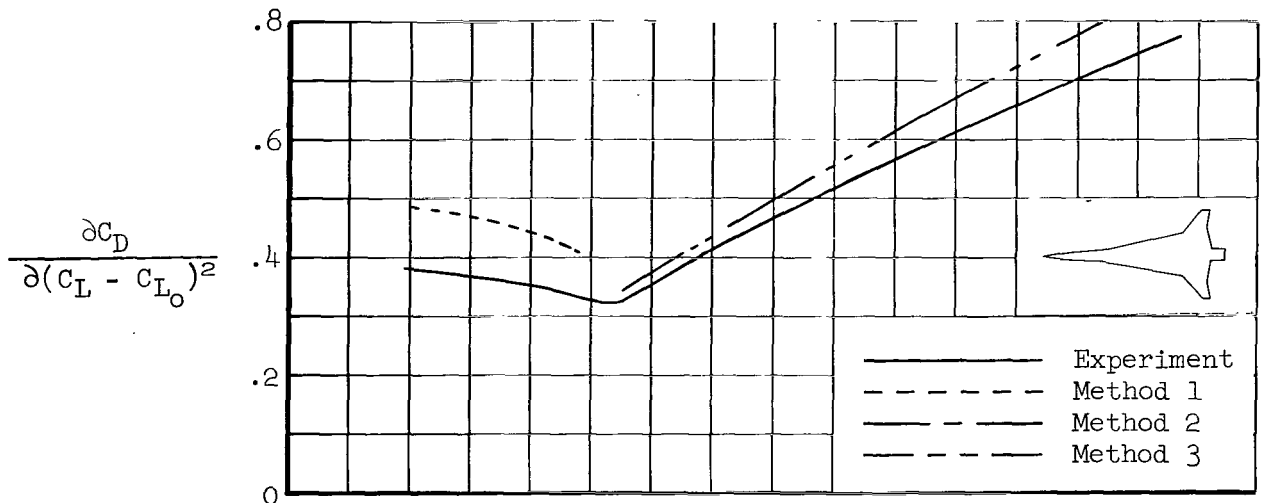


(e) Model 5

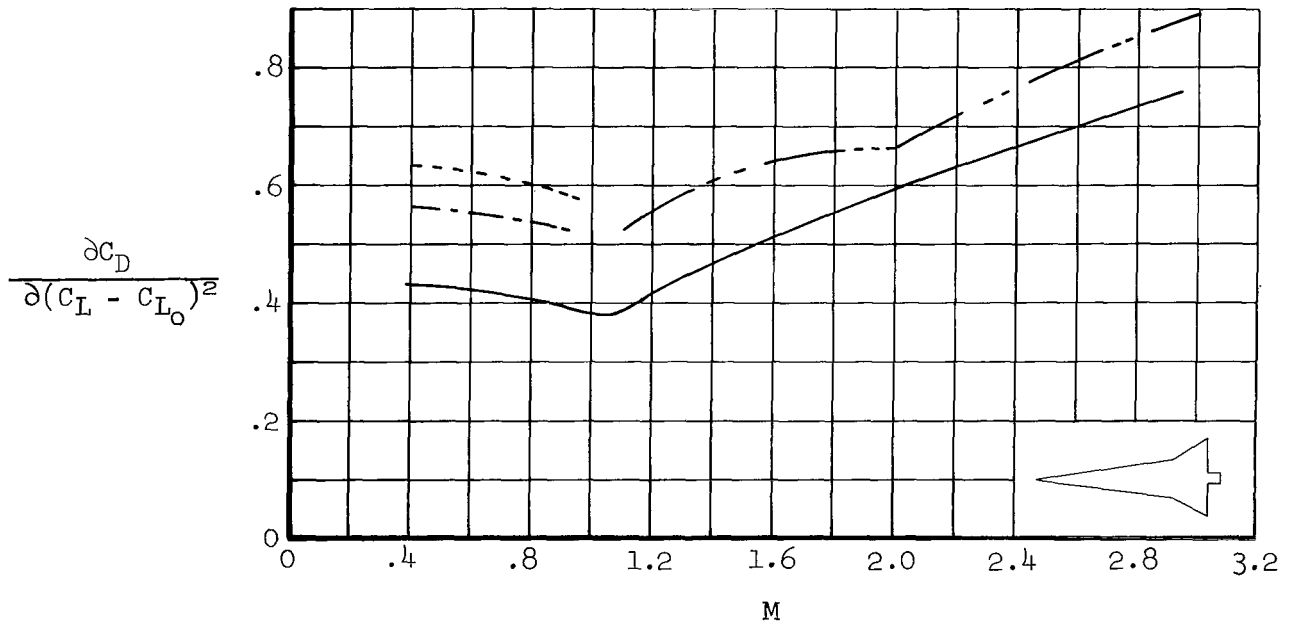


(f) Model 6

Figure 14.- Continued.

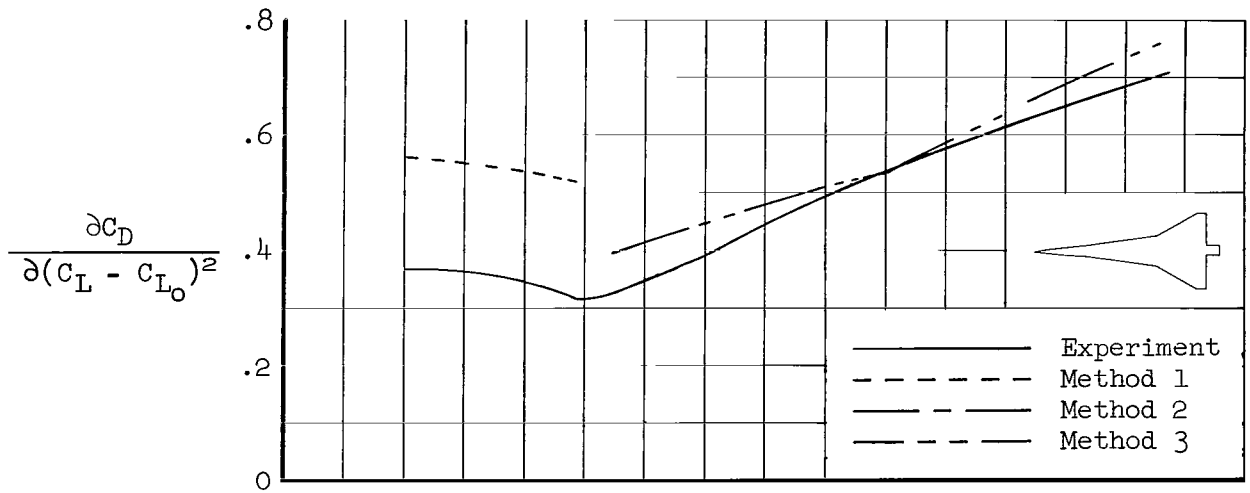


(g) Model 7

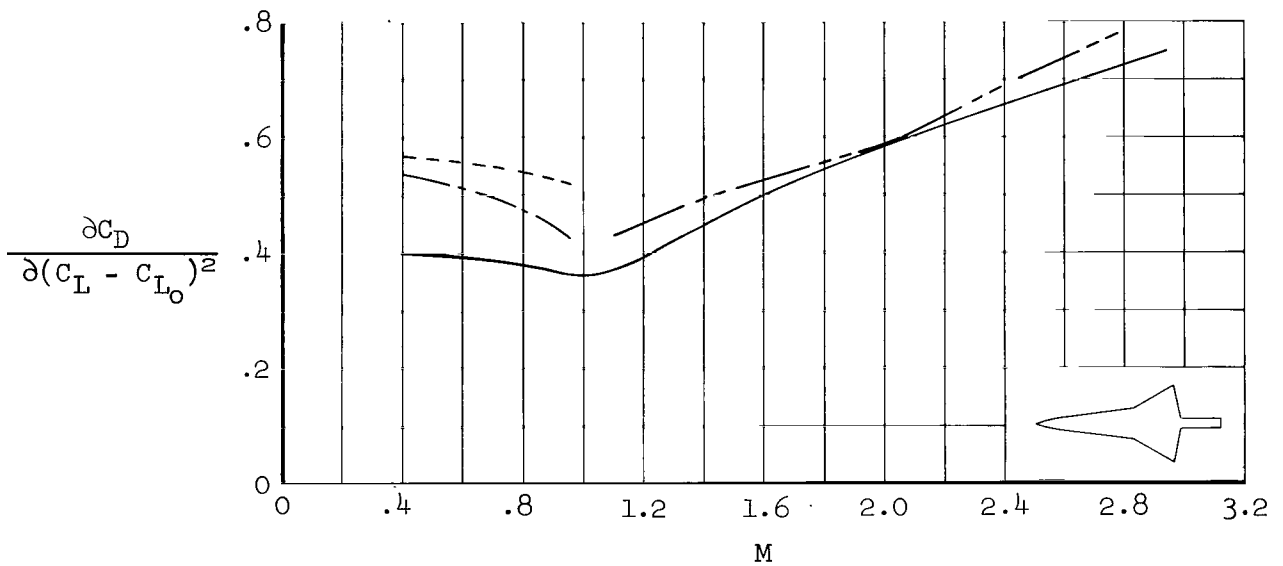


(h) Model 8

Figure 14.- Continued.

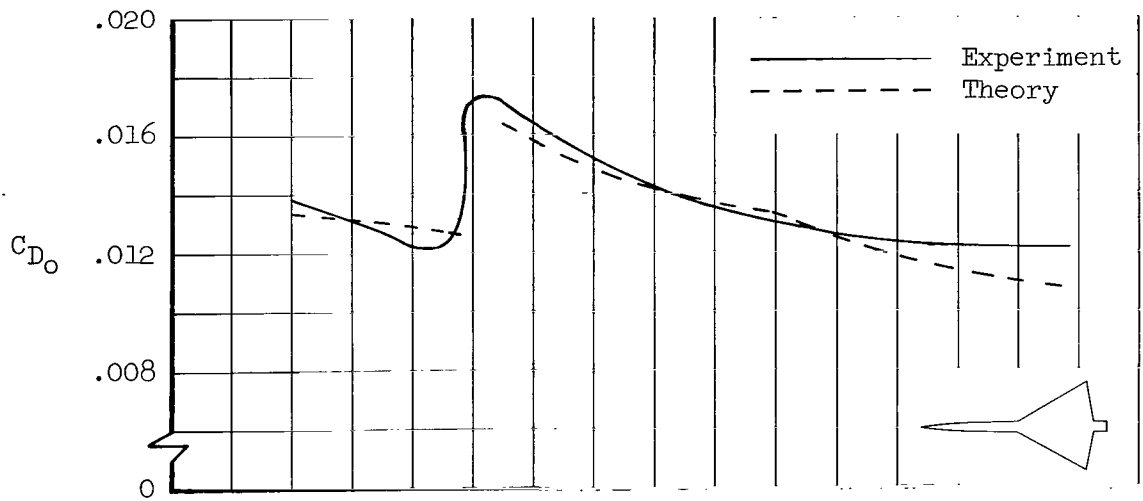


(i) Model 9

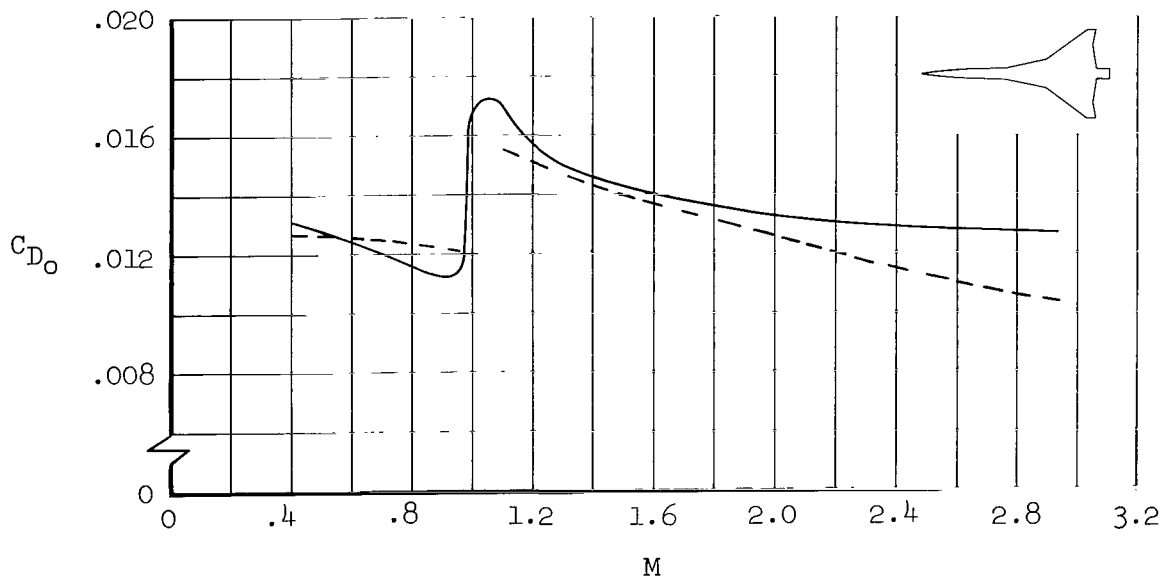


(j) Model 10

Figure 14.- Concluded.

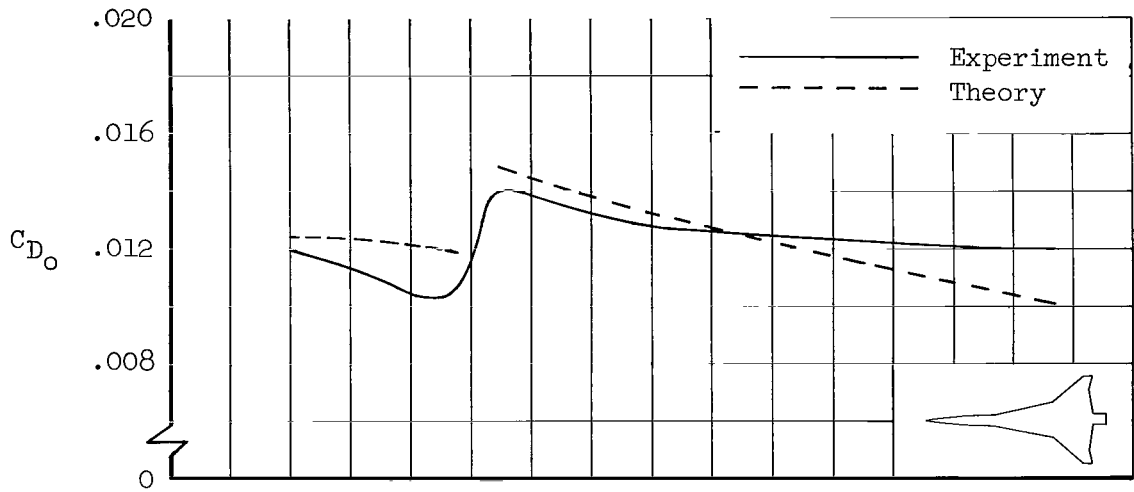


(a) Model 1

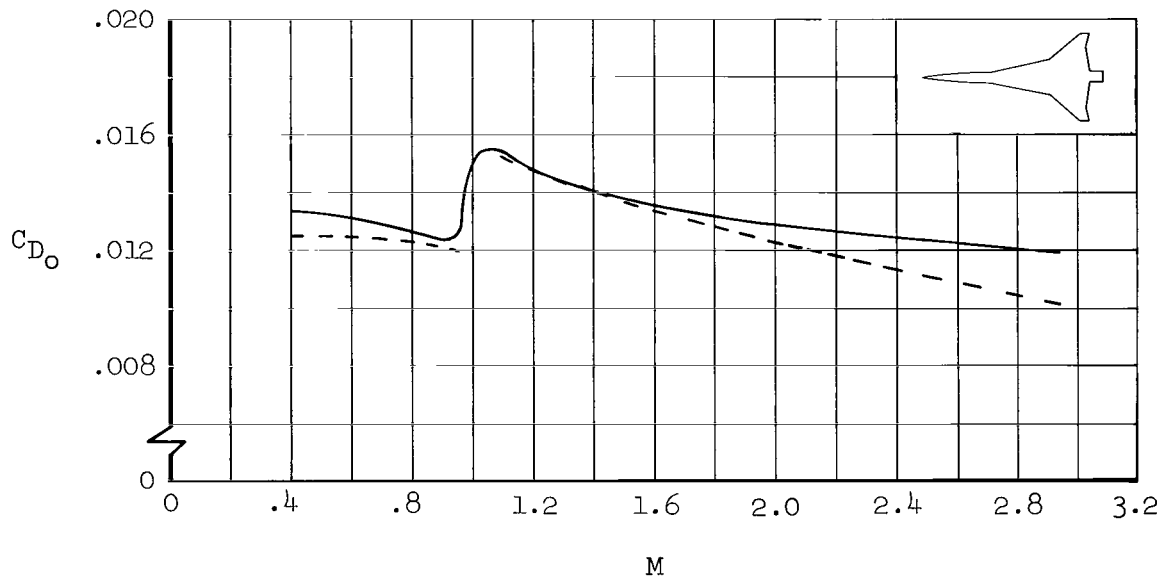


(b) Model 2

Figure 15.- Minimum drag coefficient as a function of Mach number.

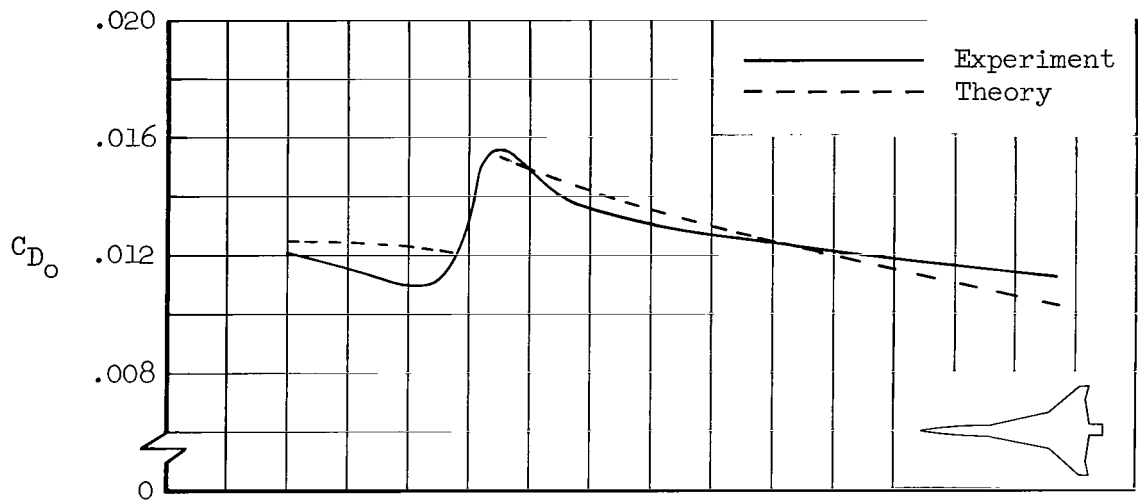


(c) Model 3

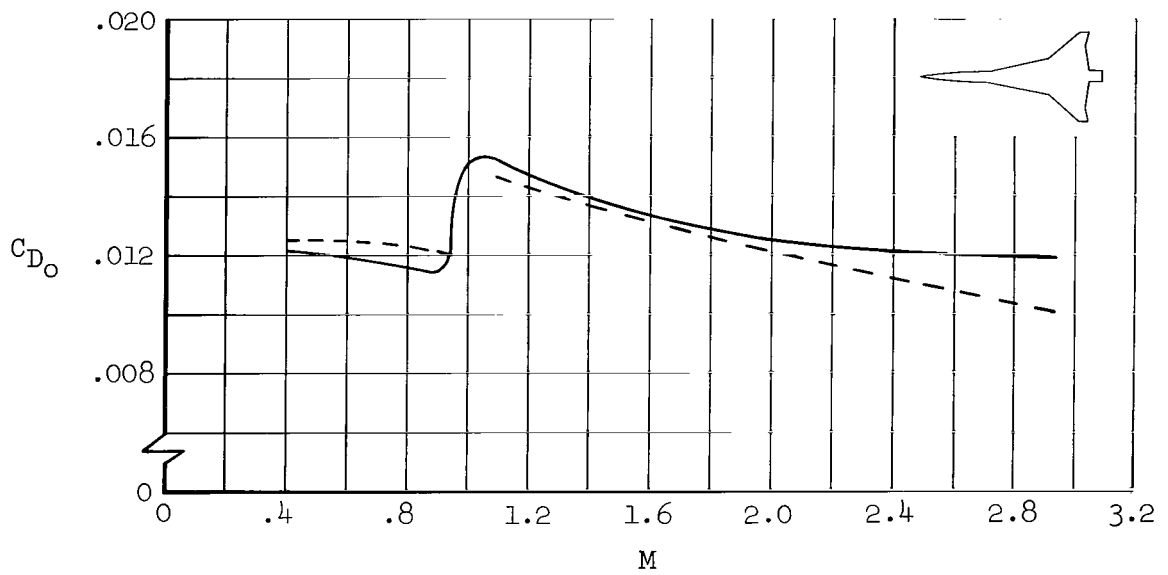


(d) Model 4

Figure 15.- Continued.

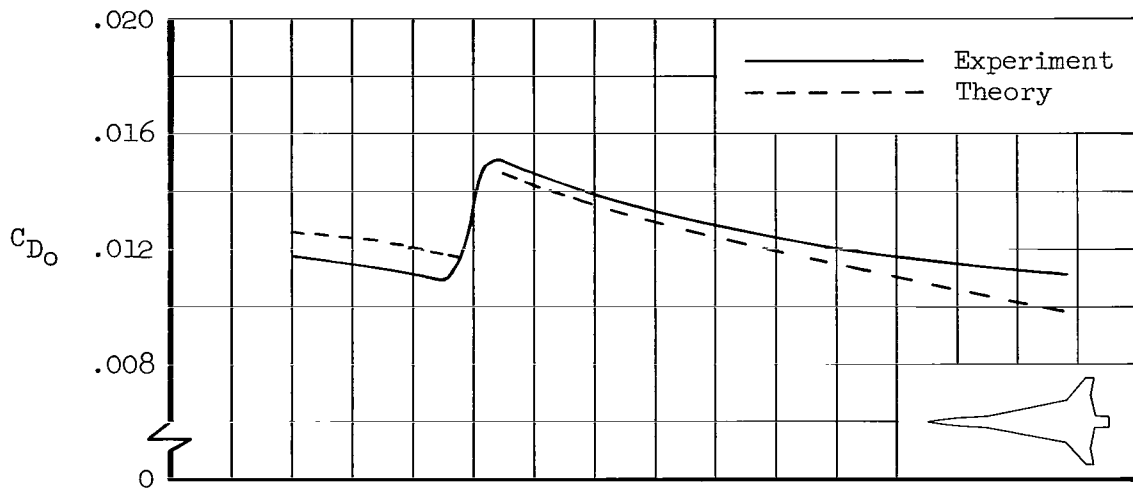


(e) Model 5

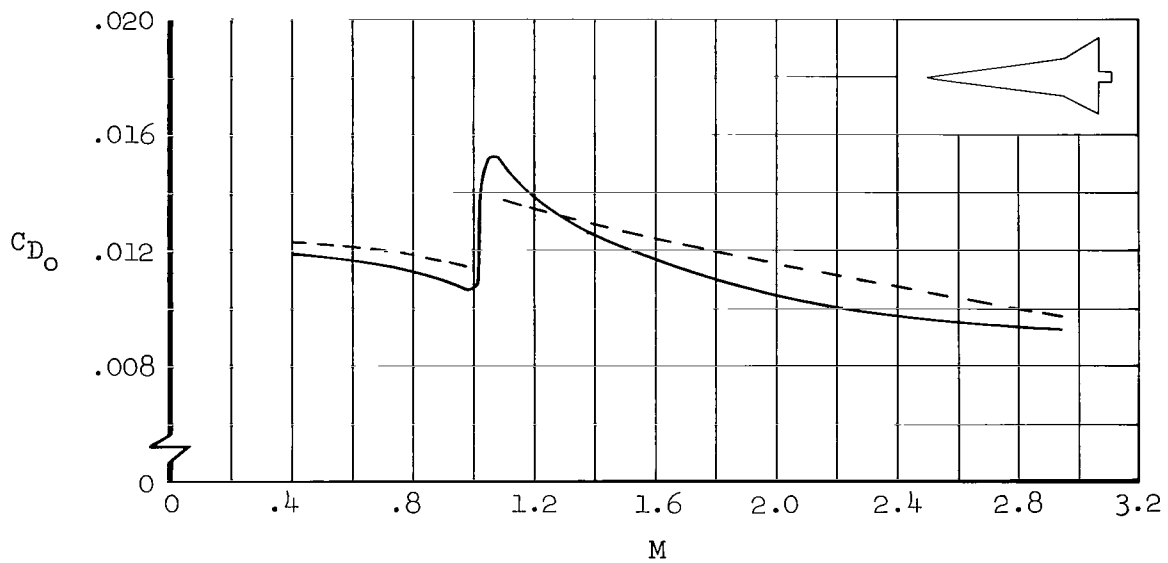


(f) Model 6

Figure 15.- Continued.

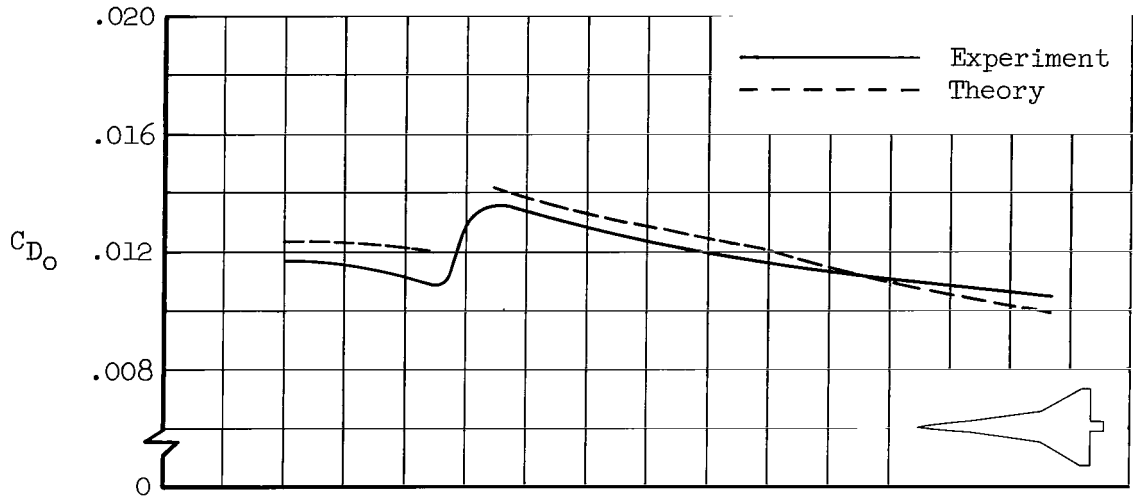


(g) Model 7

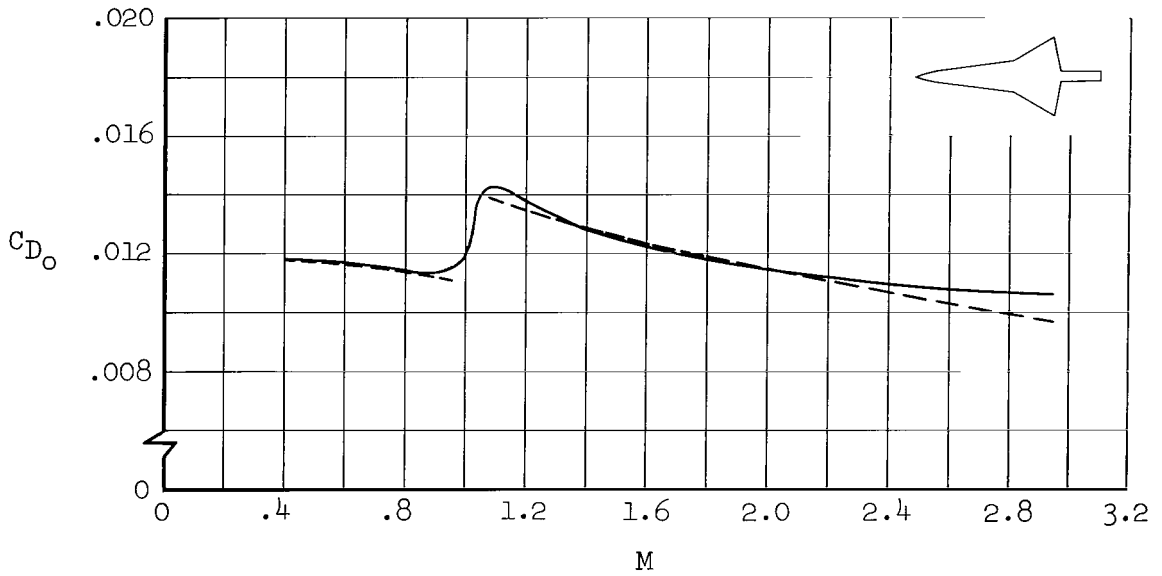


(h) Model 8

Figure 15.- Continued.

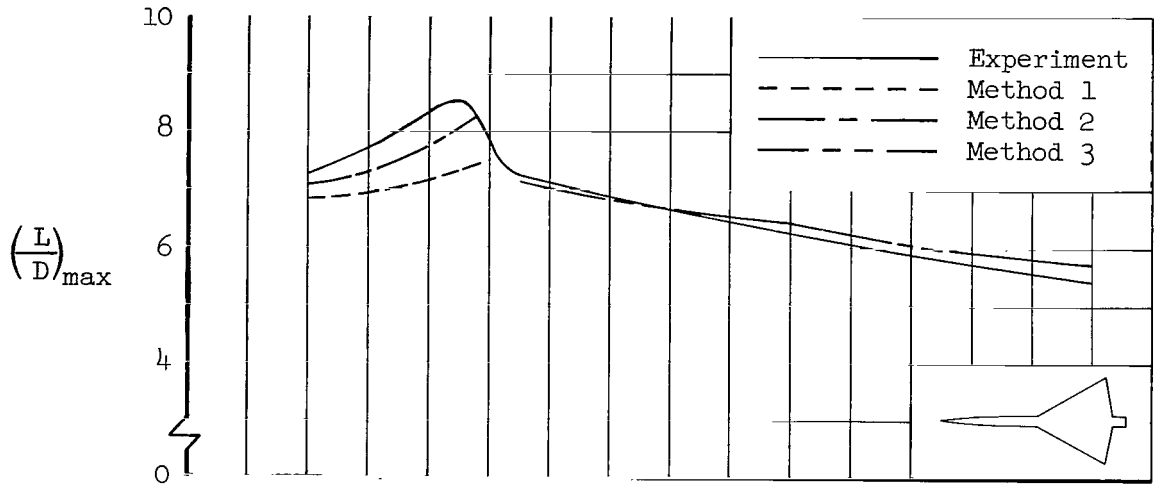


(i) Model 9

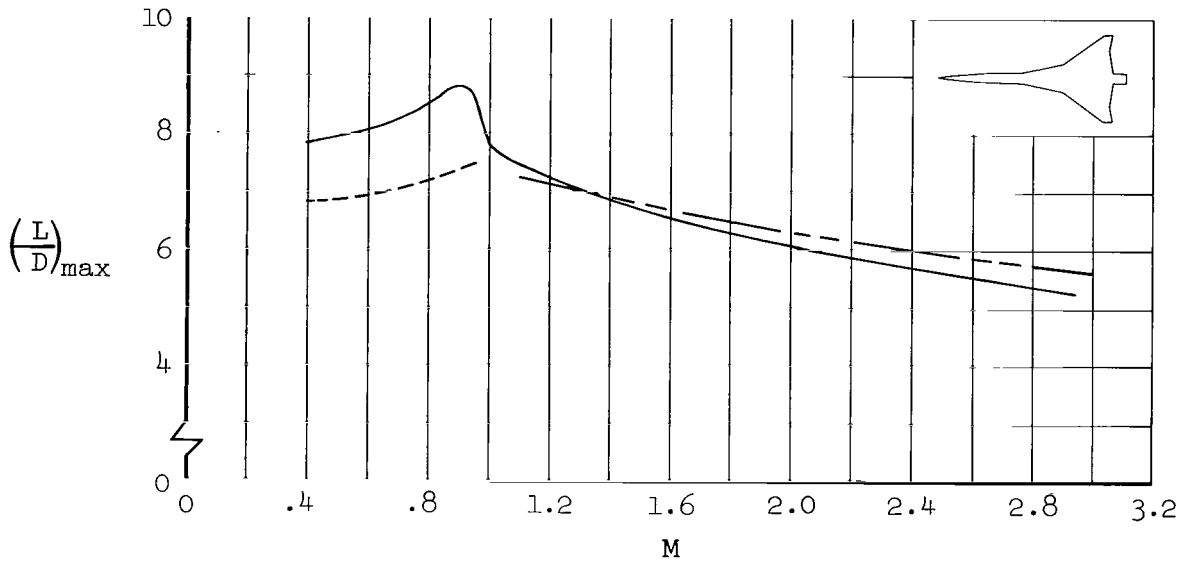


(j) Model 10

Figure 15.- Concluded.

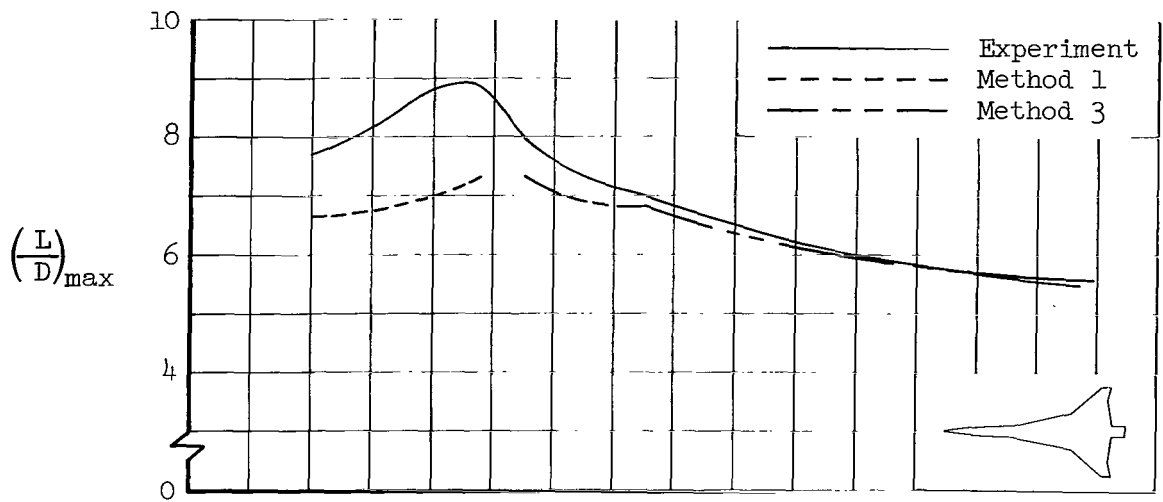


(a) Model 1

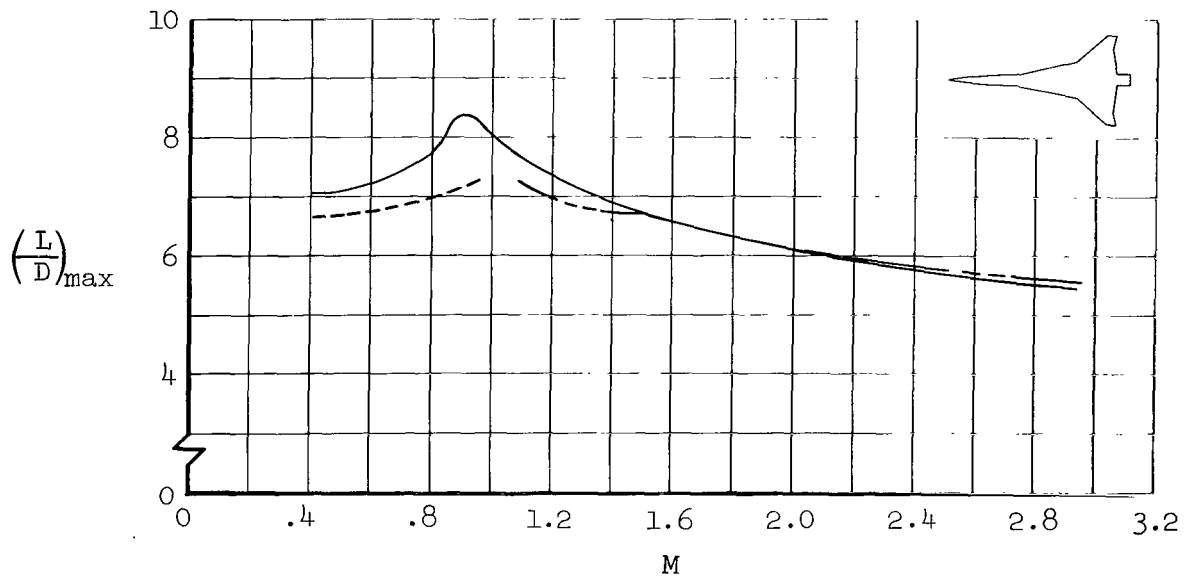


(b) Model 2

Figure 16.- Maximum lift-drag ratio as a function of Mach number.

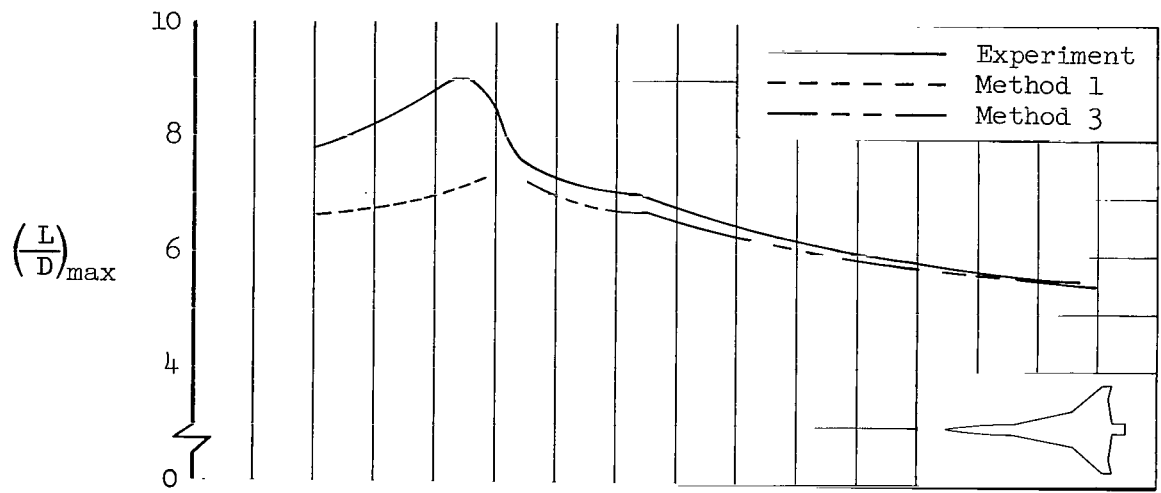


(c) Model 3

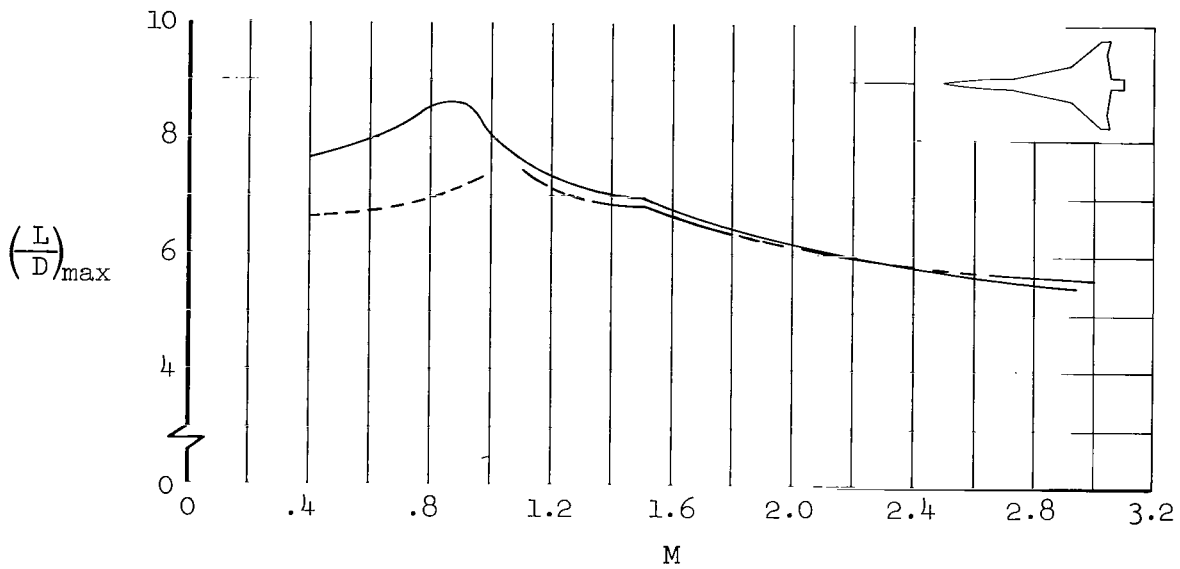


(d) Model 4

Figure 16.- Continued.

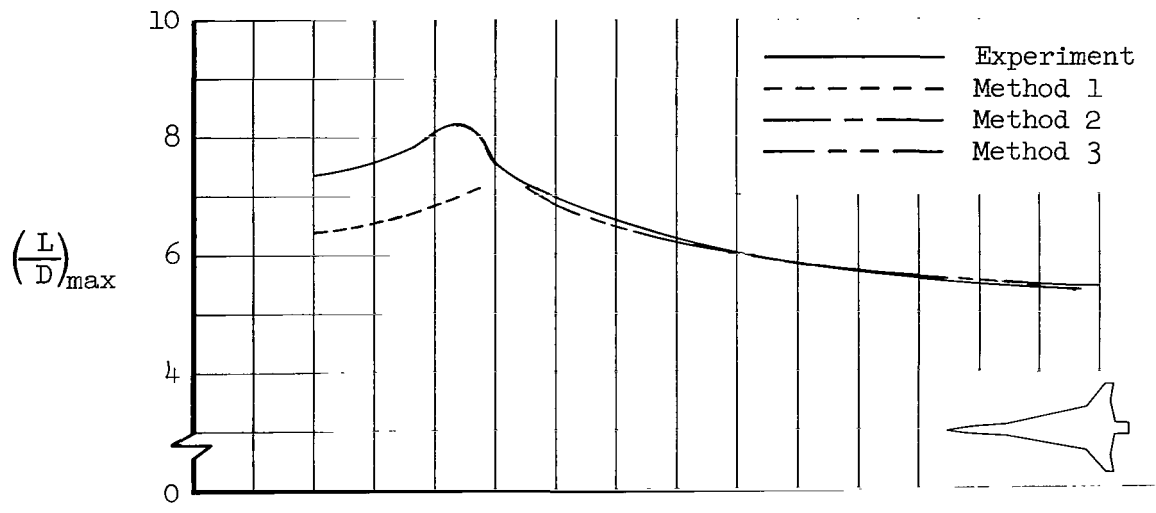


(e) Model 5

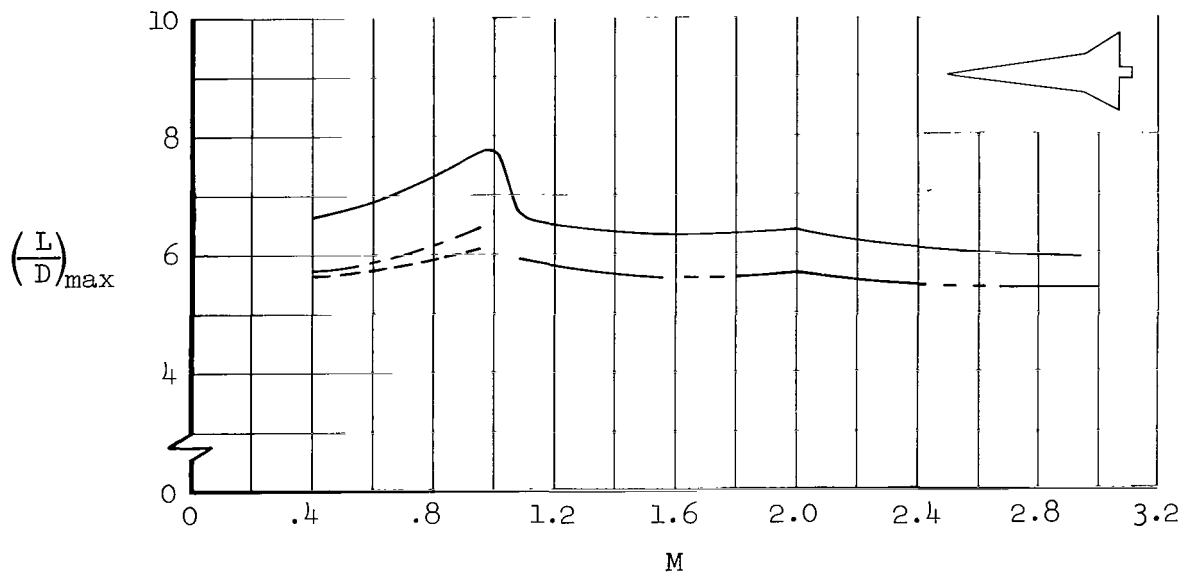


(f) Model 6

Figure 16.- Continued.

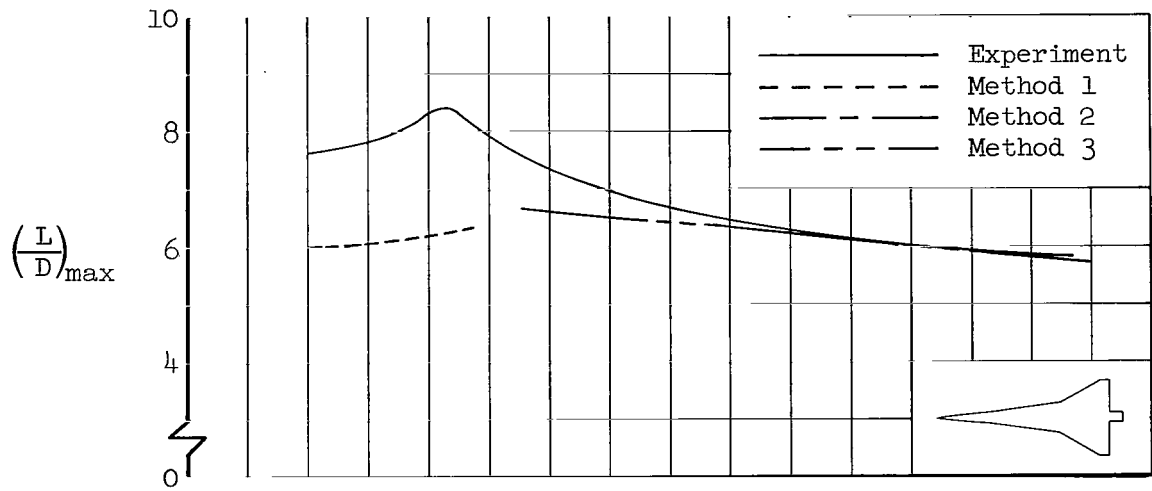


(g) Model 7

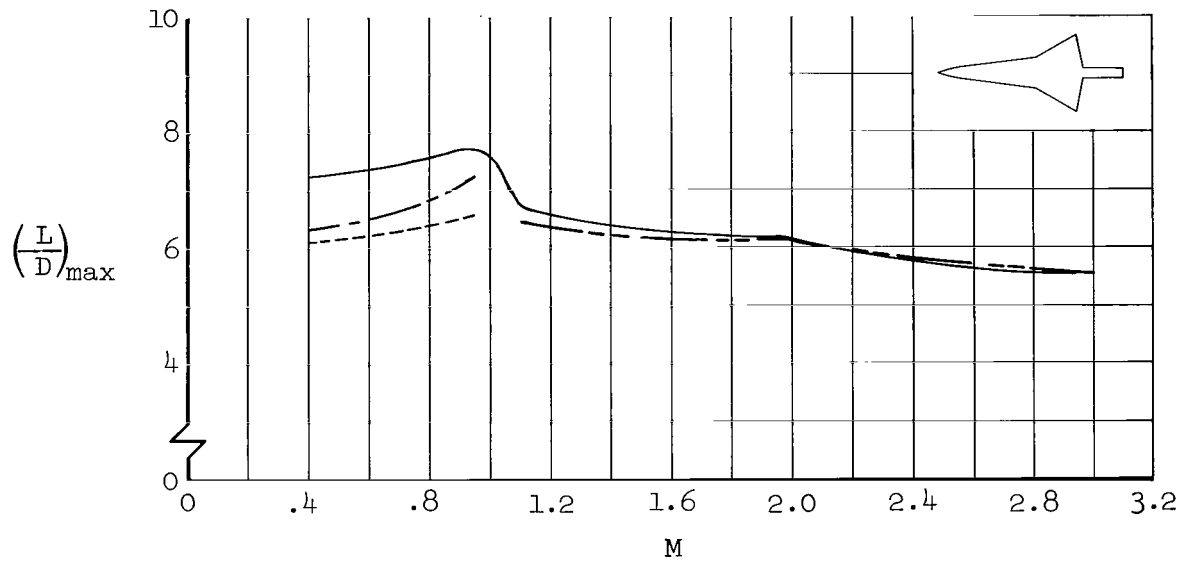


(h) Model 8

Figure 16.- Continued.

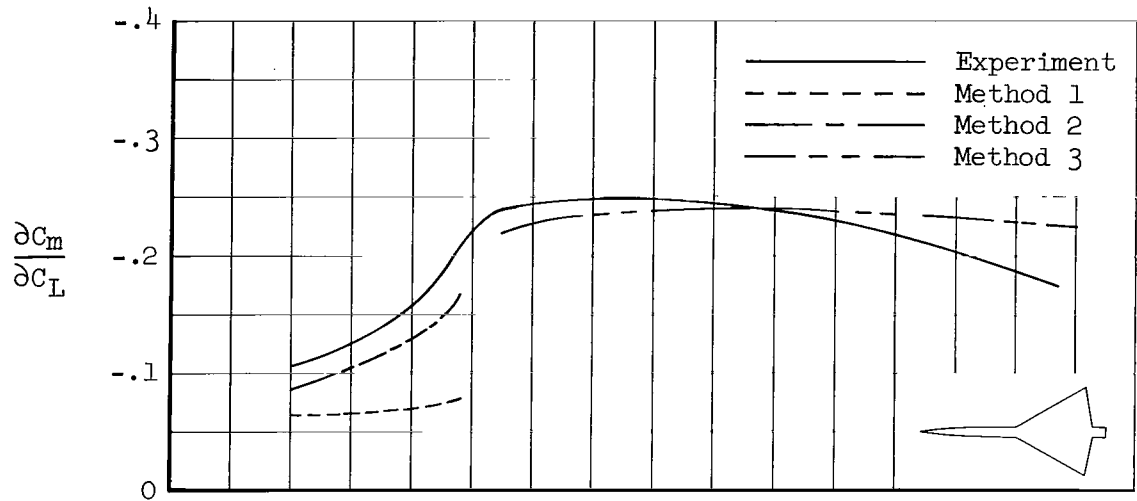


(i) Model 9

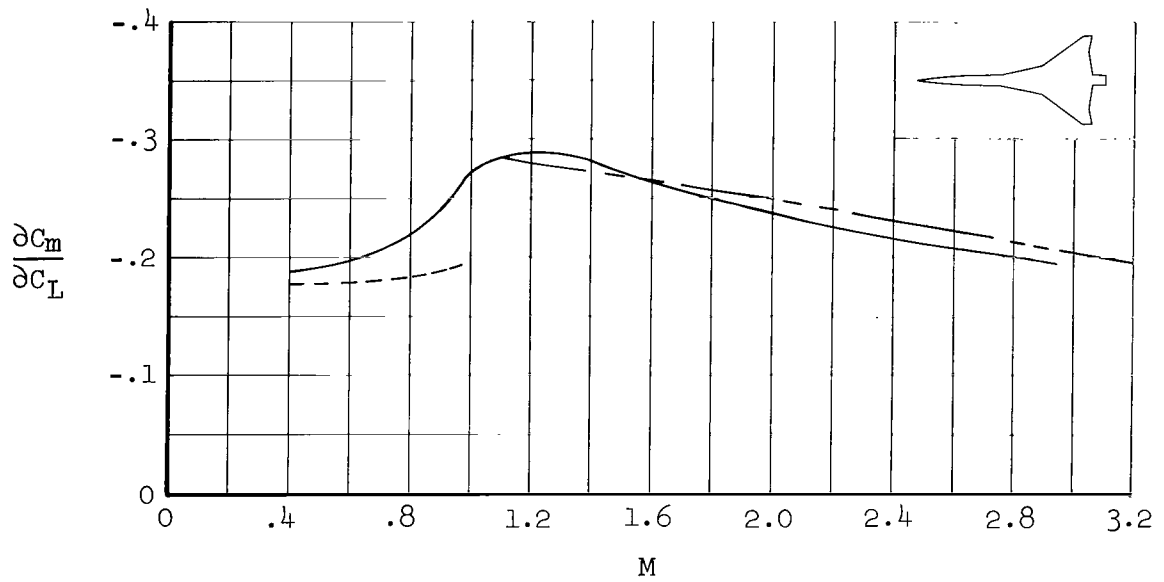


(j) Model 10

Figure 16.- Concluded.

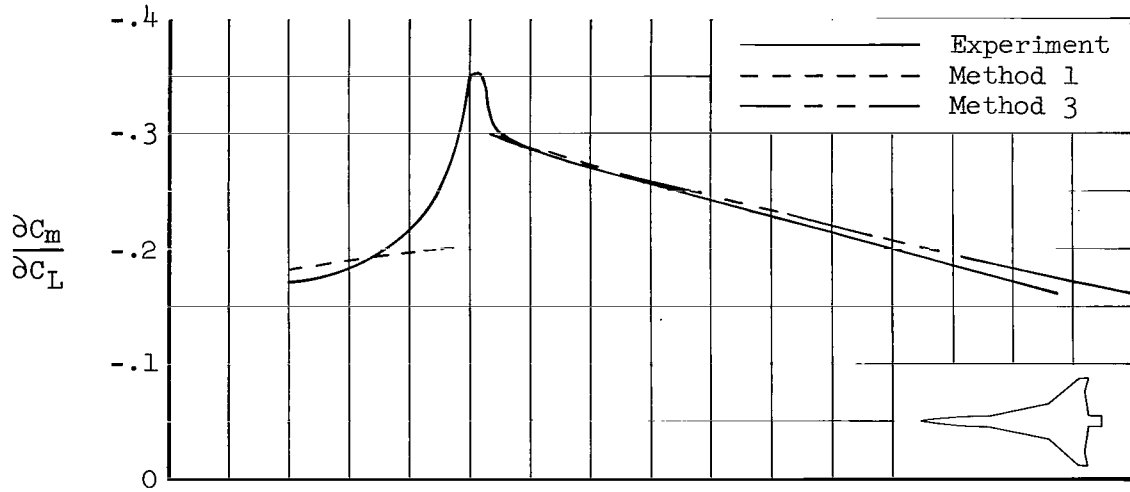


(a) Model 1

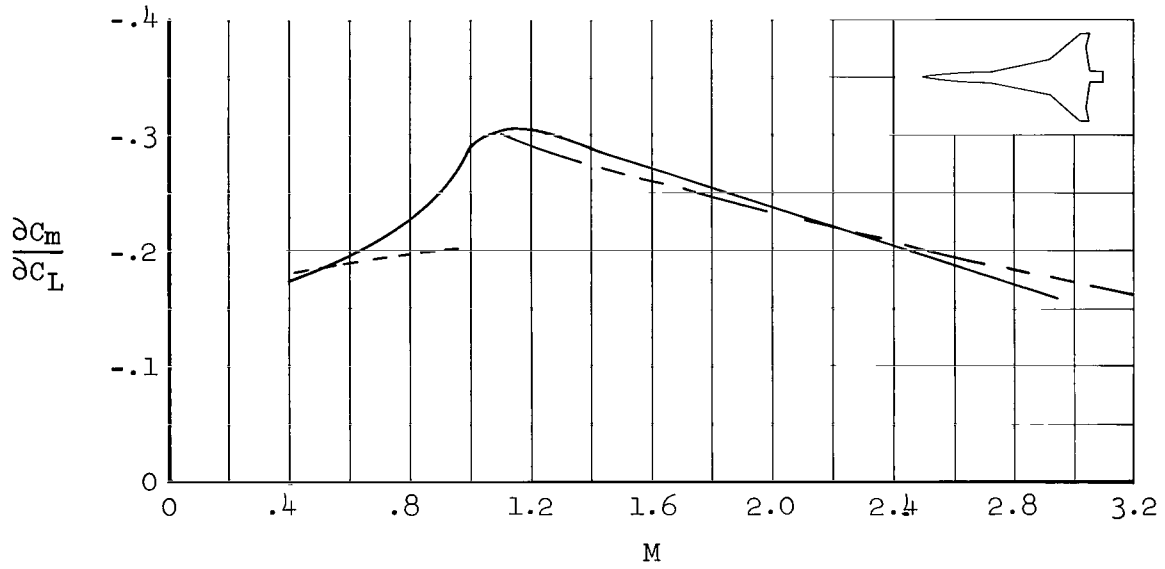


(b) Model 2

Figure 17.- Pitching-moment-curve slope as a function of Mach number.

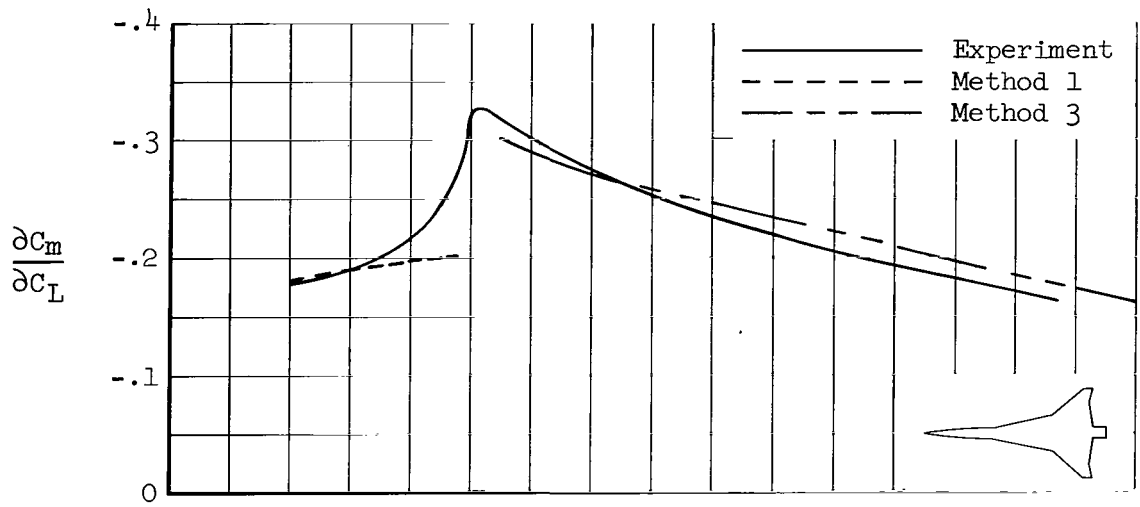


(c) Model 3

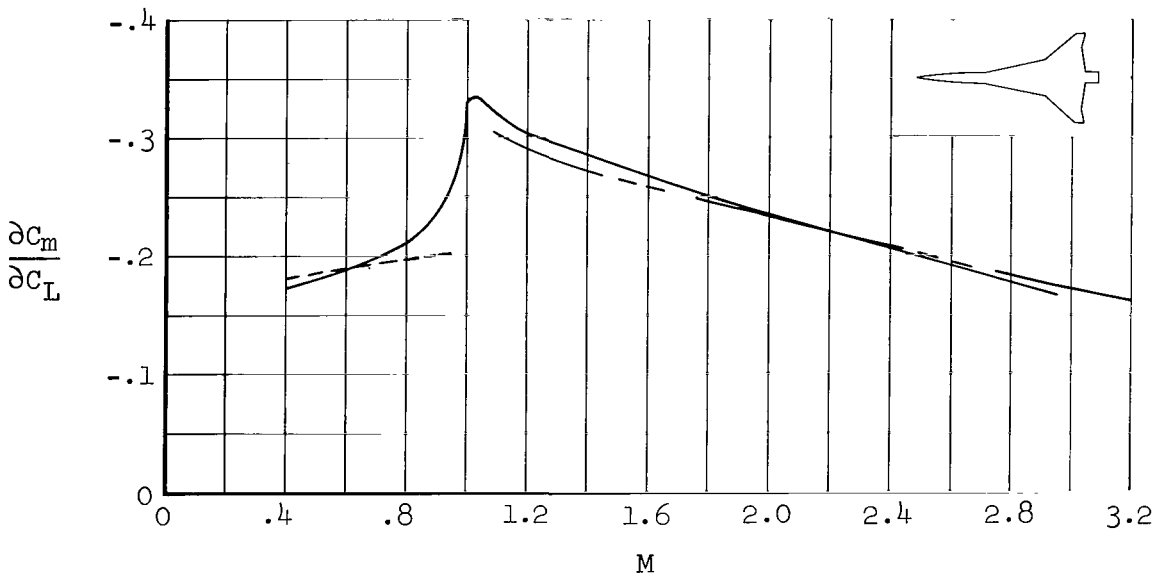


(d) Model 4

Figure 17.- Continued.

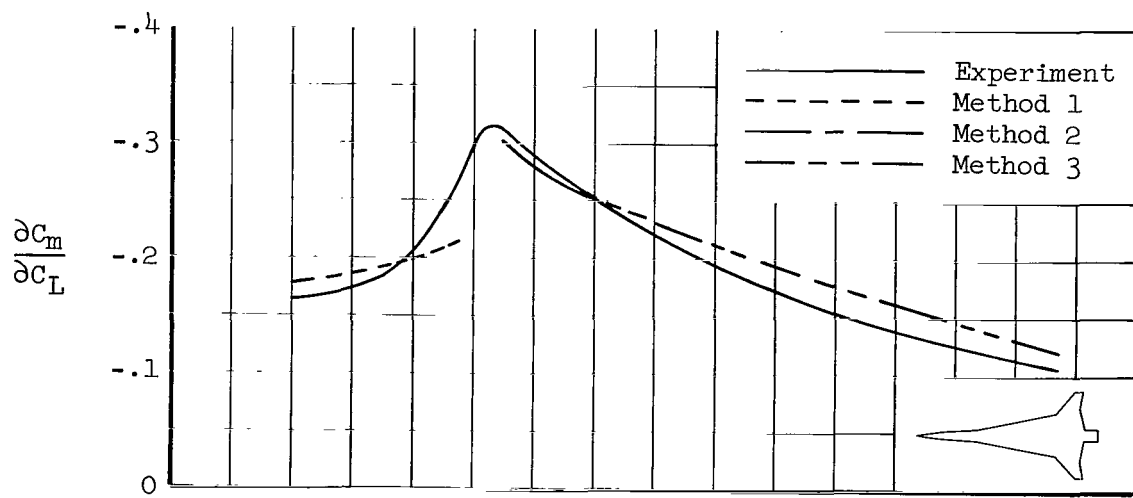


(e) Model 5

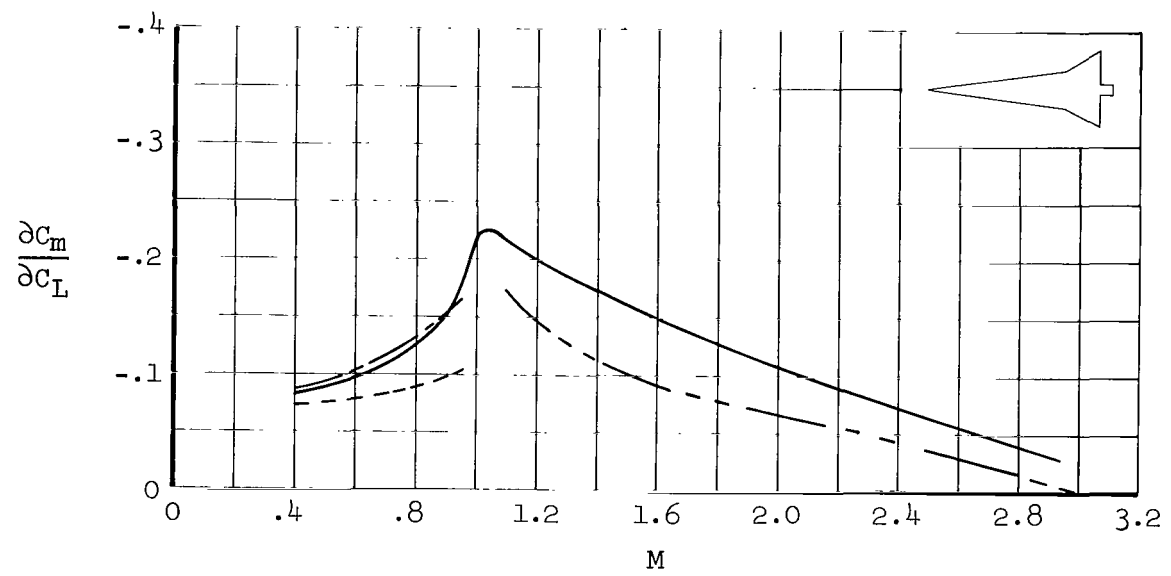


(f) Model 6

Figure 17.- Continued.

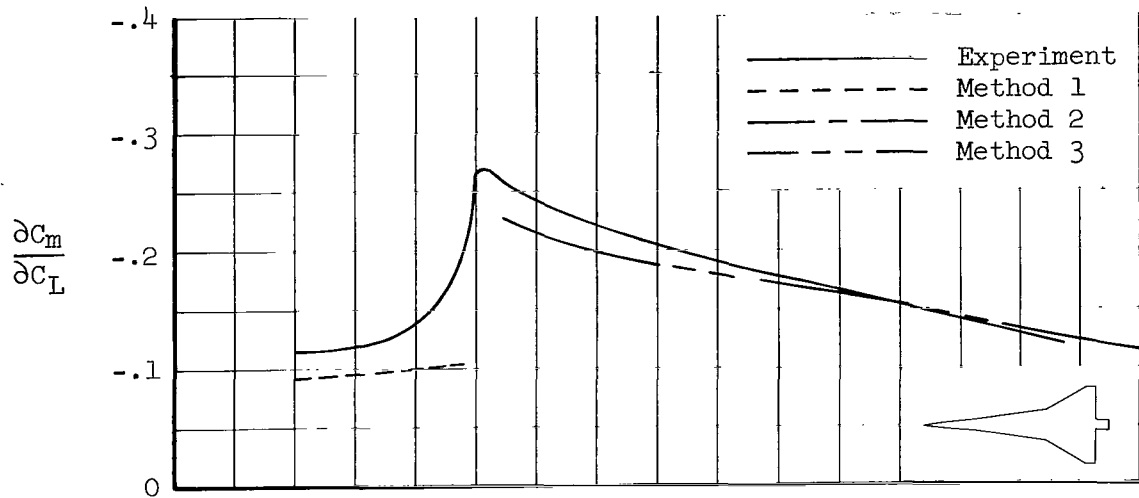


(g) Model 7

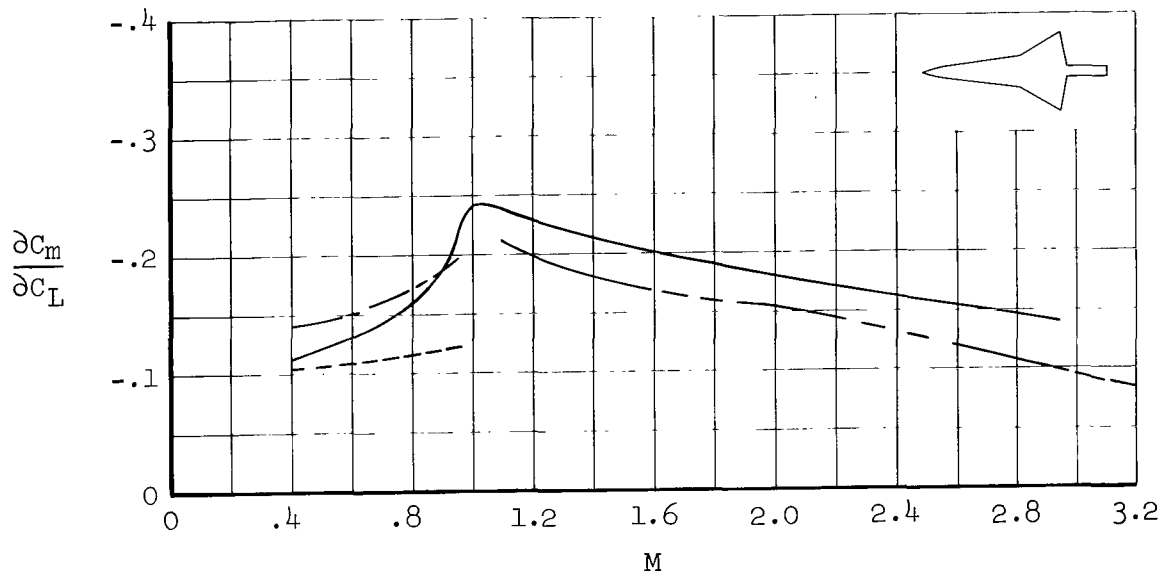


(h) Model 8

Figure 17.- Continued.

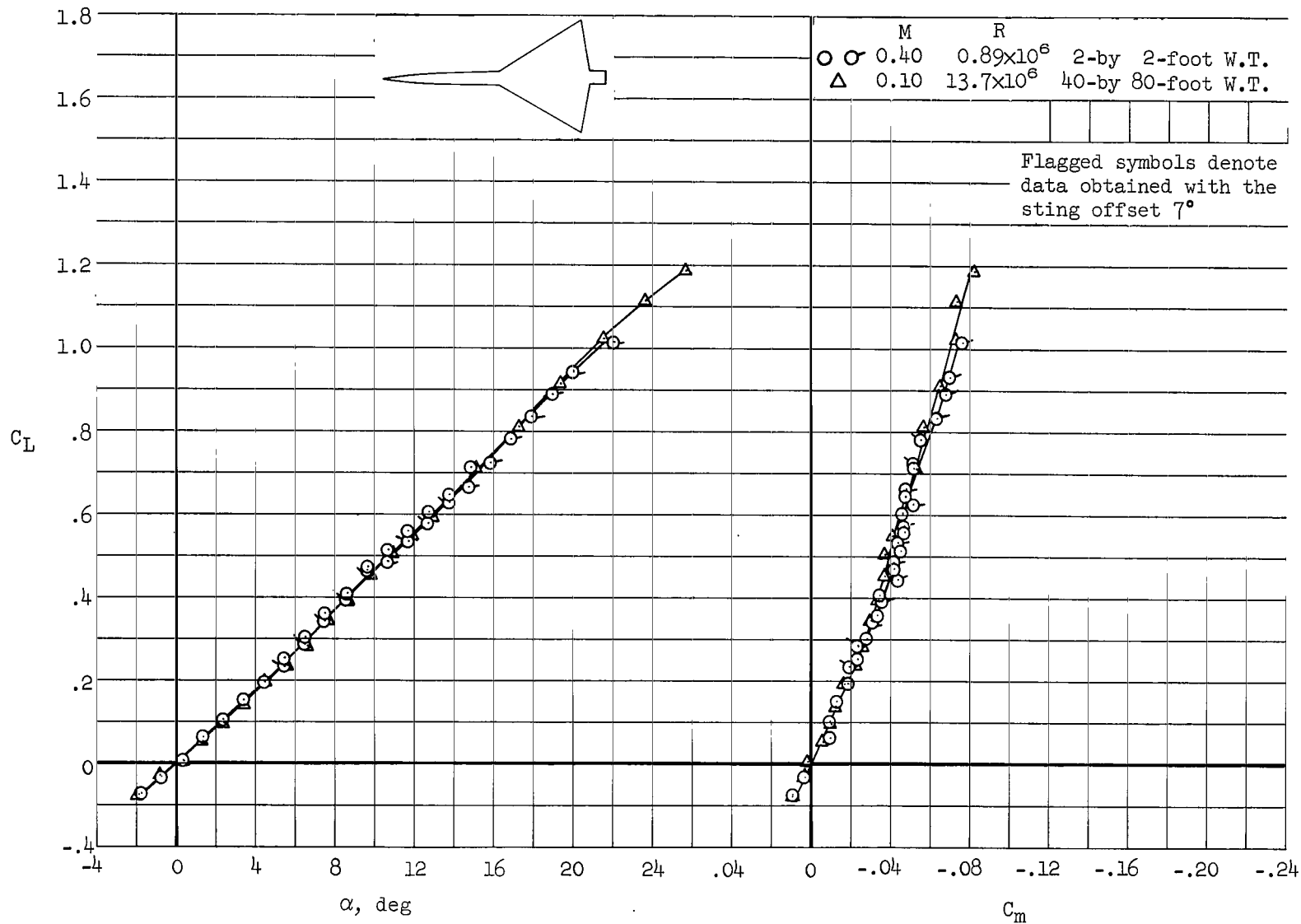


(i) Model 9



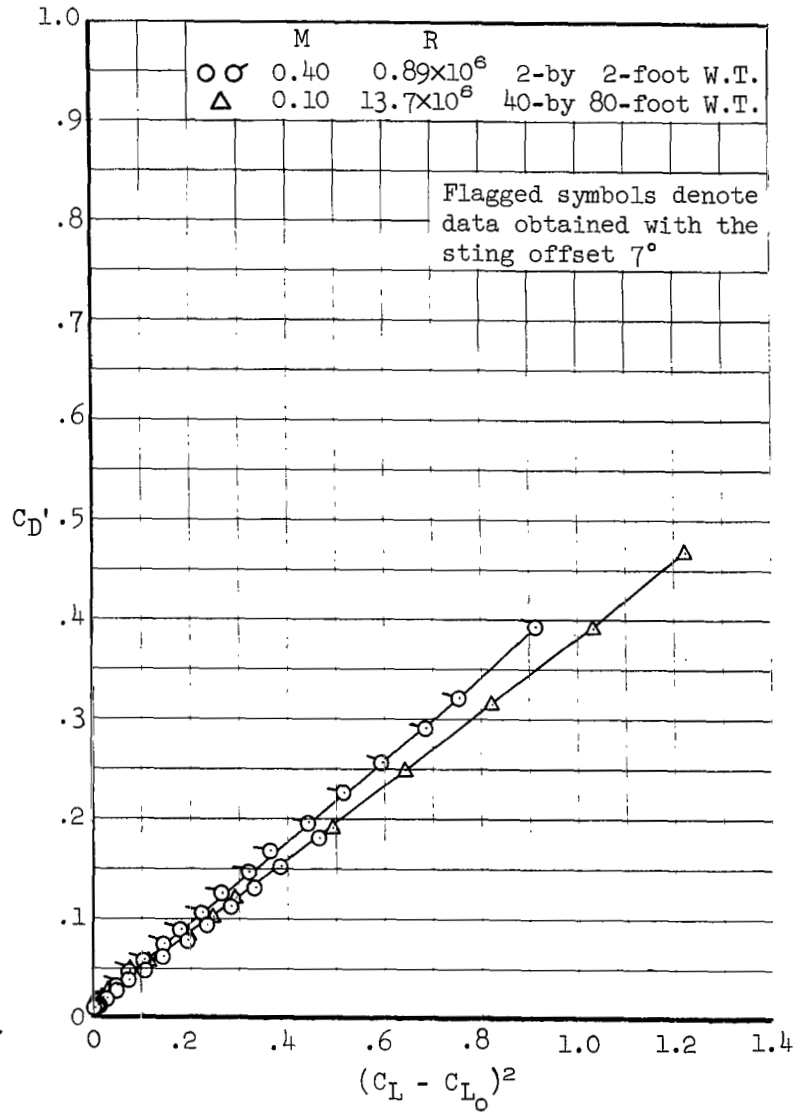
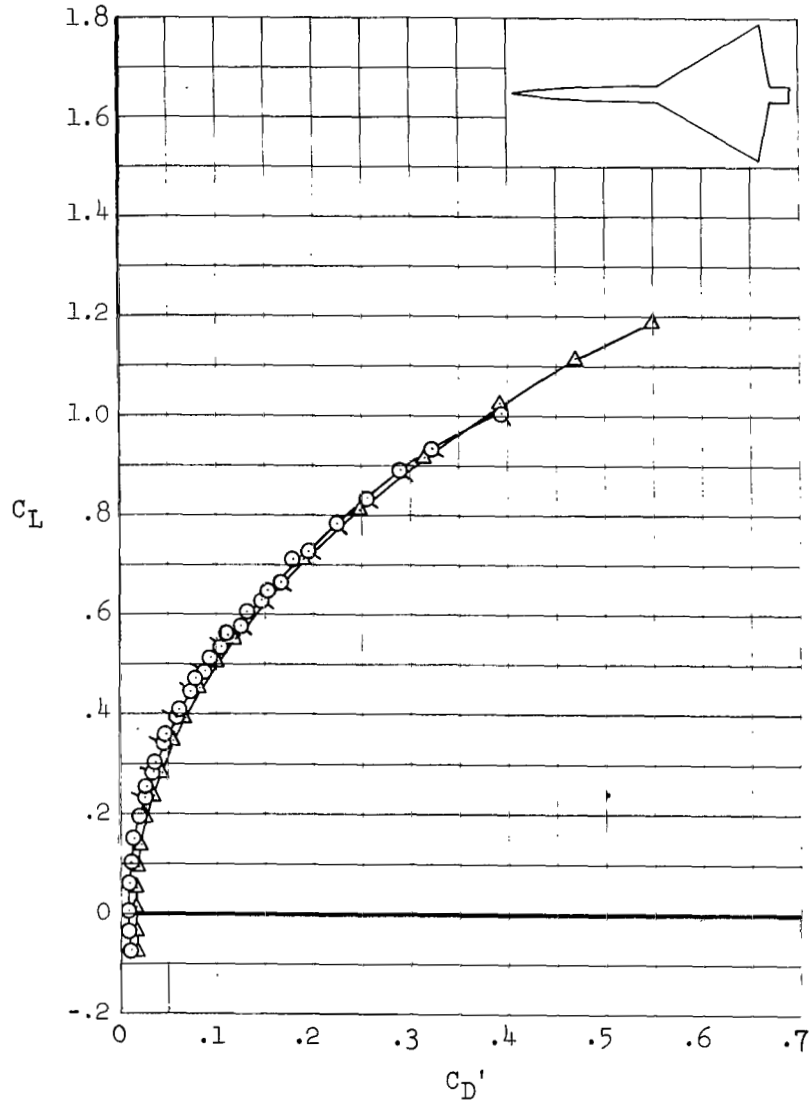
(j) Model 10

Figure 17.- Concluded.



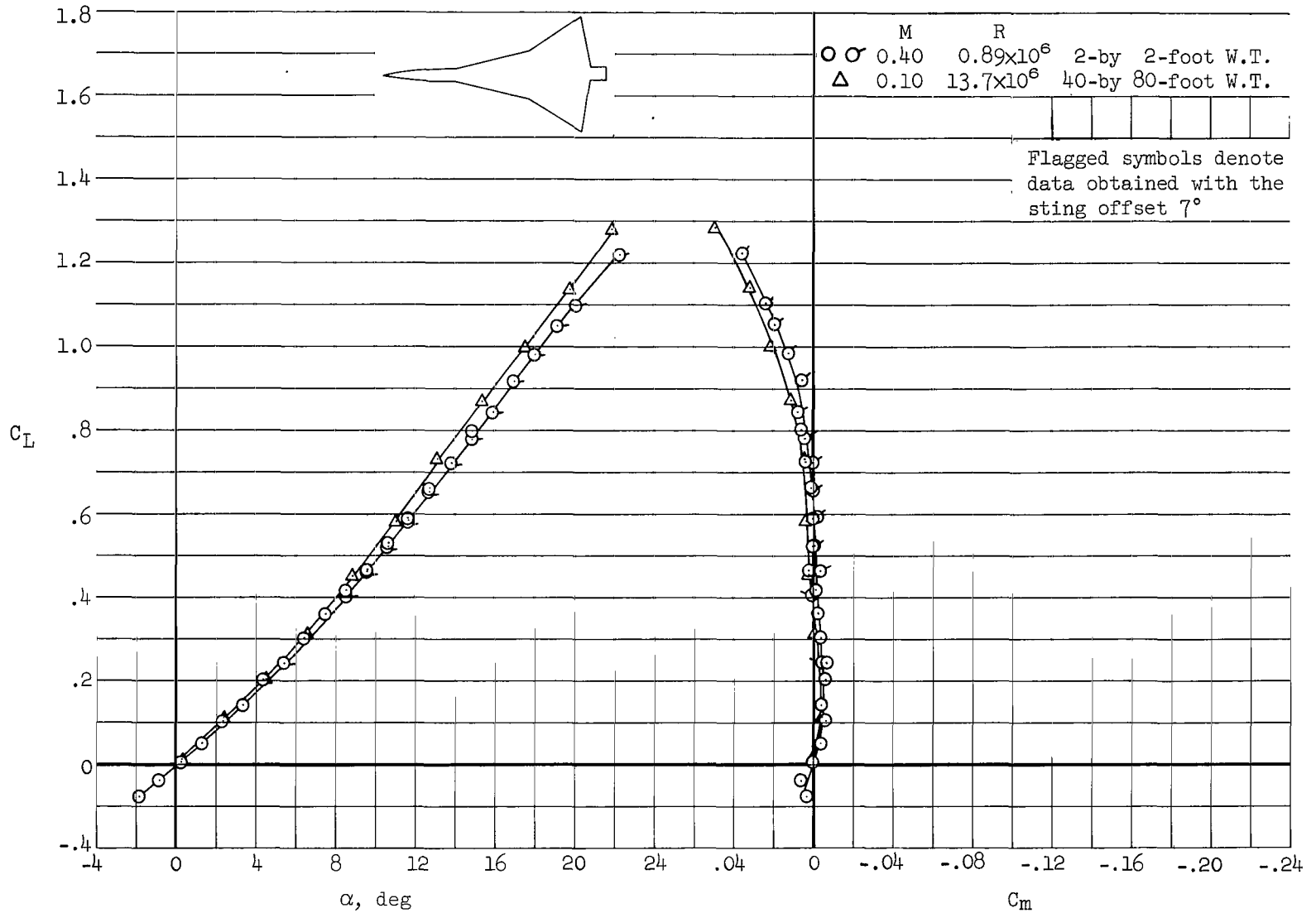
(a) C_L vs. α and C_L vs. C_m

Figure 18.- Reynolds number effects on the lift, drag, and pitching-moment characteristics of model 1.



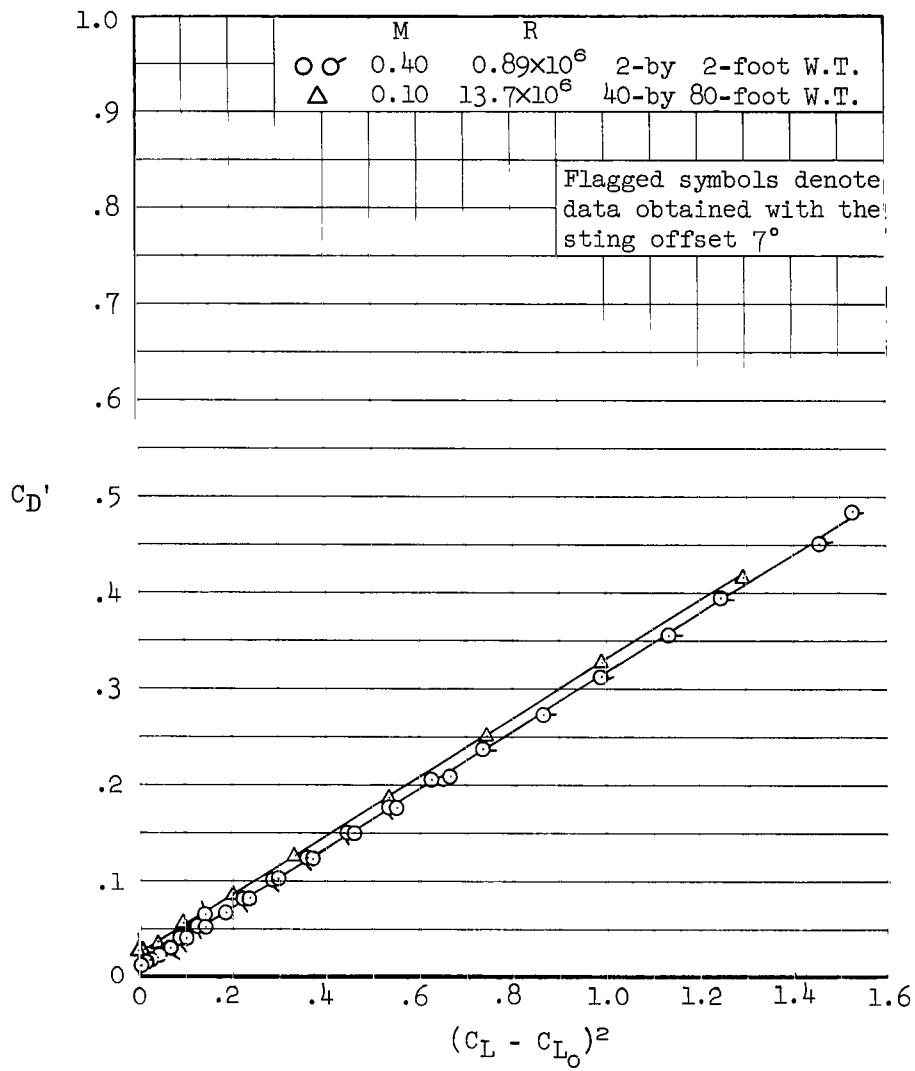
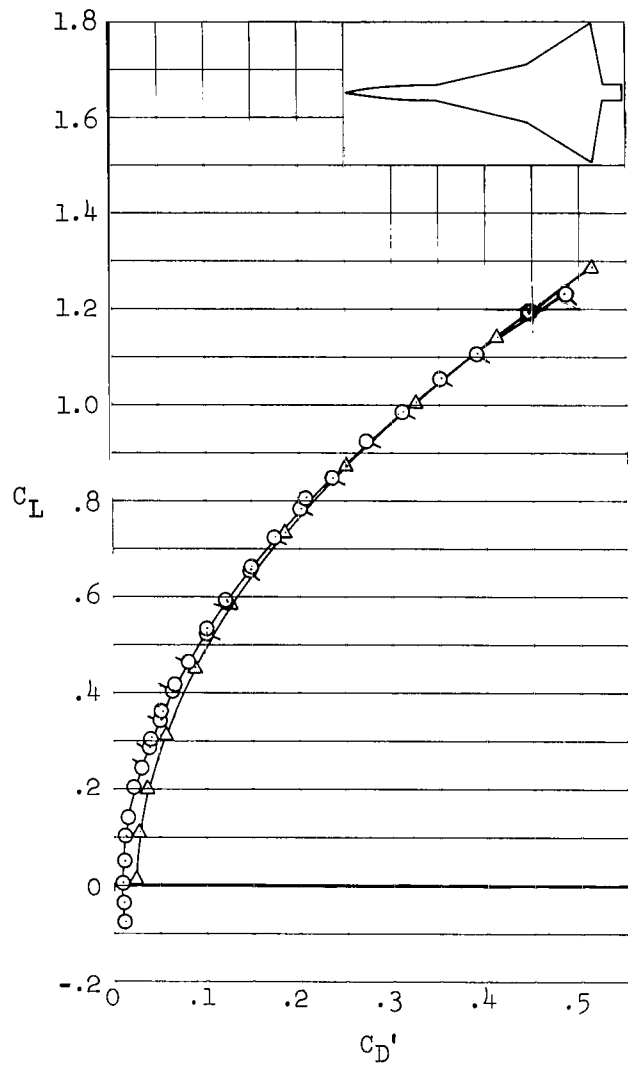
(b) C_L vs. C_D' and C_D' vs. $(C_L - C_{L_0})^2$

Figure 18.- Concluded.



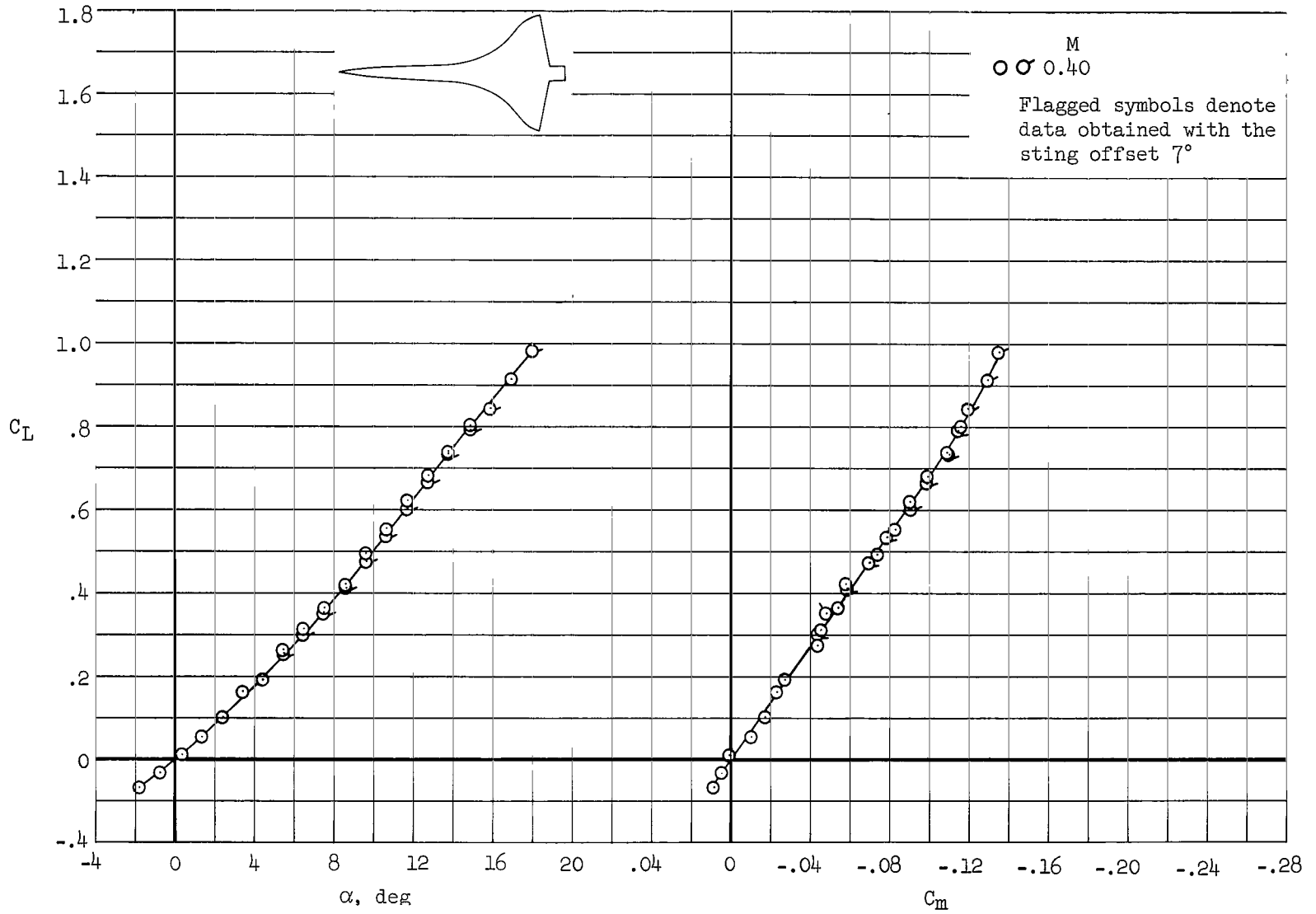
(a) C_L vs. α and C_L vs. C_m

Figure 19.- Reynolds number effects on the lift, drag, and pitching-moment characteristics of model 11.



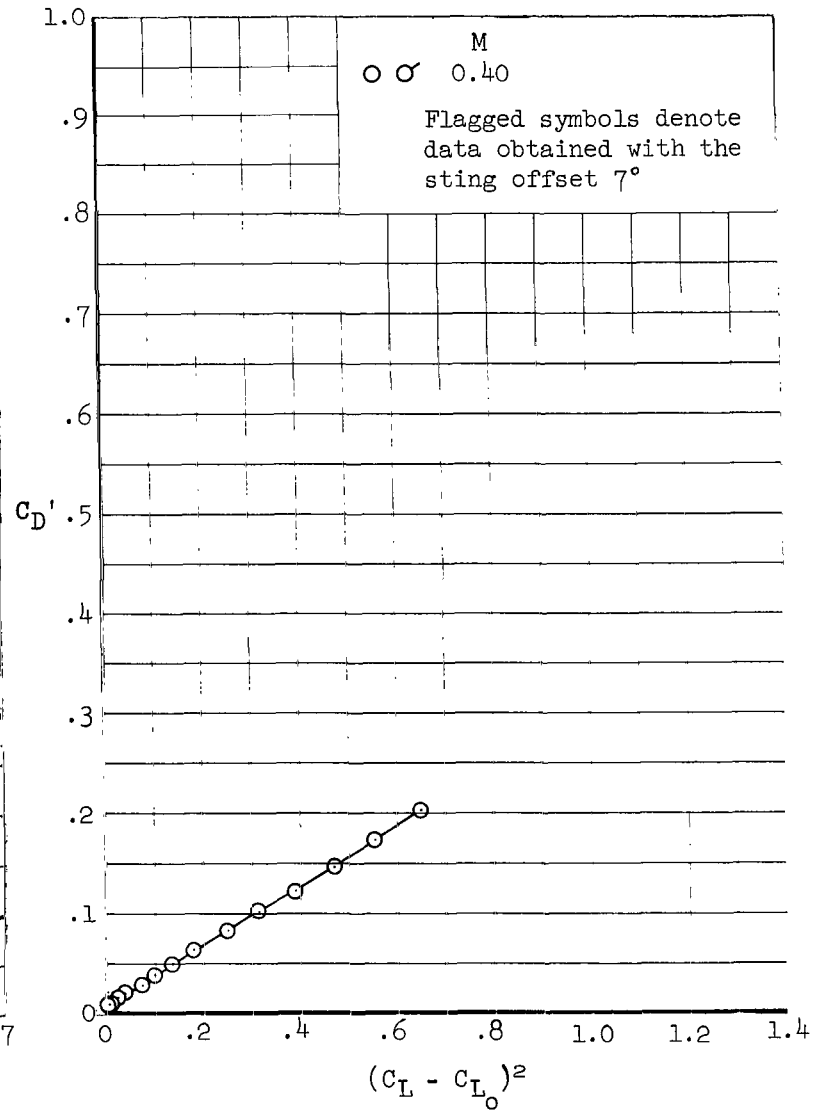
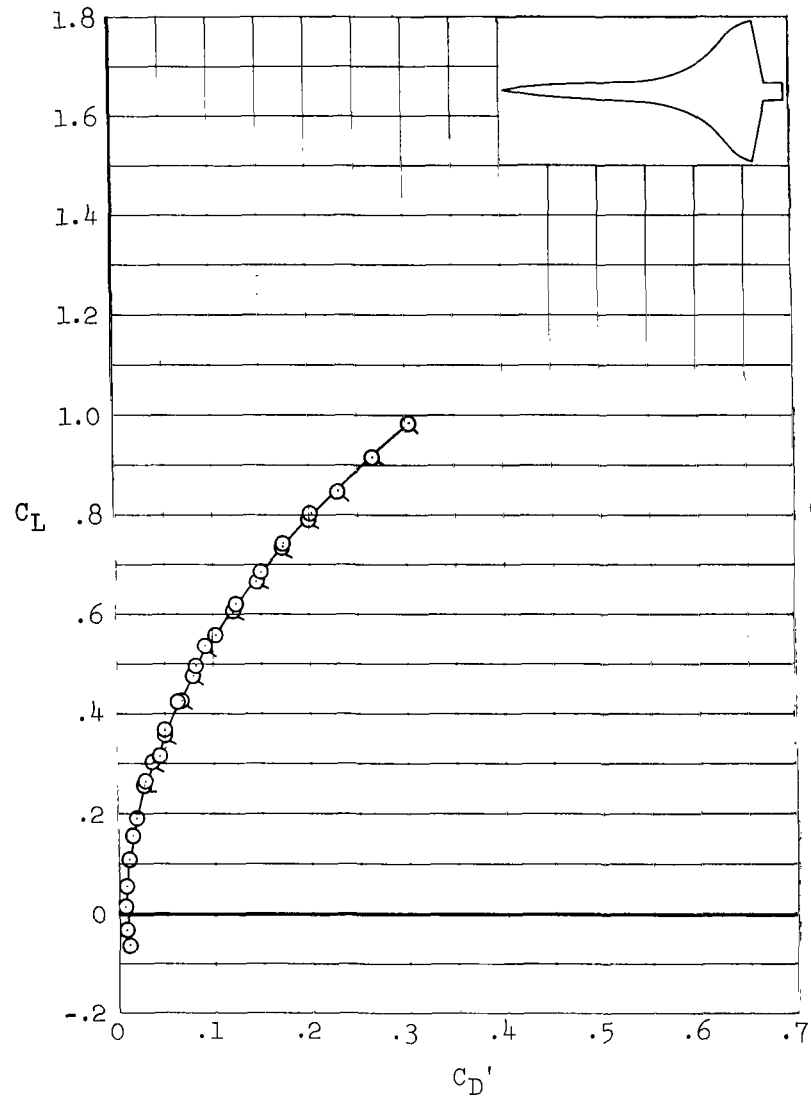
(b) C_L vs. C_D' and C_D' vs. $(C_L - C_{L_0})^2$

Figure 19.- Concluded.



(a) C_L vs. α and C_L vs. C_m

Figure 20.- Lift, drag, and pitching-moment characteristics of model Ogee 1 at a Mach of 0.4.



(b) C_L vs. C_D' and C_D' vs. $(C_L - C_{L_0})^2$

Figure 20.- Concluded.

"The aeronautical and space activities of the United States shall be conducted so as to contribute . . . to the expansion of human knowledge of phenomena in the atmosphere and space. The Administration shall provide for the widest practicable and appropriate dissemination of information concerning its activities and the results thereof."

—NATIONAL AERONAUTICS AND SPACE ACT OF 1958

NASA SCIENTIFIC AND TECHNICAL PUBLICATIONS

TECHNICAL REPORTS: Scientific and technical information considered important, complete, and a lasting contribution to existing knowledge.

TECHNICAL NOTES: Information less broad in scope but nevertheless of importance as a contribution to existing knowledge.

TECHNICAL MEMORANDUMS: Information receiving limited distribution because of preliminary data, security classification, or other reasons.

CONTRACTOR REPORTS: Scientific and technical information generated under a NASA contract or grant and considered an important contribution to existing knowledge.

TECHNICAL TRANSLATIONS: Information published in a foreign language considered to merit NASA distribution in English.

SPECIAL PUBLICATIONS: Information derived from or of value to NASA activities. Publications include conference proceedings, monographs, data compilations, handbooks, sourcebooks, and special bibliographies.

TECHNOLOGY UTILIZATION PUBLICATIONS: Information on technology used by NASA that may be of particular interest in commercial and other non-aerospace applications. Publications include Tech Briefs, Technology Utilization Reports and Notes, and Technology Surveys.

Details on the availability of these publications may be obtained from:

SCIENTIFIC AND TECHNICAL INFORMATION DIVISION
NATIONAL AERONAUTICS AND SPACE ADMINISTRATION

Washington, D.C. 20546